NTNU
Norwegian University of
Science and Technology

Complete Simulation Models to Describe the Ductile-to-Brittle Transition of Steels for Arctic Applications

A Beremin-Gurson Approach

Henrik Andre Scheide

Master of Science in Mechanical Engineering
Submission date: May 2018
Supervisor: Odd Magne Akselsen, MTP
Co-supervisor: Antonio Alvaro, SINTEF
Bård Nyhus, SINTEF

Norwegian University of Science and Technology
Department of Mechanical and Industrial Engineering

Preface

The master's thesis is published at the Department of Mechanical and Industrial Engineering at the Norwegian University of Science and Technology (NTNU) in cooperation with SINTEF Industry (SINTEF Materials and Chemistry up until 01/2018), and the Arctic Materials Project. The master‘s thesis completes TMM4960 Engineering Design and Materials, Master's Thesis and equals 30 ECTS Credits.

The research and the work conducted have been under the supervision of Antonio Alvaro. Additional guidance and co-supervising have been provided by Odd Magne Akselsen, Vidar Osen and Bård Nyhus, all from SINTEF Industry. The thesis work was conducted between January and June 2018 and is an extension of a preliminary study from the course TMM4560 Engineering Design and Materials, Specialization Project. [126]

The specialisation project was conducted prior to the master's thesis and discloses two ductile-to-brittle transition models. Both models are based on the combination of The Complete Gurson Model and the RKR Criterion as a post-processing routine based on critical opening stresses over characteristic distances to visualise the ductile-to-brittle transition regions. The project thesis with its constitutive simulation scheme and model improvement discussions are the fundamental basis for the master's thesis. [126]

Most of the time was spent on doing extensive research on fracture mechanics, bimodal grain size distribution, and existing simulations models with their constitutive computational implementation methods. A lot of time and focus were also spent on computational simulations and modelling in ABAQUS to get accurate and representative results. The primary focus addresses the Weibull-based Beremin model and its adaptability to different steels, constraint levels, and laboratory testing requirements. Additional attention is set to the Weibull parameters which are shown to be the most complicated parts of the simulation scheme to adequately describe the abrupt fracture toughness transition. The fracture mechanical data collection was highly time-consuming due to the ambiguity of the SINTEF material database with its constitutive AM1-TP8 project and a more recent test series conducted to get characteristic resistance curves in the ductile region.

First of all, I would like to thank my supervisor Antonio Alvaro at SINTEF who has provided me with continuous feedback, fruitful discussions and support throughout the entire duration of the project and master's thesis endeavor. My outright gratitude to my co-supervisors Odd Magne Akselsen, Vidar Osen and Bård Nyhus who have contributed with valuable input and profound scientific discussions. It has been a privilege to write the master's thesis at SINTEF Industry which made room for personal development, freedom of research, and an utmost inspiring atmosphere.

11-06-2018, Trondheim

Henrik A. Scheide

Henrik A. Scheide

Abstract

The toughness of common structural steels is often affected by temperature changes where low service temperatures frequently promote brittle material characteristics. Low service temperatures often occur in the Arctic regions, and unexpected catastrophic failures may occur due to inadequate material characterisation. It is crucial to have a model with the highest level of accuracy to mitigate the risk of sudden brittle failure which in turn can precisely capture the material behaviour at shifting temperatures. The primary objective of the master‘s thesis is thus to develop a model which is able to describe the temperature dependence of fracture toughness in steels. The aim is to reduce the laboratory work needed to characterise the ductile-to-brittle transition regions. At lower temperatures, steels exhibit brittle behaviour and become susceptible to sudden brittle fracture without warning. Higher temperatures yield ductile behaviour with mechanisms such as void nucleation, void growth and void coalescence promoting ductile tearing and controlled ductile failure. The transition between the ductile and brittle regions exhibit both ductile and brittle behaviour and is crucial when steels are utilised in fluctuating and low service temperatures where sudden cleavage fracture may occur.

Two Gurson-RKR models are initially developed in a preliminary study to describe the complete ductile-to-brittle transition and to visualise the ductile, transition and brittle regions. [126] The RKR Criterion is a post-processing routine for the ductile Gurson model and is used to predict brittle failure by considering critical stresses along the crack ligament with the critical opening stress ahead of the crack tip as both temperature dependent and independent. The Combined Gurson-RKR Model with temperature independent opening stress can describe the ductile-to-brittle transition by demonstrating increasing fracture toughness with increasing temperature. However, the results are somewhat conservative as the combined model highly overestimates the steel's brittleness at higher temperatures. The Combined Gurson-RKR Model with temperature dependent critical opening stress can visualise the ductile-to-brittle regions where the upper and lower boundary limits capture all the experimental fracture toughness from -60 $^{\circ}C$ to 21 $^{\circ}C$. Nevertheless, the opening stress temperature approximation cannot be concluded without further testing, and several material fitting parameters remain uncertain and questionable. Hence, further improvements of the current model is necessary in order to develop a sufficient model to describe the ductile-to-brittle transition of steels with limited laboratory testing.

Thus, a more comprehensive model is developed to describe the ductile-to-brittle transition by introducing a statistical and mechanisms based model following the weakest-link principle; instability of one single microcrack in an arbitrary volume element may lead to complete specimen failure. A Weibull-based criterion substitutes the distance-based RKR Criterion which in turn provides a framework for the connection between the driving forces on a micro-scale level and macro-scale models for cleavage fracture. The Weibull-based Beremin model is used as a post-processing routine combined with The Complete Gurson Model and constitutes a complete generalisation of the probability of brittle fracture and ductile damage control while concurrently accounting for and supporting different crack configurations, geometry constraints, and loading modes. The two Beremin model parameters fitted in the brittle region are calibrated from experimental and theoretical results and respectively characterises the flaw distribution and the scaling factor of the Weibull

distribution utilised to calculate the probability of brittle fracture throughout the DBT.

The Weibull stress along with the calibrated Weibull parameters can be used to compute the probability of brittle failure by considering the aggregate sum of the maximum principal stresses in all the volume elements exceeding a particular critical stress. As the Beremin model largely underestimates the rupture energies in the transition region, The Complete Gurson Model is utilised to simulate ductile damage mechanisms to describe the shifting stress state in the transition region. The Weibull-based Beremin Model is then used as a post-processing routine to calculate the probability of brittle failure concurrently with the competing ductile mechanisms integrated by The Complete Gurson Model. Hence, the Gurson model is independently fitted to the experimental results at the highest temperature in the ductile region to accurately describe ductile mechanisms and crack extension throughout the ductile-to-brittle transition. The Gurson model can simulate accurate crack extension throughout the DBT for the high constraint geometry when utilising temperature independent Gurson parameters. However, the same Gurson parameters are only to some extent able to characterise the applicable resistance curves for the low constraint geometry.

The Weibull-based Beremin model can constraint-correct and characterise the fracture toughness to the specimens in the brittle region but is only to some extent able to describe the DBT as it overestimates the steel's brittleness in the transition region. A Gurson user-defined material (UMAT) with constitutive ductile mechanism equations is then used to characterise typical material behaviour in the transition region. The Beremin-Gurson model with temperature independent Weibull parameters fitted at the lowest temperature in the brittle region can constraint-correct the fracture geometries and describe the fracture toughness throughout the brittle region. However, the model is unable to capture the lower bound transition at higher temperatures but can capture the applicable upper bound transition in the ductile-to-brittle transition which evidently supports temperature dependent Weibull parameters. Thus, toughness scaling and constraint-correction of two fracture geometries with different constraint levels are conducted to find the appropriate temperature dependent Weibull parameters. The Beremin-Gurson model with temperature dependent Weibull parameters can accurately constraint-correct the fracture geometries and describe the relevant fracture toughness values throughout the ductile-to-brittle transition. The Weibull modulus defining the flaw distribution and the slope of the Weibull cumulative distribution function is constant in the brittle region and increases when entering the transition region where it remains relatively constant throughout the transition region. The scale parameter defining the resistance to brittle failure follows the opposite trend as large Weibull modulus promote small scale parameters and vice versa.

The current Beremin-Gurson model needs further improvements as several material parameters remain questionable and uncertain. The Weibull stress calculation program, LINKpfat must be further enhanced to represent the weakest-link principles in the constitutive Beremin model. Thus, a thorough evaluation of the Weibull stress calculation is necessary. Another weld simulated steel must be evaluated to conclude the Weibull parameter temperature trends, and a third constraint level must be integrated to infer the accuracy of the constraint-correction.

Sammendrag

Seigheten til vanlige strukturelle stål er ofte påvirket av temperaturendringer hvor lave operasjonstemperaturer ofte fremmer sprø materialegenskaper. Lave operasjonstemperaturer oppstår ofte i arktiske regioner, og uventede katastrofale brudd kan oppstå på grunn av utilstrekkelig materialkarakterisering. For å redusere risikoen for plutselige sprøbrudd er det viktig å ha en modell med høyest mulig nøyaktighet, og som er i stand til å nøyaktig beskrive materialets oppførsel ved skiftende temperaturer. Hovedmålet til masteroppgaven er dermed å utvikle en modell som er i stand til å beskrive temperaturavhengigheten til stålets bruddseighet. Målet er å redusere laboratoriearbeidet som trengs for å karakterisere regionene i overgangen fra duktil til sprø oppførsel. Ved lavere temperaturer har stålet sprø oppførsel og kan bli utsatt for plutselige sprøbrudd uten forvarsel. Høyere temperaturer gir duktil oppførsel med mekanismer som kjernedannelse av tomrom, vekst i tomrom og sammenvoksing av tomrom som fremmer duktil sprekkvekst og kontrollerte duktilitetsbrudd. Overgangsregionen mellom de duktile og sprø regionene har både duktil og sprø oppførsel, og er avgjørende når stål brukes i svingende- og lave operasjonstemperaturer der plutselige spaltningsbrudd kan forekomme.

To Gurson-RKR-modeller er i første omgang utviklet i en innledende studie for å beskrive overgangen fra duktil til sprø oppførsel, og for å visualisere de duktile og sprø regionene samt overgangsregionen. [126] RKR-kriteriet er en etterbehandlingsrutine for den duktile Gurson-modellen, og brukes til å forutsi sprøbrudd ved å vurdere kritiske spenninger langs midtsprekken hvor den kritiske åpningsspenningen foran sprekkspissen blir testet som både temperaturavhengig og -uavhengig. Den kombinerte Gurson-RKR modellen med temperaturuavhengig åpningsspenning er i stand til å beskrive den duktile til sprø overgangen som demonstrerer økende bruddseighet med stigende temperatur. Imidlertid er resultatene noe konservative da den kombinerte modellen overestimerer stålets sprøhet ved høye temperaturer. Den kombinerte Gurson-RKR modellen med temperaturavhengig kritisk åpningsspenning er i stand til å visualisere regionene i overgangen fra duktil til sprø oppførsel der de øvre og nedre grenseverdiene fanger alle de eksperimentell bruddseighetene fra -60$^\circ C$ til $21^\circ C$. Likevel kan temperaturapproksimasjonen av åpningspenningen ikke konkluderes uten videre testing, og flere materialparametere forblir usikre og tvilsomme. Videre forbedring av gjeldende modell er derfor nødvendig for å utvikle en tilstrekkelig modell til å beskrive den duktile til sprø overgangen av stål med begrenset laboratorietesting.

Dermed er en mer omfattende modell utviklet for å beskrive den duktile til sprø overgangen ved å innføre en statistisk og mekanismebasert modell som følger svakeste-ledd prinsippet; ustabilitet av en enkel mikrosprekk i et vilkårlig volumelement kan føre til fullstendig prøvestavbrudd. Det avstandsbaserte RKR-kriteriet er erstattet med et Weibull-basert kriterium som gir et rammeverk for sammenhengen mellom drivkraften på et mikroskala-nivå og makroskala-modeller for spaltningsbrudd. Den Weibull-baserte Beremin-modellen benyttes som en etterbehandlingsrutine kombinert med Den Komplette Gurson-modellen, og gir en fullstendig generalisering av sannsynligheten for sprøbrudd og duktil skadekontroll samtidig som den tar hensyn til og støtter ulike sprekk-konfigurasjoner, geometri constraint og laster. Beremin-modellen er innledningsvis tilpasset i den sprø regionen hvor to Weibull-parametere er kalibrert fra eksperimentelle og teoretiske resul-

tater. Weibull-parameterne kan henholdsvis karakterisere defektdistribusjonen og skaleringsfaktoren til Weibull-fordelingen brukt til å beregne sannsynligheten for sprøbrudd i hele overgangen fra duktil til sprø oppførsel.

Weibull-spenningene sammen med de kalibrerte Weibull-parameterne kan brukes til å beregne sannsynligheten for sprøbrudd ved å ta den samlede summen av de høyeste hovedspenningene i alle volumelementer som overstiger en viss kritisk spenning. Ettersom Beremin-modellen i stor grad overvurderer rupturkreftene i overgangsregionen er Den Komplette Gurson-modellen brukt til å simulere duktilskademekanismer for å beskrive den skiftende spenningstilstanden i overgangsregionen. Den Weibull-baserte Beremin-modellen brukes så som en etterbehandlingsrutine for å beregne sannsynligheten for sprøbrudd samtidig som de konkurrerende duktile mekanismene integreres med Den Komplette Gurson-modellen. Derfor er Gurson-modellen uavhengig tilpasset de eksperimentelle resultatene ved den høyeste temperaturen i den duktile regionen for å nøyaktig beskrive de duktile mekanismene og sprekkutvidelsen gjennom hele den duktile til sprø overgangen. Gurson-modellen er i stand til å simulere nøyaktig sprekkforlengelse gjennom hele den duktile til sprø overgangen for prøvestavene med høyt constraint-nivå ved bruk av temperaturuavhengige Gurson-parametere. Likevel er Gurson-parameterne kun til en viss grad i stand til å karakterisere de aktuelle motstandskurvene for prøvestavene med lavt constraint-nivå.

Den Weibull-baserte Beremin-modellen er i stand til å constraint-korrigere og karakterisere bruddseigheten til prøvestavene i den sprø regionen, men er bare til en viss grad i stand til å beskrive den duktile til sprø overgangen ettersom den overvurderer stålets sprøhet i overgangsregionen. Et Gurson-brukerdefinert materiale (UMAT) med grunnleggende ligninger for duktile mekanismer brukes så til å karakterisere den representative materialeadferden i overgangsregionen. Beremin-Gurson-modellen med temperaturuavhengige Weibull-parametere tilpasset ved den laveste temperaturen i det sprø området er i stand til å constraint-korrigere bruddgeometriene og beskrive bruddseigheten i hele den sprø regionen. Modellen er imidlertid ikke i stand til å fange den nedre grenseovergangen ved høyere temperaturer, men er i stand til å fange den aktuelle øvre grenseovergangen i den duktile til sprø overgangen, noe som tydelig støtter temperaturavhengige Weibull-parametere. Dermed er seighetsskalering og constraint-korreksjon av to bruddgeometrier med forskjellige constraint-nivåer utført for å finne de aktuelle temperaturavhengige Weibull-parameterne. Beremin-Gurson-modellen med temperaturavhengige Weibull-parametere klarer å nøyaktig constraint-korrigere bruddgeometriene, og beskrive de aktuelle bruddseighetsverdiene gjennom hele den duktile til sprø overgangen. Weibull-modulen som definerer defektfordelingen og helningen på den Weibull-kumulative distribusjonsfunksjonen forblir konstant i den sprø regionen, og øker når den går inn i overgangsregionen hvor den igjen forblir relativt konstant gjennom hele overgangsregionen. Skaleringsparameteren som definerer motstanden til sprøbrudd følger den motsatte trenden hvor stor Weibull-modul fremmer små skaleringsparametere, og omvendt.

Den nåværende Beremin-Gurson-modellen trenger ytterligere forbedringer ettersom flere materialparametere forblir tvilsomme og usikre. Programmet for Weibull-spenningsberegning, LINKpfat må forbedres ytterligere for å få en mer nøyaktig representasjon av svakeste-leddprinsippene til Beremin-modellen, og dermed må en grundig evaluering av beregningene av Weibull-spenningene bli gjennomført. Et annet sveisesimulert stål må vurderes for å konkludere temperaturtrendene til Weibull-parameterne, og et tredje constraint-nivå må integreres for å konkludere nøyaktigheten av constraint-korreksjonene.

Nomenclature

This list describes the constitutive symbols and acronyms used within the body of the paper.

A = Amplitude
A_{pl}^{CMOD} = Area under the Force-CMOD curve
B = Thickness of a SENB specimen
C_0 = Diameter of a second-phase particle
C = Material dependent Ramberg-Osgood constant
E = Young’s modulus
E’ = Elastic modulus under plain strain
J = Line J-integral
J_I = Line J-Integral of mode I crack
J_{IC} = Critical J_I
K = Stress intensity factor
K_I = Stress intensity factor of mode I crack
K_{IC} = Critical K_I for cleavage fracture initiation
P_F = Cumulative probability of failure
P_S = Survival probability (reliability)
Q_{max} = Maximum stress intensification factor
T_p = Peak temperature
V_0 = Elementary volume of V_p (reference volume)
V_p = Volume of the fraction process zone (FPZ)
W = Width of a SENB specimen
α = Numerical constant function of the crack shape
Δa = Crack growth
$\Delta t_{8/5}$ = Weld cooling time between 800-500$^\circ C$
Γ_0 = Minimum work of separation for cleavage
γ_p = Effective surface energy
γ_s = Specific surface energy
δ = Crack tip opening displacement (CTOD)
δ_c = Critical CTOD
δ_0 = Initial crack opening
ϵ_p = Plastic strain tensor
ϵ_{eq} = Equivalent von Mises plastic strain tensor
ϵ_v = Equivalent von Mises plastic strain
$\epsilon_1, \epsilon_2, \epsilon_3$ = Principal strains
λ = Weibull scale parameter (CTOD)
σ_0 = Initial tensile yield strength
σ_{22} = Opening stress
σ_{UTS} = Ultimate tensile strength
σ_c = Critical stress
$\sigma_{c_{TD}}$ = Temperature dependent critical opening stress
$\sigma_{c_{TID}}$ = Temperature independent critical opening stress
Φ = Gurson yield function

σ_d = Decohesion stress
σ_e = Effective stress
σ_{eq} = Equivalent von Mises stress
σ_f = Fracture stress
σ_m = Mean stress
σ_u = Weibull scale parameter
σ_w = Weibull stress
σ_y = Uniaxial yield strength
σ_{ys} = Yield strength
σ_{yy} = Opening stress
σ_{yymax} = Maximum opening stress
σ_1, σ_2, σ_3 = Principal stresses
σ_{ij} = Stress tensor
θ = Angle from crack tip to stress field
a = Half the length of an internal crack
a_c = Critical crack depth
a_0 = Initial crack depth
d = Average grain diameter
f = Void volume fraction
f_{area} = Grain size area fraction
f^* = Artificially accelerated void growth
f_c = Critical void volume fraction
f_F = Void volume fraction at the end of coalescence
f_0 = Initial void volume fraction
f_{ij} and g_{ij} = Dimensionless functions of θ
i = Rank number
k = Weibull shape parameter (CTOD)
l_c = Mesh element length
m = Weibull modulus
n = Strain hardening exponent
q = Heat input (during welding)
q_{vm} = Von Mises stress
q_1 = Constant Gurson factor ($= 1.5$)
q_2 = Constant Gurson factor ($= 1.0$)
r = Distance from crack tip to stress field
$\bar{r}$ = Current void radius
r_0 = Initial void radius
r_p = Rotational factor (equal to 0.44)
t = Surface traction
v = Poisson's ratio
x_c = Characteristic distance

.cmd = Commando script
.dat = Output file
.inp = Input file
.odb = ABAQUS database file
.pfp = LINKpfat simulation file

CDF = Cumulative Distribution Function
CE = Carbon Equivalent
CMOD = Crack Mouth Opening Displacement
CGHAZ = Course-Grained Heat Affected Zone
CTOD = Crack Tip Opening Displacement
CVN = Charpy V-Notch
DBT = Ductile-to-Brittle Transition
DBTT = Ductile-to-Brittle Transition Temperature
EDM = Electrical Discharge Machining
FE = Finite Element
FEA = Finite Element Analysis
FEM = Finite Element Method
FGHAZ = Fine-Grained Heat Affected Zone
FPZ = Fracture Process Zone
GTN = Gurson, Tvergaard and Needleman
HAZ = Heat Affected Zone
LSQ = Least Square
ML = Maximum Likelihood
MLE = Maximum Likelihood Estimation
MOTE = Minimum Of Three Equivalent
M-A = Martensite-Austenite
RKR = Ritchie-Knott-Rice
SDV = State-Dependent Variable
SENB = Single Edge Notched Bend
SENB02 = SENB specimen with $\frac{a}{W} = 0.2$
SENB05 = SENB specimen with $\frac{a}{W} = 0.5$
SENT = Single Edge Notched Tension
SP = Specimen
SSY = Small-Scale Yielding
TD = Temperature Dependent
TID = Temperature Independent
UFG = Ultrafine-Grained
UMAT = User-Defined Material

Table of Contents

Chapter 1

Introduction

With increasing activity from the oil and gas industry in Arctic regions, harsher ambient conditions must be taken into account when designing structural steels. Higher material property requirements and the urgency for a better understanding of the weather impact in the Arctic region is inevitable. Thus, a thorough examination of the temperature dependent material properties is crucial and needs to be further investigated in order to operate safely and efficiently in the Arctic regions.

One of the most vital material parameters is the fracture toughness of steels and its temperature dependence. At low temperatures, steels tend to exhibit brittle characteristics and low fracture toughness which in turn might lead to sudden fracture without warning yielding catastrophic consequences. Common structural steels become more ductile with increasing temperature, and the fracture toughness increases gradually with a steep transition at a constraint-specific transition temperature. This transition region is of crucial importance as it defines when the steel becomes brittle at lower temperatures and needs to be further investigated to understand the material behaviour changes. Thus, a comprehensive examination of the complete ductile-to-brittle transition of steels is of utmost importance.

Several models are described and suggested to predict brittle failure, and other models for ductile behaviour characterisation. A computational simulation scheme must be developed to lower the need of laboratory testing of steels to describe the ductile-to-brittle transition. In the end, this will lead to less laboratory work which saves time and costs when characterising structural steels. The simulation scheme is required to describe the ductile region with material softening mechanisms, the brittle region constituting cleavage initiation, and the transition region exhibiting both brittle and ductile characteristics. The ultimate goal of the ductile-to-brittle transition study is to develop a model which can predict the DBT of structural steels by only requiring one fracture mechanics test series in the brittle region and another one in the ductile region. However, in the transition region, only simple uniaxial tensile tests should be required to characterise the essential stress-strain curves needed to simulate the shifting stress field.

Due to the dissimilar fracture toughness scatter bands primarily in the brittle and transition region, several approaches have been considered to describe the material characteristics. The preliminary Gurson-RKR model utilises the RKR Criterion as a post-processing routine based on critical opening stresses along the crack ligament to identify cleavage fracture initiation. The model can visualise the ductile-to-brittle transition regions, but the

100% probability based model is quite conservative and consists of several questionable material parameters and limitations. There is a range of different approaches to improve the preliminary Gurson-RKR model, and two of the most prominent methods are a statistical distribution model and a traction-separation cohesive zone model. The distance-based RKR Criterion can be improved by considering several critical material parameters such as plastic strain, stress triaxiality and tensile stress in volume elements instead of characteristic distances. It can also be established as a probability distribution model which characterises the applicable volume in the active zone ahead of the crack tip. The volume-based approach can be used to create statistical distributed ductile-to-brittle transition curves, and concurrently support and relate to different crack configurations and constraint effects to connect test data to large-scale structures.

Another method to describe the brittle behaviour of the material is the cohesive zone approach where a traction-separation curve is used to model the fracture process zone. By utilising FE-analysis, the model can solve boundary value problems at the crack tip by considering the cohesive strength of the material and the work of separation needed to get a complete brittle fracture. However, in several types of steels, especially when welded, the microstructure constitute a bi-modal grain size distribution consisting of both coarse and fine grain bands. The bi-modal grain size distribution leads to more significant scatter bands in the transition region as the distance from the coarse grain band to the notch root varies from specimen to specimen where a mixed microstructure might yield biased results when utilising uni-modal simulation models. Thus, the bi-modal grain size distribution must be considered when designing the computational simulation scheme to describe the material behaviour and the complete ductile-to-brittle transition in steels. The ultimate objective is to be able to predict and describe the ductile-to-brittle transition of both bi-modal and uni-modal grain size distributed steels by utilising a complete simulation model which are statistical and mechanism-based at a low-cost level and with limited laboratory testing requirements. The Complete Gurson Model and the Weibull-based Beremin model as a post-processing routine are utilised to characterise ductile damage mechanisms and to calculate the probability of brittle failure throughout the whole DBT in structural steels.

The first part of the thesis introduces the fundamental fracture mechanics theory required to understand the subsequent chapters along with a more comprehensive description of all the constitutive ductile-to-brittle transition models. Some of the background theory is converted from the preliminary project thesis [126], and a detailed presentation of The Combined Gurson-RKR Model is described in order to justify the chosen simulation models. Furthermore, the computational implementation methods of the Weibull-based Beremin model and The Complete Gurson Model are along with finite element models and a comprehensive material characterisation described in the subsequent chapter. The last chapters constitute all the results and discussions with the Beremin model and The Complete Gurson Model implemented and fitted individually. The Gurson parameters are estimated at the highest available temperature in the ductile region, and the Weibull parameters used in the Beremin model are initially calibrated at the lowest temperature in the brittle region. The Weibull-based Beremin model is as a post-processing routine combined with The Complete Gurson Model to compute the probability of brittle failure throughout the ductile-to-brittle transition. The final part consists of Weibull parameter temperature dependency studies, a thorough discussion of the final Beremin-Gurson model, concluding arguments, and a brief future work description.

1.1 Arctic Materials Project

Between 22-25% of the undiscovered and technically recoverable oil and gas reserves in the world are located in the Arctic region. The expected undiscovered reserves in the Arctic region comprise 20% of the world's liquefied natural gas, 30% of the natural gas, and 13% of the oil reserves. [129][49][127] The extremely harsh weather conditions in the Arctic region along with vast distances cause challenging oil and gas operations. To establish safe and cost-effective applications of materials for hydrocarbon exploration and production in the Arctic region, SINTEF is carrying out an extensive research project called the Arctic Materials Project. [129] The objective is to establish material solutions and criteria which can handle the material application challenges at low temperatures down to -60$^\circ C$, light-weight solutions, and significant temperature variations and deformation. SINTEF has the project leadership and is cooperating with major industrial companies such as Equinor, DNV GL and Aker Solutions focusing the research and development of steels, polymer materials, and composite materials. [129]

As today's industry lack standards to qualify structural steels in the Arctic region, material selection and material characterisation are quite challenging and expensive. Due to the challenging but essential material selection process, the master's thesis directs the constitutive discussion to the following Arctic Materials Project sub goals: [129]

- ☐ Extend the application range of structural steels by characterising the brittle fracture resistance in welded steels including local material property variations and geometry constraint effects
- ☐ For design temperatures down to -60$^\circ C$; define criteria for application of steels and weldments including safety factors, and develop specifications for qualification testing
- ☐ For light-weight high strength steels; develop the basis for application, and define material criteria for safe application under large deformations

The fundamental objective of the thesis is to develop understanding and a model to describe the material performance under Arctic conditions such as large temperature variation, low temperatures, and large deformations. Hence, the thesis will also address the following work packages (WP) to review the development of guidelines for qualification of weldments and steels: [129]

- ■ Mechanical characterisation and steel fabrication
- ■ Toughness and strength criteria for safe material utilisation
- ■ Material solutions and new concepts

One of the most immediate concerns is the fracture toughness of weldments which can yield low fracture toughness with brittle characteristics at low temperatures. As steels become brittle at low temperatures, it is crucial to qualify and develop ductile steels for low-temperature applications. Hence, the thesis focuses on the characterisation of brittle fracture resistance in steel structures with varying temperature and material properties. Thus, the main objective is to develop criteria and guidelines for qualifying steels for Arctic conditions in a safe and cost-efficient way.

Chapter 2

Theoretical Background

This chapter covers the fundamental theory required to understand the results and discussions in the subsequent chapters. The theoretical background chapter will enable the reader to get a comprehensive insight into the most important elements to understand the complexity of both fracture mechanics and the ductile-to-brittle transition of steels. Sections of the theoretic background is converted from the author's preliminary project thesis. [126]

2.1 Stress Triaxiality

Stress triaxiality is the triaxiality of the stress state and the ratio of the hydrostatic stress and the effective von Mises stress as described in Equation 2.1. The stress triaxiality factor, TF is only dependent on the principal stresses σ_1, σ_2 and σ_3 and affects both void growth and void coalescence under plastic deformation in ductile materials. Even under uniaxial loading conditions, the material will be exposed to a triaxial stress state with concurrent stresses in three directions.

$$TF = \frac{\sigma_h}{\sigma_e} = \frac{\frac{1}{3}(\sigma_1 + \sigma_2 + \sigma_3)}{\frac{1}{\sqrt{2}}\sqrt{(\sigma_1 - \sigma_2)^2 + (\sigma_2 - \sigma_3)^2 + (\sigma_3 - \sigma_1)^2}} \tag{2.1}$$

On a micromechanical level, the stress triaxiality promotes void growth and causes damage in the affected process zone ahead of the crack tip. [27] Models such as the Gurson model can describe the physical effects of the crack tip constraint and the tearing resistance as explained in Section 3.2.1. As the triaxiality factor increases, a progressive reduction of the material elasticity occurs at necking initiation. [24][107]

The stress triaxiality factor (TF) applies as a constraint parameter, and with plastic strain, the two parameters can control ductile rupture by cavity nucleation and growth. [114][56][57] The equivalent von Mises plastic strain, ϵ_v is usually defined as

$$\epsilon_v = \frac{1}{\sqrt{2}}\sqrt{(\epsilon_1 - \epsilon_2)^2 + (\epsilon_2 - \epsilon_3)^2 + (\epsilon_3 - \epsilon_1)^2} \tag{2.2}$$

where ϵ_1, ϵ_2, and ϵ_3 are the principle strains, $\epsilon_1 > \epsilon_2 > \epsilon_3$.

2.2 Microstructures and Welding in Steel

A variety of different microstructures in structural steels depend on the alloy content and the processing of the steel. Different phases form through phase transformation during processing which in turn changes the entire crystal structure. One of the two main phase transformations is the reconstructive phase transformation where the atoms rearrange into alternative and random patterns after the bonds break. There is no shape deformation, the volume change due to atom diffusion, and usually occurs at high temperatures. The second one is shear transformation where homogeneous deformation creates a new crystal structure from shape deformation in a specific manner and order. [22] The reader is expected to know the basic characteristics of austenite, ferrite, martensite, and bainite along with acicular ferrite, and Widmanstätten ferrite. More information about the material phases in [22], [89], and [135].

2.2.1 Welding and Heat Affected Zones

Weldments are often considered as the most crucial part of the construction as it often exhibits brittle characteristics compared to the parent material, and comprise a large density of impurities which actively reduces the toughness. The microstructure in steels often change during welding, and many different microstructures form in the heat affected zone depending on the chemical composition and the thermal cycles during welding. [83] The welding process might yield heterogeneous microstructure with varying toughness. [2] [1] The weld zone can be divided into two main regions; the HAZ and the fusion zone as shown in **Figure 2.1**. During welding, the fusion zone is heated up to the melting point, and the HAZ is the area around the fusion zone where the steel's microstructure changes without melting. [22]

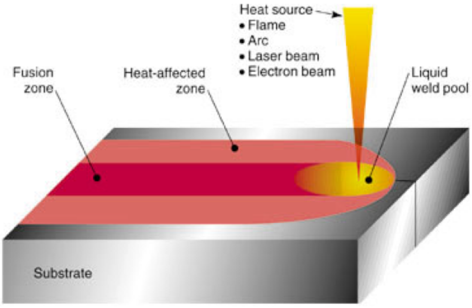

Figure 2.1: Heat source and the two main regions; fusion zone and HAZ [42]

The HAZ comprises several different regions and microstructures with different mechanical features. The main parameters which determine the final microstructure in the HAZ are the cooling rate, $\Delta t_{8/5}$, the heat input, q, and the peak temperature, T_p. $\Delta t_{8/5}$ is the time for cooling the material from $800°C$ to $500°C$ and is crucial for the phase transformation from austenite to ferrite. [22] The peak temperature and the heating rate decreases with distance from the fusion zone, while the cooling rate is independent of distance as respectively shown in Equation 2.3 and 2.4.

$$T_p \propto \frac{q}{r} \tag{2.3}$$

$$\Delta t_{8/5} \propto q^n \tag{2.4}$$

r characterises the distance from the fusion zone, and n is equal to 1 or 2 depending on the heat input, q, being two or three dimensional, respectively. [22] As shown in Equation 2.3 and 2.4, both parameters are increasing with heat input and can both be utilised to determine the nature of the thermal cycle at any given point in the HAZ.

The HAZ in single-pass welds separates into four central regions with depreciating toughness with increasing distance from the fusion zone; Course-Grained HAZ (CGHAZ), Fine-Grained HAZ (FGHAZ), Intercritical HAZ (ICHAZ), and Subcritical HAZ (SCHAZ) as shown in **Figure 2.2**. [39]

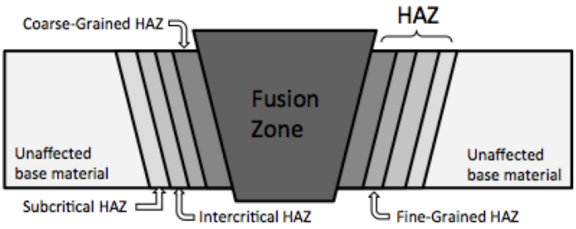

Figure 2.2: Illustration of the HAZ regions in single-pass welds [120]

Figure 2.3 illustrates the varying T_p with distance from the fusion zone and how it relates to the microstructure obtained in the HAZ after cooling. The heat diffusion changes the microstructure and the mechanical properties of the HAZ regions. Regions close to the fusion boundary have very high temperatures, and during continuous heating over the ferrite to austenite transformation temperature, $950°C$ [22], a fully austenitic microstructure forms. The CGHAZ primarily comprises large austenite grains due to annealing over $950°C$, and the final CGHAZ microstructure depends on the density of impurities in the parent material, the cooling time $\Delta t_{8/5}$, and the chemical alloy composition. The coarse-grained HAZ is coarse with brittle characteristics and often comprises a variety of M-A Constituents (see Section 2.2.2), carbides and martensite. Also, the fracture toughness in the CGHAZ has often been observed to decrease with increasing T_p. [1]

The CGHAZ is commonly characterised as the most brittle region with the lowest toughness in the HAZ, but in later studies, the Intercritically Reheated CGHAZ (ICCGHAZ) has exhibited even greater toughness degradation due to its large austenite grain size, M-A Constituents, and micro-alloy precipitates. [75] Rapid cooling (low $\Delta t_{8/5}$) will yield incomplete austenite to ferrite-bainite transformation resulting in M-A Constituents which in turn degrade the material. [74] [34] The M-A Constituents are brittle and hard islands of austenite in bainitic ferrite matrix and carbon-rich martensite. At high cooling rates, the CGHAZ is primarily bainite and martensite, and at lower cooling rates, the CGHAZ commonly comprises lower and upper bainite, bainitic ferrite, and M-A Constituents. The diffusion increases with decreasing cooling rate which in turn leads to even more bainitic ferrite, M-A Constituents, and upper bainite. [79] The M-A Constituents are further described in Section 2.2.2.

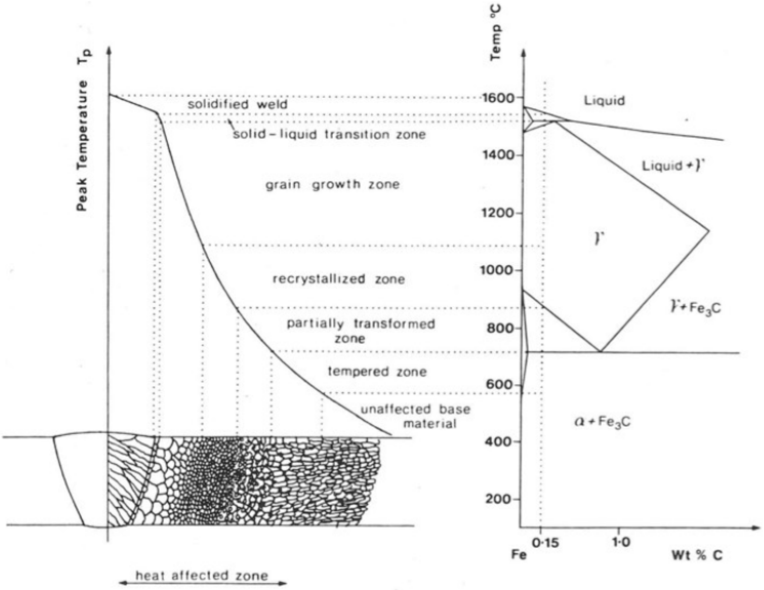

Figure 2.3: HAZ microstructures in single-pass welds with a corresponding phase diagram. [22]

Further away from the fusion boundary, the temperature will not be sufficient to yield full annealing which in turn leads to decreasing austenite grain size. This zone is commonly referred to as the fine-grained zone and tends to be superior to the CGHAZ regarding strength and toughness. Beyond the fine-grained zone, the microstructure partially transforms to austenite. This austenite comprises a high concentration of carbon due to the increasing carbon solubility in austenite with decreasing temperature. And even further away from the fusion boundary, regions of the HAZ do not transform to austenite and are thus characterised as tempered. [22] [43]

2.2.2 M-A Constituent Regions

Local brittle zones such as M-A Constituents in the HAZ is often associated with degradation of the fracture toughness in steels after welding. [43] [79] Upper bainite, microalloy precipitates, and M-A islands are some of the leading metallurgical factors which tend to lower the fracture toughness in the CGHAZ. [43] The M-A Constituents or M-A Islands have retained austenite enclosed by bainitic ferrite matrix and carbon-rich martensite. They commonly form at high temperatures with average cooling rates, and the morphology depends on the cooling time during welding. [34] [3] [65] The M-A constituents usually have either a morphology with blocky particles (M-A Islands) formed at austenite grain boundaries at longer cooling times, [78] or elongated lath particles developed between martensite laths at short cooling times. [34]

Up to a particular maximum cooling time, increasing cooling times lead to a higher amount of M-A Constituents. At higher cooling times, austenite, carbide, and ferrite formation are possible which in turn will decrease the amount of M-A Constituents. [65] The M-A regions affect the fracture toughness and the transition temperature due to its brittle characteristics from the high carbon content. [32] Increasing amounts of M-A Constituents increases the ductile-to-brittle transition temperature which means the steel will exhibit brittle fracture mechanisms at even higher temperatures. [65] Besides, the increasing amount of M-A Constituents will yield even lower fracture toughness making the material even more brittle. [3] The brittleness of the M-A Constituents promote cleavage initiation as described in Section 2.3.1, and the increased local stress concentration around the M-A Constituents will eventually yield broken bonds between the matrix and the M-A Constituents initiating a microcrack which ultimately leads to fracture.

2.2.3 Bi-Modal Grain Size Distribution

Materials are often considered as uni-modal with one dominant grain size which determines the appropriate critical distance and critical stress for failure as assumed in material models such as the RKR Criterion [115] described in Section 3.1.1. However, steels utilised in engineering applications can exhibit a mixed microstructure with inhomogeneities in the form of one soft and one hard phase. [159] This type of bi-modal microstructure leads to a more complex material characterisation process, and several researchers [7] [62] have tried to describe and explain the effect of grain size bimodality on fracture toughness. Neville and Knott [97] produced dual-phase steel with a mixture of ferrite and martensite phases and concluded that inhomogeneity rather than experimental errors primarily caused the variation in fracture toughness.

A bi-modal grain size distributed steel is not necessarily a disadvantage, and both second-phase particles and bi-modal grain distributions must be considered when improving the strength-ductility ratio. [131][145][100] Hanamura et al. [55] showed that steel with a bi-modal distribution of ferrite grains comprising UFG ferrite/cementite microstructure has even better impact toughness than conventional microstructures in low carbon steels. One method to generate a bi-modal microstructure in low carbon steel is by cold rolling and annealing of ferrite-martensite dual-phase steel. The heterogeneous microstructure is created by the concurrent recrystallization of ferrite and martensite with carbide initiation in the martensitic regions. [13]

However, as the effective grain size is one of the most important factors to determine the DBTT, the bimodality turns into a difficult challenge during material characterisation. [164] High-angle grain boundaries exceeding 15° are more effective in impeding cleavage fracture, [69] and are usually prevailing in the coarse-grained regions. [162] [163] As shown in Equation 2.5, the DBTT for low carbon steels is highly dependent on the effective grain size, d_{eff}. The material constant A contains several metallurgical factors apart from the grain size, and B is a coefficient independent of the grain size. [55]

$$DBTT = A - B \cdot ln(d_{eff}^{-1/2}) \tag{2.5}$$

$$d_{eff}^{-1/2} = \sum_{i=1}^{n} d_i^{-1/2} f_{area-i} \tag{2.6}$$

Zhao et al. [161] showed that for heterogeneous materials, the effective grain size is the sum of each grain size, d_i for n grains multiplied by the grain size area fraction, f_{area-i}

as shown in Equation 2.6. The effective grain size follows a normal Hall-Petch relation (strength $\propto d^{-1/2}$) for homogeneous grains based on the fraction area of each grain. In recent studies of bi-modal grain size distributed steels [31], it is shown that a large grain size with an area percent higher than four percent can yield cleavage initiation independent of the more dominant fine grain size distribution. Hence, Equation 2.6 may not be valid for bi-modal materials with two dominant grain size distribution peaks exceeding four percent fraction area as shown in **Figure 2.4 (d)**.

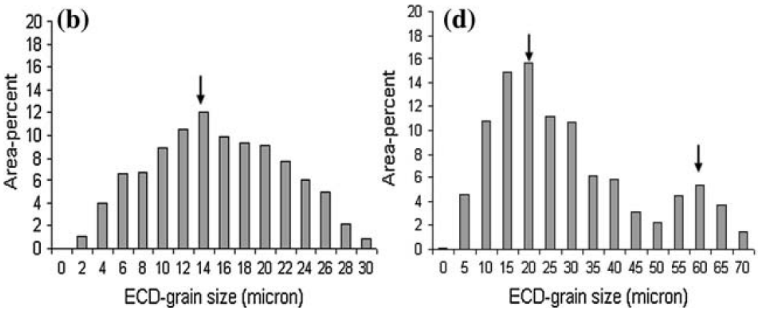

Figure 2.4: (b) Uni-modal grain size distribution, (d) Bi-modal grain size distribution [31]

By conducting a range of CVN tests of both uni-modal and bi-modal materials can characterise the effect of grain size bimodality on fracture toughness in the transition region. The overall fracture toughness scatters for bi-modal materials are usually larger than uni-modal materials due to the presence of coarse grain populations with larger grains which ultimately leads to low fracture toughness. Thus, the mixed microstructure will comprise randomly distributed bands of fine and coarse grains where the coarser grain bands act as the weakest-link for cleavage initiation. [31] The difference in size and distance between the fine and coarse grain bands results in a wide scatter of fracture toughness in the transition region. As the bi-modal grain size distribution is heterogeneous and follows weakest-link principles, scientists commonly use a Weibull-based Beremin model (see Section 3.1.3) with two independent Weibull distributions to account for the complex scatter variation. [110] [6] In addition to the bimodality challenges of single-pass weld as illustrated in **Figure 2.2**, multi-pass welds with multiple thermal cycles often comprise several reheated microstructures such as Intercritically Reheated CGHAZ (ICCGHAZ) and Subcritically Reheated CGHAZ (SCCGHAZ) which can lead to weld sections with varying mechanical properties and even more local brittle zones like M-A Constituents. [83] [38] [120]

2.3 Brittle Fracture

A fracture is when a solid is separated permanently into two or more pieces. Brittle fractures are often related to a critical crack initiation stage without any significant crack propagation or crack growth prior to fracture, and are characterised by sudden fractures without any visual warning due to its rapid and unstable crack growth.

Brittle fracture only happens when the stresses at the crack tip exceed the cohesive strength of the material. It is the most dangerous form of fracture characterised by the separation across well-defined crystallographic planes, and often exhibit a river pattern on the fracture surface originating from the crack initiation point. The fracture toughness can also readily be determined in the lower transition region in steels by conducting fracture mechanics tests. [33]

Brittle fracture occurs suddenly without warning and can be characterised by a specific stress limit which must be avoided to ensure safe service conditions. The tendency of brittle fracture in structural steels is highly temperature dependent and can be illustrated by a ductile-to-brittle transition curve. More about this transition curve in Section 2.7.

2.3.1 Cleavage Fracture Initiation

Three stages can characterise the complete brittle fracture process; the initiation of a crack nucleus, crack propagation across the boundary between the particle and the first grain, and crack propagation across the entire grain into another adjacent grain. The initiation of the crack nucleus depends on the microcrack extension in a second-phase particle and the nucleation of the crack.

By utilising the fracture mechanics parameters K, J and δ (CTOD) calculated by FEA, and building the stress and strain field ahead of a pre-cracked tip, the driving forces for triggering the brittle fracture can be determined. The normal stress, σ_{22} and the local plastic strain, ϵ_p are the most important driving forces to trigger the microcracking and must be balanced with the critical resistance of the material. [86]

The driving forces of the material are presented by the fracture mechanics parameters K_I, J_I and δ which in turn controls the corresponding crack-tip field and must exceed the resistance parameters of the material, K_{IC}, J_{IC} and δ_C in order to trigger a brittle fracture as described in Equation 2.7. [33]

$$K_I \geq K_{IC}, \quad J_I \geq J_{IC}, \quad \delta \geq \delta_C \tag{2.7}$$

The crack initiation is primarily influenced by the extent of second-phase particles, grain size, and the service temperature. Under high stresses or strains, the second-phase particles might exhibit microcracks ahead of the crack front primarily due to the high concentration of M-A Constituents. The particle fracture stress, σ_f is presented in Equation 2.8 where γ_p is the effective surface energy, E is the Young's modulus, v is Poisson's ratio, and C_0 is the diameter of the second-phase particle. [33]

$$\sigma_f = \sqrt{\frac{\pi E \gamma_p}{(1-v^2)C_0}} \tag{2.8}$$

The grain size effect is one of the most important factors regarding brittle fracture due to its impact on the ductile-to-brittle transition temperature (see Section 2.7) as well as the yield strength and ductility. Coarser grains yield higher DBTT, lower ductility and lower yield strength which is related to the dislocation pile-ups at the grain boundaries. Larger grains leads to more severe dislocation pile-ups and higher stress concentrations which in turn lead to higher probability of brittle fracture. Hahn proposed a crack propagation criteria below the transition temperature as when the maximum normal stress exceeds σ_f the material will fail by brittle fracture as described in Equation 2.9 and 2.10. [54]

$$\sigma_{yymax} = Q_{max}\sigma_y = \sigma_f \tag{2.9}$$

$$\sigma_f = \sqrt{\frac{\pi E \gamma_p}{(1-v^2)d}}\ (for\ a\ grain\ size\ crack) \tag{2.10}$$

σ_{yymax} is the maximum normal stress, Q_{max} is the maximum stress intensification factor, σ_y is the uniaxial yield strength, and d is the average grain diameter. [37]

Ritchie et al. [115] established a critical distance criterion where they showed that before brittle fracture could occur, the critical opening stress must be exceeded over a characteristic distance ahead of the crack tip. The RKR Criterion is further discussed in Section 3.1.1 where the characteristic distance is in fact found to be dependent on the grain diameter.

2.4 Ductile Fracture

Ductile fracture is when a material fails after a certain degree of plastic deformation and is used to indicate failure when the plastic deformation yields unstable crack propagation. This type of failure is often related to a process of void nucleation followed by void growth and void coalescence which ultimately leads to a macroscopic fracture. The fracture surface often appear as dimpled, and the material will fail when it reaches a plastic instability point where the strain hardening cannot keep up with the loss of cross-sectional area. [4] [158] Thus, the material will fail by the tearing instability when voids coalesce yielding rapid ductile crack growth followed by complete failure.

The consecutive stages prior to ductile failure are:

1. An inclusion or second-phase particle form a free surface either by particle cracking or interface decohesion yielding void nucleation.

2. Void growth around the particle by hydrostatic and plastic strain.

3. Coalescence of adjacent voids leading to rapid crack growth and failure.

The constitutive stages are exhibited in **Figure 2.5** and show the process of void nucleation, void growth, and void coalescence. The respective stages are further described in Section 2.4.1, 2.4.2 and 2.4.3.

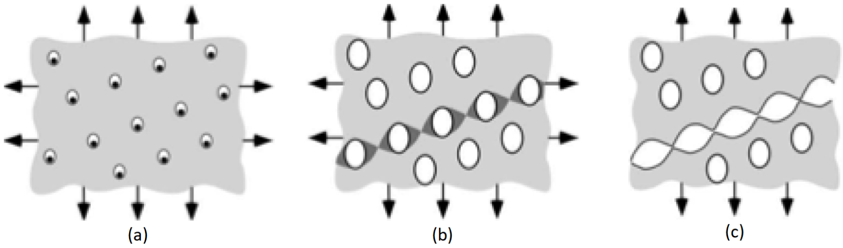

Figure 2.5: (a) Void Nucleation, (b) Void Growth, (c) Void Coalescence. [4]

2.4.1 Void Nucleation

Void nucleation happens in the early stages of deformation where the voids form mainly from inclusions or second-phase particles after the stress breaks the bonds between the matrix and the particles. The two most essential models for estimating the void nucleation stress are the continuum theory discussed by Argon et al. [10] and Beremin et al. [17], and the dislocation-particle interactions addressed by Goods and Brown. [51]

The continuum theory argues that the decohesion stress is equal to the sum of the mean hydrostatic stress and the effective von Mises stress as described in Equation 2.11

$$\sigma_d = \sigma_e + \sigma_m \tag{2.11}$$

which Beremin later optimised by utilising a semi-empirical relationship to predict a better void nucleation stress in special rolling conditions. [17] [10]

Goods and Brown made a dislocation model for void nucleation which consisted of both heterogeneous and homogeneous void nucleation. Cavities might form from vacancy condensation with high strain and high dislocation density which promotes homogeneous void nucleation. The dislocation model indicates increasing local stress concentration with decreasing particle size which concludes that larger particles make void nucleation more difficult. [51] However, larger particles are more likely to crack when exposed to plastic strain due to the increased probability of inclusions and second-phase particles.

Grain boundaries and second-phase particles are essential factors in heterogeneous void nucleation. It is shown that grain boundary sliding is the primary mode of deformation at low strain rates and intermediate temperatures, and is modelled as dislocation pile-ups when they meet obstacles. However, during sliding, the nucleation of cavities is independent of temperature which indicates that matrix displacement is determining the void nucleation. [51]

Second-phase particles and large non-metallic inclusions such as sulphides and oxides can be induced and created during material production which in turn promote void nucleation and ductile rupture. The local deformation state between the particle and the matrix might determine the cavity initiation and not the applied stress. Thus, the two mechanisms for void nucleation are cracking of the particle and decohesion between matrix and particle. [82]

2.4.2 Void Growth

Void growth is the second stage in the process of ductile fracture where voids start to grow immediately after void nucleation. The localised strain is then propagating between the voids until necking initiation and void coalescence. As abundant materials contain bimodal or tri-modal distribution of particles, intermetallic particles can exhibit submicron second-phase precipitates or inclusions dependent on the size and type of particle.

The two most widely used void growth models are from Rice and Tracey [112] and Gurson [53]. Rice and Tracey's model is based on a single isolated void which approximates the void growth with the semi-empirical relationship described in Equation 2.12

$$\ln\Big(\frac{\bar{r}}{r_0}\Big) = \alpha \int_0^{\epsilon_{eq}} exp\Big(\frac{1.5\sigma_m}{\sigma_e}\Big) d\epsilon_{eq} \tag{2.12}$$

where $\bar{r}$ is the void radius, r_0 is the initial void radius, ϵ_{eq} is the equivalent von Mises plastic strain tensor, σ_m is the hydrostatic mean stress, and σ_e is the effective stress which substitutes the yield strength, σ_{ys} in the original Rice and Tracey model. [112]

The growth of artificially inserted voids has recently been studied with tomography by Weck et al. [146]. The voids initially elongate first at a rate twice as fast as the specimen due to the high stress concentration. With a necking-induced increase in triaxiality, the voids start to grow laterally, and when the lateral void diameter to void spacing ratio reaches $1/3$, the plastic flow localisation in the ligaments changes the void growth kinetics. In engineering alloys, it is essential to consider the coexistence of continuous void nucleation and void growth which can lead to challenges when modelling ductile material behaviour. There is also a modelling challenge when multiple concurrent nucleations happen which in turn promote challenges to the conventional continuum frameworks. [106]

2.4.3 Void Coalescence

Void coalescence occurs in a lot of different modes and variants solely dependent on the microstructure, plastic flow and stress state. The void coalescence phenomenon can categorise into three modes; internal shearing of the intervoid ligament, internal necking of the intervoid ligament, and necklace coalescence as shown in **Figure 2.6**. [106]

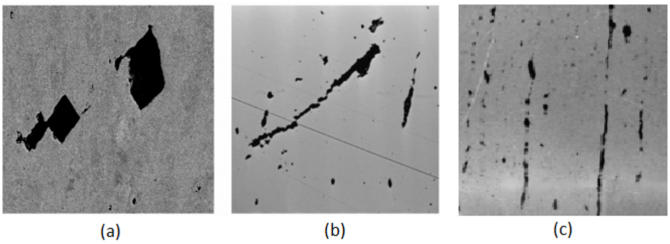

Figure 2.6: (a) Internal necking, (b) Internal shearing, (c) Necklace coalescence. [106]

Internal necking of the intervoid ligament describes the void impingement which was hypothesised by Cottrell [35] and later rationalised by Thomason [133] in plane strain. Deformation will localise in areas where the intervoid matrix loses bearing capacity due to increasing void growth which in turn yields necking in the matrix between the bonds. As a result of the necking, the voids will coalesce and form a large crack. Internal shearing of the intervoid ligament may yield localised cavities to coalesce due to the localised shearing. The cavities will form narrow bands of secondary voids (see **Figure 2.6 (b)**) as a result of local failure by void sheeting and secondary void nucleation. [36] Necklace coalescence is when voids link up along their length and is usually exhibited in steels with elongated inclusions or particle clusters. The formation is known to promote ductility, but it can also cause ductile delaminations. [16]

2.4.4 Ductile Crack Growth

The initial crack opening, δ_0 may under static load create a plastic zone at the crack tip and initiate a crack tip blunt. The stress concentration at the crack tip will exceed the yield strength and favour nucleation of voids at second-phase particles near the crack tip.

The crack tip opening displacement, δ and the distance between the inclusions and voids will determine the nucleation sites which in turn depend on the amount of stress triaxiality ahead of the crack tip where the plastic strain is quite intense. [106] When the void becomes large enough and the distance from the crack tip becomes small enough, plastic localisation and coalescence between the void and the crack tip will prevail. Dependent on the void size, the strain hardening capacity, and the initial volume fraction of voids, four types of void coalescence can occur; multiple void interactions, void by void coalescence, shear coalescence (zig-zag) or diffuse damage zone. The void coalescence types are exhibited in **Figure 2.7**.

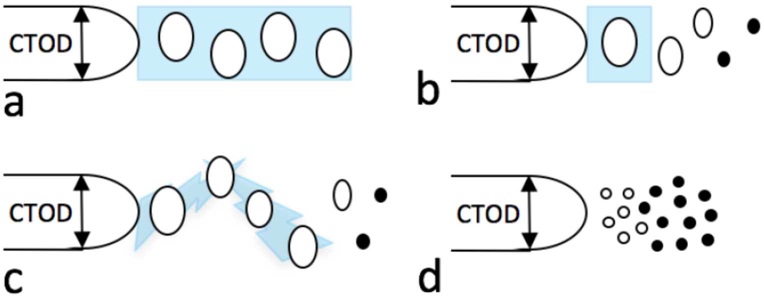

Figure 2.7: a: Multiple void interactions, b: Void by void coalescence
c: Shear coalescence (zig-zag), d: Diffuse damage zone.

Multiple void interactions occur when the porosity level is sufficient to let the void in the vicinity of the crack tip grow at the same rate as the adjacent void. The interaction with the first voids leads to higher stress concentration in the voids further away from the crack tip which in turn yields a higher aggregate growth rate. Thus, the increased growth rate leads to coalescence between several voids. [139]

Void by void coalescence does usually occur when the metallic alloys have an initial void volume fraction smaller than 10^{-2}. Indifference to multiple void interactions, the void at the crack tip does not affect the growth rate of the adjacent void. [106]

Shear coalescence happens in an early shear localisation process between the blunted crack tip and an adjacent void which in turn is harmful to the fracture toughness where there is less plastic work than full void growth and coalescence. It might occur in fracture process zones under plane strain which often promotes a zig-zag void by void coalescence pattern ahead of the crack tip as exhibited in **Figure 2.7 c**. [106]

Diffuse damage zone contains a high number of voids at the crack initiation points during the fracture process, and the voids can cause resemblance to a damage volume element in a notched tensile specimen rather than at a crack tip. Thus, the first coalescence might not occur at the crack tip but as a damage volume element, unlike the three other void coalescence mechanisms. Some materials might experience diffuse damage zone mechanisms at crack initiation and later yield one of the other three mechanisms as the crack propagates. Hence, the crack tip stress and strain field might change as the crack propagates which in turn influences the ductile-to-brittle transition as discussed in Section 2.7. [106]

2.5 Flat to Slant Fracture Transition

When a ductile fracture of sheet material occurs, the fracture initiation often commences as a flat triangular region normal to the loading condition. When the triangle forms, the whole crack will tilt and form a slant with an angle of 45° with the loading. [92] The flat to slant transition and the slant propagation might indicate the change from high triaxiality void growth to a more shear-dominated coalescence. [90] In the slant area, dimples and secondary dimples form, and in combination with a sharp notch will in turn yield higher mean stress and promote void growth. [28] However, experimental results indicate that fracture at grain boundaries or shear decohesion mechanisms might be dominant in a slant fracture. [48][29][84]

Modelling the flat to slant fracture transition is challenging as most models assume a flat fracture and it is hard to reproduce the flat to slant fracture transition since the macroscopic load and the fracture path cannot be reproduced concurrently. [28][91][26][156][157] The modified Gurson model (see Section 3.2.1) describes the void growth at both low and high stress triaxiality and can be utilised to model shear fracture in a flat to slant fracture transition. [92]

Flat to slant fracture transition is often less likely to occur when the material has endured high work hardening, but the transition might be more likely to happen under plane strain with additional damage by local stresses and strain in the stable tearing region. [20] When using continuum damage mechanism models such as Gurson [53] with extensions, the crack path changes in 2D plane strain and only slant fracture is simulated. [20]

2.6 Fracture Mechanics

Structures generally fail due to negligence during the structural design process, or when introducing new material or design. Ductile materials yielding brittle fracture with catastrophic consequences demonstrate the need for a better understanding of fracture mechanics. What is the maximum crack size the material can sustain safely, what is the strength of the material as a function of crack size, or how does the crack size relate as a function of time and applied loads? These are typical questions in fracture mechanics where scientists try to fit experimental research to understand the complexity of the fracture driving forces.

2.6.1 Stress Field

Microscopic cracks and flaws in the material produce concentrated stress fields where the stresses decrease with the distance from the crack tip. If assuming isotropic elastic material behaviour, Sneddon [130], Westergaard [61], Williams [88] and Irwin [52] derived an equation to deduce a closed-form expression for the stresses in the body as shown in Equation 2.13. [4] It is defined in a polar coordinate system with the crack tip as the origin and exhibits the stress field in linear elastic cracked bodies.

$$\sigma_{ij} = \Big(\frac{k}{\sqrt{r}}\Big) f_{ij}(\theta) + \sum_{m=0}^{\infty} A_m r^{(\frac{m}{2})} g_{ij}^{(m)}(\theta) \tag{2.13}$$

σ_{ij} is the stress tensor, f_{ij} and g_{ij} are dimensionless functions of θ, k is a constant, A_m is the amplitude. r and θ are the distance and angle from the crack tip to the applicable stress field in the body. m depends on the geometry but since the stress tensor is proportional to $1/\sqrt{r}$, the leading term will approach infinity as r approaches 0. Thus, a stress singularity is happening in front of the crack tip with a local stress asymptote at r = 0 which implies that the material will fail at any given applied load. Hence, Section 2.6.2 introduces the stress intensity factor in order to deal with this issue. [4]

2.6.2 Stress Intensity Factor

The stress intensity factor, K is a fracture mechanics quantity that governs the stress field at the crack tip and is used as a scaling factor to treat the singularity issue of $1/\sqrt{r}$ as mentioned in Section 2.6.1. The constant k in Equation 2.13 can be substituted with the stress intensity factor, $K = k\sqrt{2\pi}$ which deduces Equation 2.14 for all modes. Thus, the stress intensity factors K_I, K_{II} and K_{III} can respectively be calculated for the three different fracture modes; opening, in-plane shear and out-of-plane shear. [4]

$$\lim_{r \to 0} \sigma_{ij}^{(I)} = \Big(\frac{K_I}{\sqrt{2\pi r}}\Big) f_{ij}^{(I)}(\theta) \tag{2.14}$$

The stress intensity factor defines the amplitude of the crack tip singularity. Thus, the stress and strain near the crack tip are directly proportional to K_I. If the magnitude of K is known, it can ultimately define the conditions at the crack tip and solve for all components including strain, stress, and displacement as a function of r and θ. Hence, the stress intensity factor is an essential concept in fracture mechanics which can comprehensively assess the singularity issue at the crack tip.

With tensile stress normal to the crack plane (mode I loading), K_I can be defined as in Equation 2.15 and 2.16 where P is the force, S is the distance between the applied loads, B is the specimen thickness, W is the width of the specimen, a is the crack depth, and $f(\frac{a}{W})$ is a dimensionless function dependent on the mode of loading and the geometry. For a SENB fracture mechanics test (see Section 5.2), its dimensionless function can be defined as in Equation 2.16. [132]

$$K_I = \frac{P}{B\sqrt{W}} f(\frac{a}{W}) \tag{2.15}$$

$$f(\tfrac{a}{W}) = \frac{3\frac{S}{W}\sqrt{\frac{a}{W}}}{2(1+2\frac{a}{W})(1-\frac{a}{W})^{3/2}} \Big[1.99 - \tfrac{a}{W}(1 - \tfrac{a}{W})\Big\{2.15 - 3.93(\tfrac{a}{W} + 2.7(\tfrac{a}{W})^2)\Big\}\Big] \tag{2.16}$$

The definition of the stress intensity factor is given in many forms and can always be related to the crack with the appropriate correction factor as exhibited in Equation 2.17,

$$K_{(I,II,III)} = Y\sigma\sqrt{\pi a} \tag{2.17}$$

where a is half the crack length, Y is a dimensionless constant which depends on geometry and mode of loading, and σ as the characteristic stress. [4] However, the material's resistance to brittle fracture with a crack present can be defined as the critical fracture toughness, K_{Ic} which in turn is related to the critical fracture stress as described in Equation 2.18 and 2.19.

$$K_{Ic} = \sigma_c\sqrt{\pi a_c} \tag{2.18}$$

$$\sigma_c = \sqrt{\frac{2E\gamma_s}{\pi a_c}} \tag{2.19}$$

a_c is the critical crack length equal to half the length of the internal crack, E is the Young's modulus, γ_s is the specific surface energy, and σ_c is the critical fracture stress required for crack propagation.

Brittle materials usually have low K_{Ic}, and ductile materials typically have a higher fracture toughness as the fracture toughness describes the ability to resist brittle fracture. Since brittle materials do not have any significant plastic deformation at the crack tip, the material will be exposed to brittle fracture. Hence, K_{Ic} is only applicable for brittle materials as ductile materials are in an elastic-plastic range with additional fracture toughness parameters as described in Section 2.6.4. [60]

2.6.3 Geometry Constraint Effects

The constraint effects are usually considered as specimen configurations and loading conditions which influence the crack-tip field. The highly strained area around the crack tip is constrained by the surrounding material which in turn affects the crack growth and fracture behaviour due to the stress triaxiality state. As the fracture toughness dependence relates to the specimen configuration and loading conditions, the constraint effects can be considered as the inhibition of plastic flow. [128] It enhances the material degradation and elevates the local stress which in turn will make it easier to exceed the critical fracture stress.

Two-parameter fracture theory [9][8][21] is developed for elastic-plastic materials to quantify the constraint levels for different geometries and loading conditions. Single edge notched bending (SENB) specimens with $a_0/W = 0.5$ ratio have a high geometry constraint level which yields high conservatism in critical engineering assessments, but it is difficult to know the degree of conservatism as the geometry constraint is highly material dependent. [153][154]

By reducing the specimen size, the constraint effects will diminish and the toughness increases accordingly, thus, decreasing the specimen size can increase the crack growth resistance of SENB specimens [153]. The constraint level is in this manner dependent on factors such as geometry, material thickness, material properties, and crack location relative to external boundaries. [98] Specimens with longer crack ligaments will have less crack tip constraint effects than deeper notched specimens, and a significant loss of constraint effect is exhibited when the local plasticity zone at the crack tip merges with the global plasticity in the specimen which in turn results in constraint relaxation. [154]

The constraint effects in fracture mechanics have been thoroughly investigated the last decades, and to accurately quantify the constraint effects on near crack-tip stress fields, Betegon and Hancock [21] proposed the T-stress, and O'Down and Shih [99] introduced the Q-parameter. However, there are still challenges when determining constraint modified fracture toughness between geometries and different constraint levels. The scaling of fracture toughness between geometries is proposed by Ruggieri and Dodds [122] by utilising a Weibull-based Beremin model [18] (see Section 3.1.3) to account for the scatter variation. Wallin [143] later proposed a constraint modified version by utilising a master curve approach to account for changing material characteristics with shifting temperature. Knott [72] discussed the challenges with inhomogeneous microstructures in the HAZ (see Section 2.2.1) which resulted in wide fracture toughness scatters for different

HAZ regions. In recent years, thermal weld simulation has been utilised to obtain a homogeneous microstructure in order to determine the fracture toughness in the different HAZ regions. [1] [102] The weld simulation is thus able to mimic brittle characteristics in the HAZ with homogeneous microstructure. The fracture toughness is not recognised as an intrinsic material parameter as it is influenced by mode of loading and geometry as discussed in Section 2.7. However, the shifting fracture toughness relates to the so-called constraint effect. [101]

The transversal stress (T-stress) is often utilised to describe the crack tip geometry constraints. O'Dowd and Shih [99] and Dodds et al. [40] described a relationship between the T-stress and the stress triaxiality near the crack tip. When the T-stress is positive, the stress triaxiality remains high, and negative values of T-stress rapidly decrease the stress triaxiality for $K_I - T$-controlled far-fields in elastic-plastic materials. Both K_I and T-stress can be determined for particular specimens and may deduce relevant information about the specimen's dimensions and constraint level. The dimensionless biaxiality ratio

$$\beta = \frac{T\sqrt{\pi a}}{K_I} \tag{2.20}$$

is thus defined to quantify the crack tip constraint changes for different types of fracture specimens with a normalised T parameter. [76] The biaxiality ratio is related to Equation 2.17 where the reference stress is normalised to T and the stress biaxiality ratio as described in Equation 2.20. By defining the T-stress with a Williams series of the crack displacement field, the biaxiality ratio can yield geometry independence with a critical transition of the crack path stability behaviour. [76]

2.6.4 Additional Fracture Toughness Parameters

The crack tip opening displacement (CTOD) was first introduced by Wells [148][149] when he noticed that as a result of plastic deformation and blunting at the crack tip, the fracture surfaces moved apart prior to fracture as shown in **Figure 2.8**. The blunting increases in proportion to the toughness and the CTOD could be utilised to measure the fracture toughness at the crack tip. CTOD is the most commonly used fracture toughness parameter and can also be utilised as a fracture criterion where the material fails at $\delta = \delta_c$. However, the critical CTOD is highly dependent on temperature and constraint level as discussed in Section 2.6.5 and 2.7.

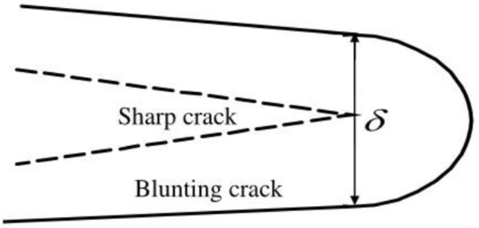

Figure 2.8: Finite displacement (CTOD, δ) at the crack tip with an initially sharp crack yielding plastic blunting prior to ductile tearing initiation. [4]

A generic expression of CTOD can be described as in Equation 2.21 and relates to the stress intensity factor, K_I and the yield strength, σ_{ys}. For plane stress conditions, m = 1.0 and E' = E, while for plane strain conditions, m = 2.0 and E' = E' as described in Equation 2.21 [4]. v is the Poisson's ratio, a_0 is the initial crack depth, W is the width of the specimen, and r_p is the rotational factor assumed to be equal to 0.44.

$$CTOD = \frac{K_I^2}{m\sigma_{ys}E'}, \quad E' = \frac{E}{1-v^2} \tag{2.21}$$

$$CTOD_{el+p} = \frac{K_I^2}{m\sigma_{ys}E'} + \frac{r_p(W-a_0)CMOD}{r_p(W-a_0)+a_0} \tag{2.22}$$

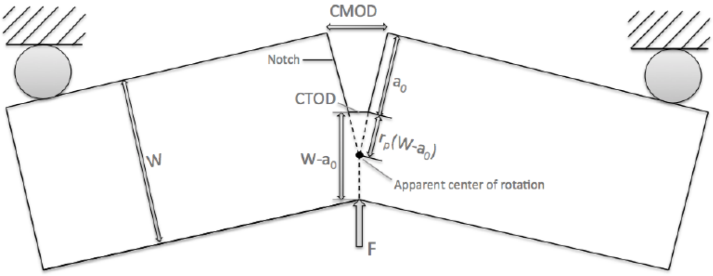

Figure 2.9: Single edge notched three-point bend specimen (SENB) [4]

The hinge model for notched three-point bend specimens as exhibited in **Figure 2.9** can be utilised to determine CTOD values from measurements of the crack mouth opening displacement (CMOD). The total CTOD value can be calculated by using Equation 2.22 where both elastic and plastic deformation has occurred. The CTOD can be separated into two parts where the first component is elastic CTOD which relates to the stress intensity factor K_I. The second component is the plastic CTOD which is related to **Figure 2.9** as a function of CMOD and the rotational factor. [4]

In addition to the CTOD, J-integrals are determined from all fracture mechanics tests. The J-integral value is defined as

$$J = \frac{K_I^2}{E'} = m\sigma_{ys}\delta \tag{2.23}$$

where E' is the Young's modulus in Equation 2.21, δ is the CTOD, and m is the correction factor for plane stress or strain. In theory, $m = 2.0$ for plane strain and $m = 1.0$ for plane stress, however, Hauge and Holm [59] demonstrated an average m-factor at about 1.5 for varying constraint levels of weld simulated steels. Nevertheless, if the fracture specimen has endured plastic deformation, the area under the Force-CMOD curve, A_{pl}^{CMOD} can be used to calculate the critical J-integral, J_c with the estimation procedure by Kirk and Dodds [70] expressed as

$$J = \frac{K_I^2}{E'} + \frac{\eta_{J_c}}{Bb}A_{pl}^{CMOD} \tag{2.24}$$

where b is the length of the remaining crack ligament $(W - a)$, and η_{J_c} is the non-dimensional eta factor for CMOD defined as

$$\eta_{J_c} = 3.75 - 3.101\frac{a}{W} + 2.018\left(\frac{a}{W}\right)^2 \qquad , \frac{a}{W} \in [0.05,\ 0.70] \tag{2.25}$$

2.6.5 Resistance Curves

A plot of a fracture mechanics parameter as a function of crack extension is called a resistance curve, or R-curve. The resistance curve is often utilised to illustrate stable or unstable crack growth with a fracture toughness parameter such as K_I, J or CTOD along the y-axis, and crack growth, Δa along the x-axis. Thus, the R-curve illustrates how the fracture toughness changes as a function of crack extension during plastic blunting and ductile tearing.

Figure 2.10 exhibits a steady-state region after a certain amount of crack growth which means the material will not fail if the characteristic fracture toughness (K_I, J or CTOD) is under the critical fracture toughness value, $CTOD_R^{SS}$. Thus, the crack propagation becomes unstable immediately after the characteristic value exceeds the critical fracture toughness which in turn initiates unstable crack growth and ultimate failure. Brittle materials have flat resistance curves as the surface energy is an invariable material property, [4] hence, the material will fracture when the characteristic fracture toughness exceeds the corresponding resistance curve.

Ductile materials usually have sloped resistance curves where the driving force rate must be higher than the resistance curve in order to get unstable crack propagation. Thus, the structure will ultimately fail when the driving force rate is tangent to the resistance curve. The rising resistance curve trend is usually due to the evolving plastic zone ahead of the crack tip as it requires increasing driving forces in order to maintain the crack growth. If the plastic zone is too small compared to the body, the fracture resistance will reach a steady-state value where the resistance curve remains flat. [4]

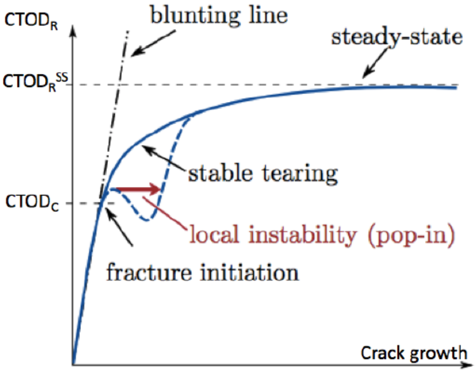

Figure 2.10: CTOD vs Δa, resistance curve phases [63]

Figure 2.10 exhibits a typical crack growth resistance curve for a semi-infinite crack with $CTOD_R$ (CTOD resistance) as a function of crack growth, Δa. The straight blunting line is often followed by stable tearing and steady-state as the crack tip field moves correspondingly along the crack plane at a constant CTOD with increasing crack growth. According to ASTM E 1290 [12], a pop-in may happen when local instability occurs at configurations where the crack growth resistance decreases locally. Thus, the crack will propagate dynamically until it arrests and follows the resistance curve once again with further crack growth. [63] The SENB fracture mechanics test results are somewhat conservative which in turn produce relatively straight fracture resistance curves when only incorporating ductile tearing. The constraint effects will increase in the process zone as the compressive field and crack propagation decrease the crack ligament which in turn yields a flattening effect of the resistance curve.

2.7 The Ductile-to-Brittle Transition

The fracture toughness of steels is temperature dependent where the material exhibits a transition going from low fracture toughness at low temperatures with brittle behaviour, to high fracture toughness at higher temperatures with ductile behaviour. As previously discussed in Section 2.4 about ductile fractures, the voids nucleate at second-phase particles, voids grow as the material plastically yields, and finally, the voids coalesce as shown in **Figure 2.5**. These plastic deformation mechanisms are immensely energy-consuming and result in high fracture toughness and exhibit a high tolerance for initial flaws.

By reducing the temperature, the mobility of dislocations decreases, and it is required an increased level of stresses in order to move them which in turn will decrease the plastic deformation. At certain lower temperatures, local stresses will be high enough to break the local bonds and initiate brittle fractures as microcracks nucleate at broken second-phase particles. Brittle crack propagation requires considerably less energy consumption compared to the ductile mechanisms. Hence, the material fracture toughness will be significantly lower with decreasing temperature as exhibited in **Figure 2.11**.

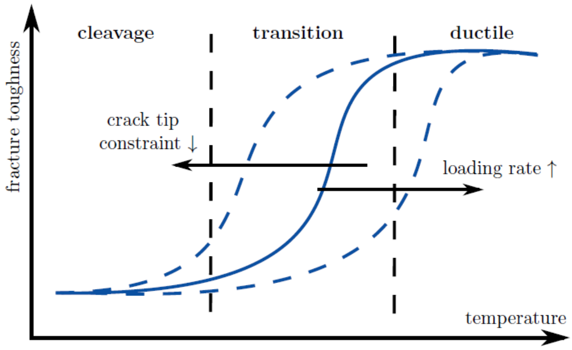

Figure 2.11: Ductile-to-brittle transition curves with shifting loading rate and crack tip constraint level [63]

The transition region in **Figure 2.11** exhibits both ductile and brittle behaviour and the transition temperature is usually determined by factors such as second-phase particles, flaws, and microcracks. Prohibited plastic flow contributes to embrittlement and increases the transition temperature which is highly problematic in Arctic regions with low service temperature where sudden brittle fracture may prevail. The transition temperature also depends on the loading rate where increased loading rate increases the transition temperature. As discussed in Section 2.6.3, the highly concentrated plastic deformation at the crack tip promotes a high stress level in the process zone which in turn yields a higher transition temperature with increasing crack tip constraint levels. [63]

The fracture toughness scatters in the transition region are highly responsive to the geometry and size of the test specimen which makes the essential data collection extremely difficult. Thus, the experimental values may not have the best transferability to large structures. The large scatter in the transition region is due to the competing micromechanisms of fracture where concurrent ductile tearing and cleavage initiation might happen. The fracture toughness is related to the distance from the cleavage initiator to the crack tip where a short distance yields low toughness, and a remote cleavage initiator results in a higher toughness. In some cases, a crack grows by ductile tearing until the crack reaches a microstructural feature which initiates a cleavage fracture. [5] The fracture toughness in the transition region can be significantly affected by the stress triaxiality relaxation (see Section 2.1) at the crack tip due to the geometry and size effects. The plastic flow during ductile tearing leads to constraint relaxation which in turn results in constraint loss and increased fracture toughness up to a factor of six. [5]

2.8 Probabilistic Fracture Mechanics Modelling

Methods in probability theory enable material characterisation of known but apparent random populations of fracture mechanics data by utilising mathematical modelling and probabilistic analyses. Experimental samples can be interpreted and described with statistical models and distributions which further can be used to assume material characteristics by quantifying and illustrating the sample data. Thus, probability distributions and statistical models can describe and predict both randomness and statistically independent fracture mechanical data.

Failure analyses are often utilised to guarantee reliable structures during the structural design process where averaged fracture mechanics data are traditionally utilised to determine material characteristics. The averaged data will give acceptable results in cases of small variations in the fracture mechanics scatter, but for larger scatter band, the results become uncertain and ambiguous. However, lower limit approaches are often used to give safe predictions for material characterisation with large scatter bands where the results remain conservative which in turn leads to expensive material and structure design. Hence, a probabilistic approach is often suggested when predicting failure in structural engineering and to quantify the probability of failure with more reliable risk assessments.

This section will focus on the underlying concepts of the classical Weibull distribution and the theoretical basis of the weakest-link principles in the Weibull approach. [165]

2.8.1 The Weakest-Link Principle

The weakest-link approach is commonly used in probabilistic analyses for continuum mechanics where the weakest-link is based on a mechanical chain of statistically independent components. If one of the statistically independent parts in the mechanical chain fails, ultimate failure occurs. In fracture mechanics, this means the material will ultimately fail if one of the statistically independent elements fails. However, in reliability engineering, the weakest-link approach is usually defined by a series system where all the statistically independent components need to be working for the system to work, and if one of the parts fails, the entire system fails. The reliability (survival probability) of the system can be expressed as in Equation 2.26 where R_i is the reliability of component i in a series system of n statistically independent components.

$$R_{sys} = \prod_{i=1}^{n} R_i \tag{2.26}$$

In general terms, the density of the weakest-links is often distributed with the density function $c = n/l_{ch}$, where n is the amount of weakest links and l_{ch} is the chain length. When l is the finite length of an arbitrary segment, the survival probability is defined as

$$P_S = \left(1 - \frac{l}{l_{ch}}\right)^{cl_{ch}} \tag{2.27}$$

However, as the chain length, l_{ch} is not finite and limits to infinity, the resulting failure probability of an arbitrary segment can be expressed as [71]

$$P_F = 1 - e^{-cl} \tag{2.28}$$

In continuum mechanics, the segments are substituted with statistically independent volume elements containing n defects. When a single defect in one of the volume elements becomes critical due to uniform loading, the whole volume chain fails. By utilising a similar flaw density distribution, $c = n_c/V_0$ where V_0 is the original volume with n_c critical flaws, the failure probability of volume V_0 can be expressed as

$$P_F^{V_0} = 1 - e^{-cV_0} \tag{2.29}$$

When the structure comprises a volume $V = \sum_{i=1}^{N} \Delta V_i$ with N non-overlapping statistical independent volume elements (ΔV_i) containing statistically independent defects, the failure probability of the continuous volume V can be defined as

$$P_F^V = 1 - exp\left(-\sum_{i=1}^{N} c(f)\Delta V_i\right) = 1 - e^{-c(f)V} \tag{2.30}$$

where $c(f)$ is the density function of defects as a function of uniform loading, f. [71] In conclusion, the weakest-link approach is based on the ultimate failure from uniformly distributed statistically independent material defects defined as point defects in statistically independent volume elements.

2.8.2 The Weibull Approach

The density function discussed in Section 2.8.1 was initially introduced by W. Weibull in 1951 [147] as the empirical expression

$$c(f) = \frac{1}{V_0}\left(\frac{f}{f_0}\right)^{m} \quad , f \geq 0 \tag{2.31}$$

where f_0 is the normalising value of the uniform loading, f related to the scaling volume, V_0 and the exponent m characterised as the Weibull modulus. By assuming the material follows the weakest-link principles in Section 2.8.1, the density function in Equation 2.31 substituted into Equation 2.30 leads to the failure probability by Weibull:

$$P_F^V = 1 - exp\left[- \frac{V}{V_0}\left(\frac{f}{f_0}\right)^m \right] \quad , f \geq 0 \tag{2.32}$$

As shown in **Figure 2.12 (a)**, the variability increases with decreasing Weibull modulus, and the failure probability converges to a single point at about 63,2% with constant volume relation regardless of Weibull modulus when considering the failure probability in Equation 2.32 versus the uniform loading, f. In reliability engineering, the Weibull modulus is characterised as the shaping constant and defines the component life phases. For $m < 1$, the component is in its burn-in phase with a downward sloping hazard function, $m = 1$ represents a constant hazard function in its steady life phase, and $m > 1$ represents the component in its wear-out phase with upward sloping hazard function. As the material during fracture mechanics testing experience abnormally high stress and strain, it is most likely to be in the wear-out phase with $m > 1$. However, by changing the volume relation with constant Weibull modulus, the resulting failure probability increases with increasing volume relation as shown in **Figure 2.12 (b)**. [71]

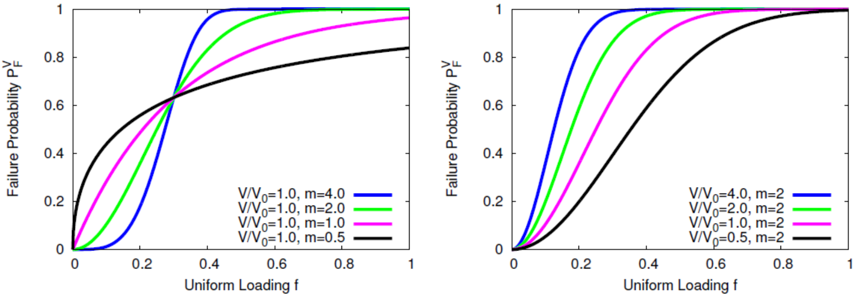

(a) Varying Weibull modulus m. **(b)** Varying volume relation $\frac{V}{V_0}$.

Figure 2.12: Weibull failure probability, P_F^V as a function of uniform loading, f [71]

From Equation 2.32 and **Figure 2.12**, the constituent parameters, f_0, m, and V_0 can a priori be estimated by conducting statistical analysis of experimental results. More recently, scientists such as Beremin [18] has utilised Weibull probabilistic distributions and the weakest-link principles to predict fracture toughness values primarily in the brittle region. More about the Weibull-based Beremin model and the constitutive Weibull parameter calibration schemes in Section 3.1.3 and 5.3.1, respectively.

Chapter 3

Constitutive DBT Models

A range of different models is described in this chapter to characterise the material behaviour in all the ductile-to-brittle transition regions. One model is traditionally utilised to describe the unstable crack propagation with cleavage initiation and another model to describe the plastic deformation and material softening. The chapter will start by introducing the individual models to independently characterise the material behaviour in the brittle and ductile regions, and then present a couple of combined models which can be used to describe the concurrent ductile and brittle mechanisms in the transition region.

3.1 Brittle Region

This section briefly introduces the three most common material behaviour models to predict and visualise the fracture toughness in the lower ductile-to-brittle transition region, or the so-called brittle region. The material models are based on brittle fracture as described in Section 2.3, and cleavage fracture initiation as described in Section 2.3.1.

3.1.1 RKR Criterion

The RKR Criterion developed by Richie, Knott, and Rice [115] is based on the idea that cleavage will occur if the principal stresses along the crack ligament exceed the critical stress over a characteristic distance. The RKR Criterion is established to solve the singularity problem as discussed in Section 2.6.1 and explain why the material did not fail even though the stress concentration approaches infinity at the crack tip. It suggests that brittle failure occurs whenever the stresses perpendicular to the crack ligament exceed the critical opening stress over a characteristic distance along the crack ligament. [4][115]

For unstable crack growth to occur, the original RKR Criterion states the crack must initiate at a grain boundary and propagate to the next grain boundary. Thus, the opening stresses along the crack ligament must exceed the critical opening stress over a distance equal to one grain diameter, and the total characteristic distance necessary for unstable crack growth is considered as two grain diameters. [115]

Another approach is to relate the characteristic distance to a volume element within the plastic zone where all the cracked particles experiencing high enough stress concentration for cleavage initiation are considered. [80] The basis for this behaviour arises as the brittle strength of the material is based on the highest stress in a defined volume exceeding the critical stress. The most probable fraction initiation location may be determined from a statistical fracture model competition between the increasing number of plastic sampling volumes remote from the crack and the high stresses near the crack tip. [14] The latter approach is later set up as a Weibull distribution model as described in Section 3.1.3.

3.1.2 Cohesive Zone Model

A cohesive zone model to describe the brittle behaviour before cleavage initiation has been investigated by scientists such as Kabir et al. [67] and Hardenacke et al. [58]. The cohesive zone model combines two predominant features; the softening effect when the maximum principal stress exceeds the cohesive strength of the ligament, and the work of cohesive separation defined as the work required to drive the microcrack from the broken second-phase particle into a grain and through the next grain boundary.

The cohesive zone model with its constitutive traction-separation law describes the relation between surface traction and local separation where bi-linear and exponential shape laws are used to describe the brittle mechanisms exhibited in **Figure 3.1**. Similarly to the RKR Criterion in Section 3.1.1, the cohesive zone model is dependent on a critical cohesive strength and the maximum principal stresses along the crack ligament. The parameters in the bi-linear and exponential laws are thoroughly discussed by Tvergaard and Hutchinson [138], and Xu and Needleman [155] where they explain how the cohesive zone at the crack tip propagates prior to cleavage initiation. The cohesive work of separation corresponds to the critical energy-release rate which in turn can account for the minimal work required for cleavage. When reaching the critical cohesive strength, the model accounts for the softening and further separation in order to describe the full extent of the cleavage initiation and the minimum work required to yield brittle fracture. [63]

The cohesive laws visualised in **Figure 3.1** defines the relation between the local separation, δ and the surface traction, t along the crack during blunting and crack propagation. The bi-linear law is based on a shape parameter $\lambda \in [0, 1]$ which determines the relationship between the critical cohesive strength and the critical local separation as shown in **Figure 3.1 (a)**. [63]

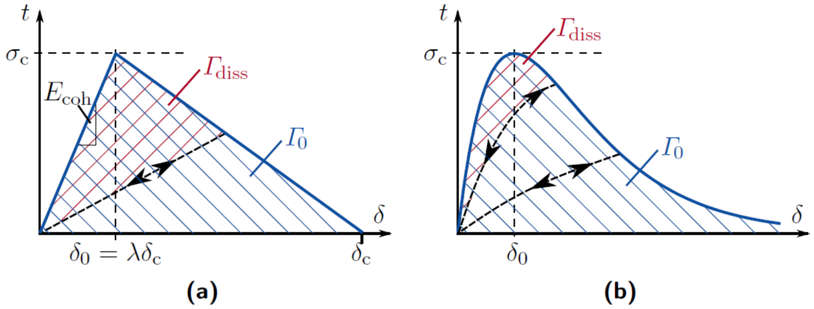

Figure 3.1: Cohesive traction-separation laws. (a) bi-linear, (b) exponential shape. [63]

Regardless of cohesive law, the respective traction-separation laws follow the universal cohesive work of separation envelope described in Equation 3.1.

$$\Gamma_0 = \int_0^\infty \mathrm{t}(\delta)\,\mathrm{d}\delta \tag{3.1}$$

The surface traction, t is a function of local separation, and is for the bi-linear law separated into two discontinuous functions, one for $\delta < \delta_0$, and one for $\delta_0 < \delta < \delta_c$ where δ_0 is the local separation at the critical cohesive strength, σ_c and δ_c is the critical local separation for cleavage. As exhibited in **Figure 3.1 (b)**, the exponential law has continuous surface traction as a function of local separation which reaches the critical cohesive strength at δ_0. Rice [113] defined Γ_0 as the minimum work required for cleavage and corresponds to both the critical energy-release rate and the lower-bound fracture toughness. The exponential cohesive law was initially proposed by Roth and Kuna [117] due to the discontinuous behaviour of the bi-linear law at δ_0 which in turn resulted in a sudden increase in the dissipated work, Γ_{diss} as shown in **Figure 3.1 (a)**. The variable $D = \frac{\Gamma_{diss}}{\Gamma_0}$ is often utilised to represent the total cohesive damage where the material will yield ultimate cleavage when $\Gamma_{diss} = \Gamma_0$. [63]

3.1.3 Weibull-based Beremin Model

The statistical Weibull approach established by Beremin [18] postulates a stochastic distribution of potential cleavage initiation flaws and is a local criterion for cleavage fracture initially introduced by Weibull [147]. By assuming weakest-link behaviour as described in Section 2.8.1, the Weibull stress is derived as a global measure of loading by modelling the flaws as Griffith-cracks. The weakest-link principles constitute the idea of complete failure whenever one of the statistically independent components in a series of components fails. Thus, if cleavage initiates at any flaw, the material will yield complete failure. The Beremin model can a priori be used regardless of constraint effects to describe the experimental fracture toughness scatter. The Weibull stress can be utilised to quantify the constraint effects as the failure probability scales with the Weibull stress meaning the probability of failure with corresponding Weibull stress should be identical regardless of the geometry constraint level.

To numerically predict the large experimental fracture toughness scatter as discussed in Section 2.7, the Beremin model has probably become the most popular local fracture approach in this area. The original approach is based on a hypothesis of temperature independent critical cleavage stress similar to the RKR Criterion (see Section 3.1.1), but is also incorporating statistically distributed Griffith-flaws based on the weakest-link principles in Section 2.8.1. Structural steels usually contain certain populations of defects (M-A Constituents, inclusions and microcracks) which follows a simple power law, $p(a)$. This flaw distribution function is used to calculate the probability of failure for uniformly loaded element volumes, V_0 expressed as

$$P(\sigma) = \int_{a_c(\sigma)}^\infty \mathrm{p(a)}\,\mathrm{d}a \tag{3.2}$$

where $a_c = 2E\gamma_s/\alpha\sigma_c^2$ is the critical half crack length as described in Equation 2.19 substituted with α as a mathematical constant function of the crack shape instead of π.

[105] As shown in Equation 3.2, the probability of failure is calculated after reaching the critical half crack length and with further crack growth.

When weakest-link principles are assumed, all the volume elements which are uniformly loaded can be characterised as V/V_0 statistically independent elements, and the probability of failure in volume V can be expressed as [105]

$$P_F = 1 - exp\Big[-\frac{V}{V_0}P(\sigma)\Big] \tag{3.3}$$

The simple power law, $p(a)$ in Equation 3.2 has been proposed through experimental metallurgical observations of propagated microcracks from defects. For Weibull distributions, the flaw distribution function can be described as an inverse power law defined as

$$p(a) = \gamma a^{-\beta} \tag{3.4}$$

with both γ and β as material constants which in turn leads to the probability of failure:

$$P_F = 1 - exp\bigg[-\frac{V}{V_0}\Big(\frac{\sigma}{\sigma_u}\Big)^m\bigg] \tag{3.5}$$

where the Weibull modulus (shape parameter), m and the scale parameter, σ_u are respectively defined as [105]

$$m = 2\beta - 2 \qquad\qquad \sigma_u = \bigg(\frac{m}{2\gamma}\bigg)^{1/m} \cdot \bigg(\frac{2E\gamma_s}{\alpha}\bigg)^{1/2} \tag{3.6}$$

By assuming microcracks modelled as Griffith flaws and a microcrack size distribution following the inverse power law in Equation 3.4, the Weibull distribution can be expressed as [18] [25] [93]

$$P_F(\sigma_w) = 1 - exp\bigg[-\frac{1}{V_0}\int_{V_{pl}}\Big(\frac{\sigma_1}{\sigma_u}\Big)^m dV\bigg] = 1 - exp\Big[-\Big(\frac{\sigma_w}{\sigma_u}\Big)^m\Big] \tag{3.7}$$

where P_F is the Weibull cumulative probability of failure, m is the Weibull modulus, σ_u is the scale parameter, and σ_w is the Weibull stress determined by the volume size effects and principal stresses in the respective elements near the crack tip as expressed in Equation 3.8. [18] [125] [96] The Weibull distribution in Equation 3.7 is defined with two material dependent parameters, m and σ_u which respectively represent the size of the flaw distribution and the Weibull scale parameter.

$$\sigma_w = \bigg[\int_{V_{pl}}(\sigma_1)^m\frac{dV}{V_0}\bigg]^{1/m} = \bigg[\sum_{i=1}^{n}(\sigma_1^i)^m\frac{V_i}{V_0}\bigg]^{1/m} \tag{3.8}$$

The Weibull stress, σ_w in Equation 3.8 is the random variable in the two-parameter Weibull distribution in Equation 3.7 and must be computed in order to describe the shifting material behaviour during blunting and crack propagation. σ_1 is the maximum principal stress, m is the same Weibull modulus as in Equation 3.7, and V_0 is the initial element volume. V_{pl} is the entire plastic volume of the structure called the fracture process zone (FPZ) as shown in **Figure 3.2** and represents the volume of all elements which have undergone enough plastic deformation to yield a certain probability of slip-induced cleavage due to dislocation pile-ups. The reference volume, V_0 is often set as temperature independent and must be small enough to resolve extreme stress levels ahead of the crack tip and large enough to allow the presence of a critical flaw. [116]

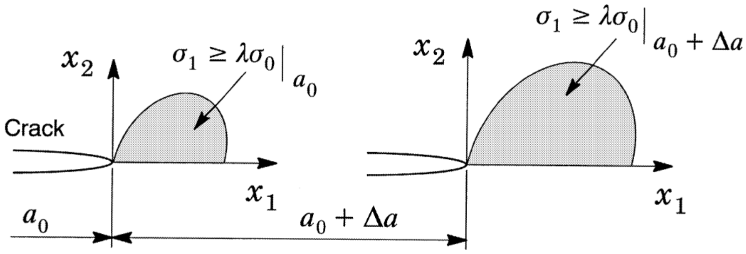

Figure 3.2: Illustration of the FPZ evolution during crack propagation. [96]

As expressed in Equation 3.8, the Weibull stress must be calculated by integrating the maximum principal stresses over the entire FPZ. Nevertheless, as the Beremin model follows the weakest-link principle, the Weibull stress can be determined by calculating the aggregate sum of the maximum principal stresses from all the elements in the FPZ. For a specific time increment, the Weibull stress calculation must account for both volume change and the maximum principal stresses in all the statistically independent volume elements in the fracture process zone.

The FPZ ahead of the crack tip contains potential sites for cleavage initiation and is defined as a highly stressed region with plastic deformation. Ruggieri and Dodds [122] [123] [121] [124] described the FPZ in **Figure 3.2** as the loci where $\sigma_1 \geq \lambda\sigma_0$, $\lambda \approx 2$ was fulfilled. However, Beremin [18] and Mudry [93] defined the FPZ as the plastic region ahead of the macroscopic crack where $\sigma_{eq} \geq \sigma_0$ was fulfilled. As the crack grows, the FPZ evolves accordingly as illustrated in **Figure 3.2** which in turn leads to higher Weibull stress as the crack advances. Fracture geometries with low constraint level experience a significant increase in stress triaxiality ahead of the crack tip during ductile tearing, and fracture geometries with a high constraint level exhibit less stress triaxiality elevation during ductile tearing. Nevertheless, the high stress triaxiality region will expand with increasing crack growth leading to a more prominent FPZ which in turn is more vulnerable to cleavage fracture initiation. [122]

The Weibull parameters, m and σ_u must be separately calibrated and fitted by comparing the simulated Weibull stress with the experimental results which in turn requires a comprehensive calibration scheme in order to get an optimal fit between the probability of failure and the critical Weibull stresses. One of the methods is to utilise a non-dimensional Weibull stress $\bar{\sigma_w} = \sigma_w/\sigma_u$ to define the probability of failure as $P_F = 1 - exp[-(\bar{\sigma_w})^m]$ and fit it to the experimental probability of failure. Rank probabilities of each fracture point are utilised to represent the cumulative probability of failure by ranking the critical Weibull stresses in ascending order, and an approximation scheme such as maximum likelihood estimation or mean least square regression is used to calibrate the Weibull modulus. After the m-value is calibrated from the previous fitting procedure, the Weibull stress, σ_w can be fitted to the $P_{rank} = 63.2\%$ (or $1 - 1/e$) to find the assigned scale parameter, σ_u. [152] Recent studies disclose the best rank probability to estimate the cumulative probability of failure for Weibull distributed materials as the median rank probability $F(i,n) = (i-0.3)/(n+0.4)$, $i \in [1,n]$ for both Monte Carlo simulations with maximum likelihood estimation [45] and logarithmic Weibull representation utilising the mean least square regression method [77] where i is the rank number of n specimens arranged in ascending order. There are several other methods to determine the Weibull parameters, and the whole Weibull parameter study is further described in Section 5.3.1.

The two-parameter Weibull model approach implies that a relatively small fracture toughness or Weibull stress leads to a finite failure probability. However, as discussed in Section 2.3.1, cleavage fracture cannot occur before sufficient energy to break the atomic bonds and crack propagation have endured. Hence, it may exist a threshold limit for the minimum Weibull stress or fracture toughness for which the cracks are completely arrested below this threshold value. By recognising these problems, Anderson et al. [5] made a simplified three-parameter Weibull distribution which approximates the probabilities of crack arrest and propagation expressed as

$$P_F(K_I) = 1 - exp\Big[- \Big(\frac{K_I - K_{min}}{K_0 - K_{min}} \Big)^4 \Big] \tag{3.9}$$

where K_I is the stress intensity factor for a mode I crack, K_0 is the fracture toughness at 63.2% probability of failure, and K_{min} is the threshold fracture toughness estimated to 20 $MPa\sqrt{m}$ for common ferritic steels under SSY conditions. [11] A similar approach is proposed by Wallin [144] who defined K_I in Equation 3.9 as K_{JC} equivalent with the critical fracture toughness corresponding to P_F. Wallin suggested a master curve approach where K_0 changes with temperature by calibrating a reference temperature, T_0 for each specimen geometry by utilising a K_0 estimation scheme based on censored fracture toughness data. However, Gao et al. [47] substituted all the stress intensity factors in Equation 3.9 with corresponding Weibull stresses and introduced a new threshold Weibull stress, $\sigma_{m,min}$ in the Weibull cumulative distribution function

$$P_F(\sigma_w) = 1 - exp\Big[- \Big(\frac{\sigma_w - \sigma_{w,min}}{\sigma_u - \sigma_{w,min}} \Big)^m \Big] \tag{3.10}$$

where $\sigma_{m,min}$ is defined at the time increment where $K_I = K_{min}$ (in plane-strain), and assumes that cleavage fracture cannot occur below this threshold Weibull stress value ($\sigma_w < \sigma_{w,min}$) due to crack arrest and lack of energy dissipation. Nevertheless, if the thickness of the fracture mechanics test specimens remains identical, the threshold stress can simply be defined as $\sigma_w^* = \sigma_w - \sigma_{m,min}$ and can a priori follow the same parameter calibration procedure as the two-parameter Weibull model. [47]

If small-scale yielding (SSY) conditions are fulfilled, the original Beremin theory can describe the real probability to failure as

$$P_F = 1 - exp\Bigg[- \frac{\sigma_0^{m-4} K_{IC}^4 B C_m(n)}{V_0 \sigma_u^n} \Bigg] \tag{3.11}$$

where P_F is the cumulative probability to failure, σ_0 is the yield strength, B is the specimen thickness, V_0 is the volume of the mesh element at the crack tip, and K_{IC} is the fracture toughness for a given probability. $C_m(n)$ can be expressed as

$$C_m(n) = \int_{-\pi}^{\pi} g_{\theta\theta}^{m}(\theta) d\theta \int_{0}^{\alpha(\theta)} f^m(u) u du \tag{3.12}$$

with Δu steps related to the mesh element length, stress intensity factor, and yield strength. Equation 3.11 is found in the ASTM standards [11] and can describe the size effects and the fracture toughness with changing temperature, specimen thickness, and yield strength. The whole criterion can be implemented into computer programs to compute equal probability distributions. [104]

3.2 Ductile Region

This section describes The Complete Gurson Model which in turn can be utilised to simulate the ductile material softening mechanisms as described in Section 2.4. The ductile damage model has shown to be able to describe the fracture toughness in the upper ductile-to-brittle transition region or the so-called ductile region. Several models have been developed over the last decades in order to describe the ductile mechanisms, and some of them exhibit noticeable results in the ductile region. One of the most common ductile models is developed by Rousselier [118] [119] which is based on constitutive relationships including coalescence and cavity growth for accurate material characterisation and good transferability of material data to cracked structures. The Rousselier model comprises similarities with the Gurson model discussed in Section 3.2.1 as the Rousselier model is based on a local approach to fracture and damage mechanisms by predicting the effect of inclusion content and temperature concerning ductile fracture. [118] Both Rousselier and Gurson are plasticity theories utilised to describe the material softening with continuum mechanics composing idealised growth of voids. Other ductile models are usually based on the original Gurson model [53] with extensions such as The Complete Gurson Model described in Section 3.2.1 and other non-local Gurson models. [111] [64]

3.2.1 The Complete Gurson Model

As discussed in Section 2.4, a ductile fracture is often a result of void nucleation, void growth, and void coalescence as engineering steels contain inclusions and second-phase particles which nucleate micro-voids during plastic deformation. The most commonly used model for elastic-plastic materials to simulate and describe the ductile mechanisms is the model initially developed by Gurson [53] and later modified by Tvergaard and Needleman [136][140][137]. The original Gurson model only accounts for void nucleation and void growth, and the coupling between plasticity and damage which can reflect the voids' softening effect. When Tvergaard and Needleman introduced the critical void volume fraction, the model considered the impact of void coalescence and is also known as the Gurson-Tvergaard-Needleman (GTN) model. They were able to avoid the problem of complete material loss Gurson initially had and modified the homogeneous yield function as expressed in Equation 3.13.

$$\phi(q_{vm},\sigma_f,f,\sigma_m) = \frac{q_{vm}^2}{\sigma_f^2} + 2q_1 f cosh\Big(\frac{3q_2\sigma_m}{2\sigma_f}\Big) - 1 - (q_1 f)^2 \tag{3.13}$$

σ_m is the mean stress, f is the void volume fraction, q_{vm} is the von Mises stress, and σ_f is the flow stress of the matrix material. q_1 and q_2 are parameters introduced by Tvergaard and Needleman [136][137] in order to modify the original Gurson model [53] and is respectively equal to 1.5 and 1.0. As the yield function depends on the void volume fraction, both void nucleation and void growth parameters are essential. Equation 3.14 illustrates the strain-controlled nucleation where f_ϵ is the void nucleation intensity, and $\bar{\epsilon}^p$ is the equivalent plastic strain. Due to the incompressible nature of the matrix material and the requirement of a volume preserving plastic flow of the matrix material, the growth rate of existing voids can be expressed as in Equation 3.15 where ϵ^p is the plastic strain tensor, and **I** is the second-order unit tensor known as the Kronecker delta, δ_{ij}.

$$df_{nucleation} = f_\epsilon(\bar{\epsilon}^p)d\bar{\epsilon}^p \tag{3.14}$$

$$df_{growth} = (1-f)d\epsilon^p : \mathbf{I} \tag{3.15}$$

However, the GTN model did not have physical mechanisms based on void coalescence criterion which is required when utilising realistic micro-void parameters. [41] Thomason's plastic limit load model for coalescence [134] is one of several coalescence models [103][50][15] which can be used to complete the GTN model. Thomason argued that void nucleation and growth competed with localised void coalescence and the homogeneous deformation phase could shift to the localised deformation phase at a critical moment. For 2D strain problems, the limit can be expressed as in Equation 3.16 where σ_f is the flow stress, and σ_1 is the maximum principal stress. R and r are the current average void radius and intervoid distance calculated from principal strains (see Appendix A.2).

$$\begin{aligned} \frac{\sigma_1}{\sigma_f} &< \frac{0.3}{r/(R-r)} + 0.6 \quad \textit{no coalescence} \\ \frac{\sigma_1}{\sigma_f} &= \frac{0.3}{r/(R-r)} + 0.6 \quad \textit{coalescence starts} \end{aligned} \tag{3.16}$$

Zhang et al. [160] combined the GTN model for void growth and Thomason's plastic limit load model for coalescence and created The Complete Gurson Model. With the complete model, the critical void volume fracture, f_c can be determined automatically from the plastic limit load model and does not need to be fitted as a material parameter which in turn means the ductile fracture is only linked to void nucleation parameters. Zhang usually applies a cluster nucleation model which assumes all the microvoids will nucleate at the beginning of plastic deformation and the void volume fraction is exclusively from the growth of existing voids following Equation 3.15. [160] In FEA, the mesh size is solely related to the material characteristic length parameter and can thus link the mesh size directly to the material in The Complete Gurson Model.

Tvergaard and Needleman [136] simulated artificial acceleration of the void growth, f^* as post-coalescence deformation behaviour which in turn resulted in the modification of the yield function to account for final material failure by substituting the void volume fraction, f in Equation 3.13 with f^* as expressed in Equation 3.17.

$$f^* = \begin{cases} f & for \quad f \leqslant f_c \\ f_c + \frac{f_u^* - f_c}{f_F - f_c}(f - f_c) & for \quad f > f_c \end{cases} \tag{3.17}$$

$f_u^* = 1/q_1$, f_0 is the initial void volume fraction, f_c is the critical void volume fraction, and f_F is the void volume fraction at the end of coalescence defined as $f_F = 0.15 + 2f_0$. When the void volume fraction reaches the critical value f_c, the artificial acceleration of the void growth, f^* substitutes f in Equation 3.13 after which the load bearing capacity drops rapidly.

3.3 Transition Region

The transition region in the ductile-to-brittle transition of steels has proved to be extremely challenging but crucial to characterise and predict. A range of different approaches has been tested by several scientists the last three decades, and most of the simulation schemes comprise one model to describe the ductile mechanisms in Section 2.4, and a post-processing model to predict the occurrence of brittle fracture as described in Section 2.3. The most common models to describe ductile mechanism are the Rousselier model and the Gurson model as discussed in Section 3.2, and the usual post-processing models are the RKR Criterion and Weibull-based Beremin models as described in Section 3.1. Also, the cohesive zone model described in Section 3.1.2 can be utilised to define the minimum work required for brittle fracture combined with for example non-local Gurson models. [63] There are several other model combinations to predict the concurrent ductile and brittle mechanisms in the transition regions, and two of them are the Gurson-RKR approach described in Section 3.3.1, and the Beremin-Gurson approach described in Section 3.3.2.

3.3.1 RKR and Gurson

The Combined Gurson-RKR Model is based on the RKR Criterion in Section 3.1.1 and The Complete Gurson Model in Section 3.2.1. The RKR Criterion is implemented to identify cleavage initiation as a post-processing routine combined with The Complete Gurson Model. The RKR Criterion as a post-processing routine is based on two parameters, the critical opening stress and the characteristic distance along the crack ligament. If the opening stresses ahead of the crack tip exceed the critical opening stress over the entire characteristic distance, the material will fail by cleavage fracture. The criterion solves the singularity complication at the crack tip as discussed in Section 3.1.1 by considering opening stress evolution along the crack ligament instead of a singularity point at the crack tip. The RKR Criterion is based on the critical stresses at the lowest temperature in the brittle region exhibiting solely brittle behaviour and are initially defined as temperature independent. The critical opening stresses are further characterised as material parameters by utilising a Gurson UMAT (see Section 5.4) as the FE-model material to predict when the material fails by cleavage in the transition region. Temperature dependent critical opening stresses can be approximated in order to visualise the ductile-to-brittle transition regions and to identify the transition temperature.

The temperature dependent true plastic flow curves from all the uniaxial tensile tests are first incorporated as material properties in the original ABAQUS CAE model. From the resulting ABAQUS database file (.odb), a path along the crack ligament is defined to analyse the stresses perpendicular to the crack ligament. The characteristic fracture toughness at the lowest temperature in the brittle region is chosen based on the BS 7910 Standard [30]. For instance, the standard characterises the second lowest fracture toughness value as the MOTE value when considering a fracture tests series comprising six specimens as described in Appendix D.4. In ABAQUS, the Force-CMOD curve should coincide with the experimental results if the material properties from the uniaxial tensile tests are properly fitted. When analysing 2D FE-models in ABAQUS, the simulated mid-point force will be 20 times less than the experimental force due to symmetry and unit thickness (for 10x10mm^2 SENB specimens). By utilising the path function in ABAQUS, the opening stress as a function of true distance from the crack tip along the ligament can be extracted from the critical time increment where the FE-model simulates the critical fracture toughness. The characteristic distance from the applicable opening stress at the lowest temperature in the brittle region is the fundamental basis for the whole simulation scheme. The same method can be utilised by substituting the critical fracture toughness with the critical force. Nonetheless, the time increment from the critical fracture toughness method should a prior be identical to the time increment from the critical force method as the simulated Force-CMOD curve fits the experimental Force-CMOD curve.

Determining the RKR Parameters

The parameters for the RKR criterion are the characteristic distance, x_c and the critical opening stress, σ_c. By utilising the critical time increment from either the critical fracture toughness or force, the opening stress as a function of true distance from the crack tip is plotted accordingly as shown in **Figure 3.3**. The critical distance, x_c should a priori be determined from the microstructure corresponding to two grain diameters as discussed in Section 2.3.1. Nevertheless, the characteristic distance is in the current RKR Criterion defined as a material fitting parameter from which the critical opening stress can be found. Once the characteristic distance is chosen, the critical opening stress, σ_c can be defined as the highest stress where the opening stress, σ_{22} is maintained over the entire characteristic distance, x_c as shown in **Figure 3.3**.

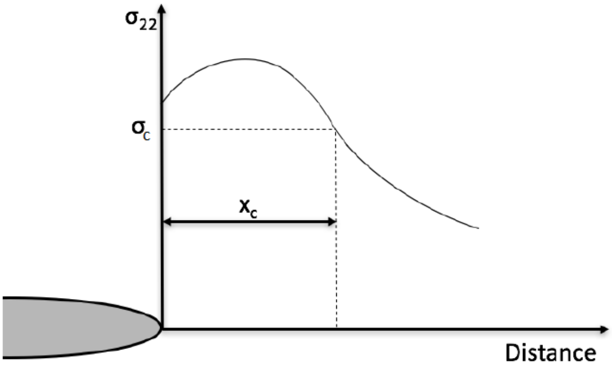

Figure 3.3: Opening stress as a function of true distance from the crack tip [4]

The critical opening stress and the characteristic distance at the lowest temperature in the brittle region are initially used as the fracture criterion for all temperatures when considering the critical opening stress as temperature independent. Thus, cleavage fracture initiation is in all the ductile-to-brittle transition regions identified at the first time increment where the opening stresses exceed the critical opening stress over the entire characteristic distance. From the applicable critical time increments, the fracture toughness values can be extracted directly from ABAQUS and incorporated as a ductile-to-brittle transition curve. The curve will thus describe when the material yields cleavage fracture at the respective temperatures and act as a conservative cleavage criterion.

However, when considering the critical opening stress as temperature dependent, the critical opening stresses are found at the critical time increment corresponding to the characteristic experimental fracture toughness at the respective temperatures. The critical time increment is thus identified when the simulated fracture toughness reaches the characteristic experimental fracture toughness at the applicable temperatures. The critical opening stress as a function of temperature is then established to deduce a linear approximation of opening stress and temperature. The resulting opening stresses can then be utilised to visualise the full extent of the ductile-to-brittle transition regions and identify the appropriate transition temperatures.

3.3.2 Beremin and Gurson

The Combined Beremin-Gurson Model is based on the Weibull-based Beremin Model in Section 3.1.3 and The Complete Gurson Model in Section 3.2.1. The Beremin model is used to calculate the probability of brittle failure by considering volume elements instead of characteristic distances. The volume elements in the finite element fracture test simulation are defined as statistically independent entities following the weakest-link principles and Weibull distributed volume defects as described in Section 2.8.1 and 2.8.2, respectively. The Beremin model is used as a post-processing routine similar to the RKR Criterion (see Section 3.1.1) but is based on statistical distributed flaws and defects in volume elements instead of characteristic distances. The maximum principal stresses in all the volume elements are calculated by considering the mean stress from all the nodes in each element which in turn independently contribute to the total Weibull stress in Equation 3.8. As the Beremin model originally only predicts brittle failure for fracture specimens in the brittle region without ductile tearing [18], it is imperative to introduce another model which can describe the degradation of the material stress capacity by considering material softening during crack propagation and ductile mechanisms. Hence, The Complete Gurson Model can be utilised to describe the continuum damage processes happening in the transition and ductile regions.

Scientists like Xia and Shih [152], Koers et al. [73], and Rossoll et al. [116] have all utilised a Weibull-based model to predict brittle failure combined with a modified Gurson model describing void-induced material softening in the transition region. Several papers show promising results in the brittle and transition region by considering the void-induced ductile damage and statistically independent defect distribution as shown in **Figure 3.4 (a)**. However, multiple material parameters remain uncertain with increasing temperature, and the ductile region is still not yet fully accounted for in the ductile-to-brittle transition of ferritic steels with concurrent void-induced damage and statistically distributed defects.

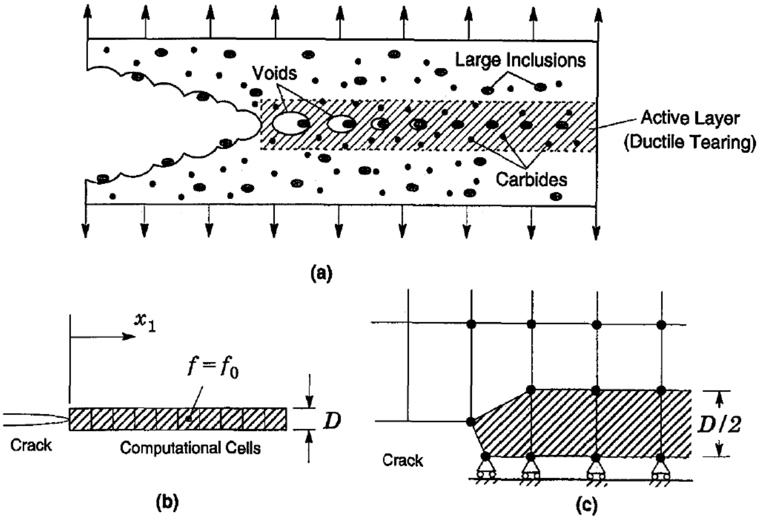

Figure 3.4: (a) Defect and void distribution, (b) Crack ligament and elements with initial void volume fraction, (c) Crack setup with constituent symmetry plane and mesh arrangement [122]

The simulation material in The Combined Beremin-Gurson Model is characterised as a user-defined material (UMAT) constituting cell elements with initial void volume fractions as shown in **Figure 3.4 (b)** which in turn is specified by connecting the experimental resistance curves to the finite element cell volume. **Figure 3.4 (c)** illustrates the mesh arrangement used in the simplified finite element model with squared four-node elements where the Gurson model with its constitutive Gurson parameters are fitted to the experimental resistance curve in the ductile region or the upper transition region. As the Gurson model should provide proper ductile tearing with increasing plastic deformation, the simulated void-induced damage is ideally fitted in the ductile region. In case of insufficient mesh resolution during plastic blunting, a sub-cell averaging scheme by Bilby et al. [23] can be utilised instead of manually reducing the mesh element size.

After the Gurson parameters are fitted in the ductile region or the upper transition region, the Weibull parameters for the Beremin model can be determined. The Weibull modulus is first calibrated through an iterative procedure by fitting critical experimental fracture data in the brittle region with finite element simulated fracture data. In the computational cell model, the ductile crack extension results in cell extinction through void growth and void coalescence within the Gurson UMAT following its yield function (see Equation 3.13). The Gurson UMAT is utilised as the FE-model material in the Weibull-based Beremin model which in turn is used in parallel by independently describing the flaw distribution within statistically independent unit volumes in order to calculate the probability of brittle failure. Thus, The Complete Gurson Model simulates ductile tearing by considering void-containing cell elements and the Beremin model based on weakest-link statistics is incorporated in the cell element model as a post-processing routine to predict the onset of unstable cleavage fracture. Hence, the combined model constitutes an active competition between unstable nucleation of microcracks at flaw interfaces leading to cleavage fracture and nucleation of voids leading to ductile fracture. By accounting for the material softening mechanisms, the opening stress levels ahead of the crack and in the fracture process zone will a priori be substantially reduced which in turn leads to wide confidence intervals.

The success of The Combined Beremin-Gurson Model hinges on the accuracy of the stress field evolution during ductile crack growth. Hence, the Gurson void-induced cell damage model must concurrently and accurately characterise the micro-separation during crack growth in competition with the critical flaw distribution in the transition region. Xia and Shih [152] proposed a cleavage fracture model based on the constraint effects studies by Koers et al. [73] and Wallin [142] which recognised that the amount of tearing depends on microstructure and crack tip constraint. As the ductile tearing is the precursor to cleavage fracture, and both brittle and ductile mechanisms are in competition in the transition region, the predictive approach relies on the accuracy of the ductile crack growth characterisation and constraint relaxation. Hence, the initial void volume fraction, f_0 is fitted in the ductile region to account for the void distribution, and the Weibull modulus, m is calibrated in the brittle region to characterise the flaw distribution of second-phase particles and other defects. The complete simulation scheme will then a priori be able to run computational simulations to predict relationships among probability of brittle fracture, loading, crack growth, fracture toughness, and displacement for the whole ductile-to-brittle transition of ferritic steels. Thus, the combined model can yield better toughness scaling in the transition and ductile regions. Hence, the concurrent ductile mechanisms from the Gurson model and the brittle flaw distribution from the Beremin model can yield good predictions of the fracture toughness scatter band for different geometry constraint levels. More about the parameter studies and the implementation procedures of The Complete Gurson Model and the Beremin model in Section 5.4 and 5.3, respectively.

Chapter 4

Preliminary DBT Model

This chapter comprises the most important discoveries and conclusions from the preliminary work conducted prior to the master's thesis. [126] The initial study is unpublished, and the overall conclusion and discussion are thus presented in full. The final review of the two models is thoroughly described, and less attention is directed to the preliminary findings leading to the final simulation scheme. The initial study is based on The Combined Gurson-RKR Model described in Section 3.3.1 and consists of The Complete Gurson Model (see Section 3.2.1) to simulate material softening, and the RKR Criterion (see Section 3.1.1) as a post-processing routine to predict brittle failure. The simulation scheme considers a separate SENB05 fracture mechanics test series with corresponding uniaxial tensile tests (see Section 2.6.4 and 5.2) conducted at -60$^\circ C$, 0$^\circ C$, and 21$^\circ C$.

4.1 Experimental Data and Material Parameters

SINTEF Industry conducted several fracture mechanics tests and tensile tests at -60$^\circ C$, 0$^\circ C$, and 21$^\circ C$, and by utilising SENB05 ($\frac{a}{W} = 0.5$) specimens with a cross-sectional area equal to 10x10mm^2, the applied load with the corresponding CMOD are concurrently measured during bending. The tests are stopped if the specimen fractures, or unloaded if the specimen reaches a desired CMOD. After the tests are conducted, the specimens are cracked open, and an optical microscope is utilised to measure the plastic blunting and total crack growth. The corresponding CTODs are calculated by utilising the measured CMODs and Equation 2.22. As discussed in Section 3.3.1, the Force-CMOD curve from the characteristic specimen at the lowest temperature in the brittle region determines the critical force and fracture toughness for the failure criterion. The preliminary Force-CMOD curves with all the specimens utilised in this chapter are illustrated in Appendix D.1.

Figure 4.1 exhibits the CTODs from the end of all the fracture mechanics tests. The blue squares are specimens unloaded at desired CMODs, and the red crosses represent fractured specimens. As shown in **Table 4.1**, all the specimens at room temperature are unloaded, while at 0$^\circ C$ and -60$^\circ C$, some specimens fractured and some were unloaded. The total ductile crack growth, Δa and CTOD increases with increasing temperature which in turn illustrates the ductile-to-brittle transition where the steel exhibit brittle characteristics with low fracture toughness at low temperatures, and ductile mechanisms with high fracture toughness at higher temperatures.

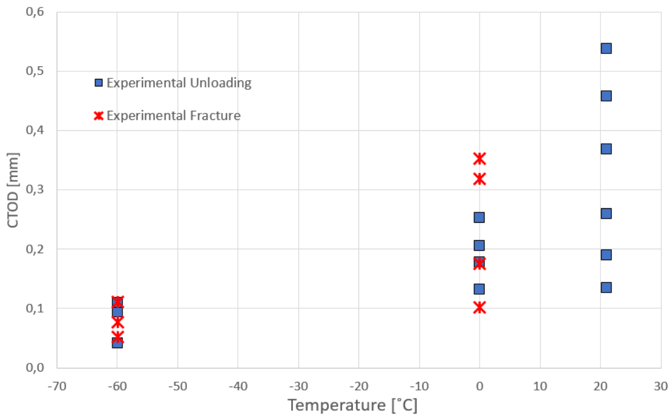

Figure 4.1: SENB05 experimental ductile-to-brittle transition scatter plot

Table 4.1: Experimental CTOD and Δa at unloading and fracture. F = Fracture, U = Unloading

-60$^{\circ}C$			0$^{\circ}C$			21$^{\circ}C$		
CTOD mm	Δa mm	Mode F/U	CTOD mm	Δa mm	Mode F/U	CTOD mm	Δa mm	Mode F/U
0.111	0.07	F	0.205	0.23	U	0.259	0.22	U
0.094	0.08	U	0.318	0.39	F	0.538	0.89	U
0.052	0.05	F	0.353	0.47	U	0.368	0.51	U
0.076	**0.07**	**F**	0.101	0.08	F	0.458	0.77	U
0.042	0.03	U	0.133	0.11	U	0.134	0.09	U
0.110	0.06	U	0.175	0.17	F	0.190	0.19	U

In order to develop a simulation model which accounts for the whole ductile-to-brittle transition of steels, The Complete Gurson Model is combined with the RKR Criterion as a post-processing routine as described in Section 3.3.1. The following list constitutes the comprehensive process of determining the essential material properties and the constitutive model parameters:

1. **Tensile testing** conducted at temperatures in the brittle, transition and ductile regions
    (a) Plot the engineering stress-strain curves
        i. Determine the elastic parameters, E and v, and the characteristic yield strength, σ_{ys}
    (b) Plot the true plastic stress-strain curves
        i. Calibrate the strain hardening exponent, n and estimate true plastic flow curves with limited data points for simple model characterisation in ABAQUS by utilising the Ramberg-Osgood equation and the experimental true plastic strain-stress curves

2. **Fracture mechanics testing** at all temperatures utilising SENB specimens
    (a) Measure the mid-point force as a function of CMOD and plot corresponding Force-CMOD curves
    (b) Measure the crack growth and plastic blunting by cracking the specimens open and utilise an optical microscope
    (c) Calculate the CTODs by utilising measured CMODs and crack growth at unloading and fracture (see Section 2.6.4)
    (d) Plot the experimental CTOD scatter of all unloaded and fractured specimens
3. **Develop ABAQUS Gurson UMAT**
    (a) Create an ABAQUS finite element model with accurate dimensions, symmetry axes, and boundary conditions
        i. Define the mesh element length, $l_c = 0.1mm$
        ii. Incorporate the material properties and parameters from the estimated true plastic flow curves into the Gurson material code
        iii. Define the initial Gurson parameters as $f_c = 0.2$ and $f_0 = 0.0014$
    (b) Calibrate the initial void volume fraction, f_0 by fitting the Gurson simulated resistance curve to the experimental resistance curve at the highest temperature in the ductile region. Remember to exclude both simulation blunting and experimental blunting during the fitting procedure
4. **Develop simple ABAQUS FE-model**
    (a) Create an identical model as in the previous stage but only incorporate E, v, and the estimated true plastic stress-strain curves as material parameters
    (b) Run simulations and verify the accuracy of the FE-model by fitting the simulated Force-CMOD curve to the experimental Force-CMOD curves at the lowest temperature in the brittle region
    (c) Set the characteristic distance, x_c equal to the diameter of two grains. If unknown, use 60 microns (0.060mm) as a reference distance
5. **Determine the temperature independent opening stress (if applicable)**
    (a) Examine the experimental Force-CMOD curve to identify the characteristic fracture toughness and use the simple ABAQUS model to find the critical time increment. Use the experimental fracture toughness at failure from the characteristic specimen at the lowest temperature to identify the critical time increment in the ABAQUS simulation
    (b) At the applicable critical time increment, create a path along the crack ligament and plot the opening stress as a function of true distance from the crack tip
    (c) Find the largest opening stress which is maintained over the entire characteristic distance and define it as the temperature independent critical opening stress, $\sigma_{c_{TID}}$

6. **Determine the temperature dependent opening stresses**
    (a) Find the critical opening stresses at the corresponding time increments for all the lowest experimental CTOD fracture values. Use the last time increment in the simulation if none of the specimens fractured at the respective temperature
    (b) Plot all the critical opening stresses as a function of temperature and find the best approximation. Microsoft Excel with its trendline approximation tool is recommended
    (c) For the applicable specimens, use the approximation and the critical opening stress available at the lowest temperature to approximate the remaining critical opening stresses, $\sigma_{c_{TD}}$ at higher temperatures
    (d) If the approximation is set as linear, use the characteristic experimental values to create the linear approximation. Combine the temperature approximation with the known opening stress and extrapolate the remaining opening stresses

All the constitutive parameters utilised in this section are displayed in **Table 4.2**. The parameters and material properties are extracted from experimental tests and simulations at -60°C, 0°C, and 21°C.

Table 4.2: All the constitutive parameters utilised in the Combined Gurson-RKR Model. $\sigma_{c_{TD}}$ and $\sigma_{c_{TID}}$ are the temperature dependent and independent critical opening stresses

T °C	E [GPa]	v	σ_{ys} [MPa]	f_0	f_c	l_c [mm]	x_c [μm]	$\sigma_{c_{TD}}$ [MPa]	$\sigma_{c_{TID}}$ [MPa]
-60	208	0.3	697	0.0012	0.2	0.1	60	2355	2355
0			676					2405	
21			667					2375	

4.2 Gurson-RKR Model 1

A Combined Gurson-RKR Model can be established by utilising the constitutive parameters in **Table 4.2**. The Gurson parameters are first estimated at 21°C to describe the ductile mechanisms, and then the RKR Criterion is fitted as a post-processing routine to predict brittle failure at -60°C. The distance-based RKR Criterion can predict brittle failure at -60°C but needs an underlying model to describe the material softening at higher temperatures. The temperature independent opening stress, $\sigma_{c_{TID}}$ in **Table 4.2** is defined at the characteristic CTOD value at -60°C as described in Section 3.3.1.

The resulting ductile-to-brittle transition curve with temperature independent critical opening stress for the Combined Gurson-RKR Model is illustrated as the thick red line in **Figure 4.2**. The DBT curve follows the Gurson-RKR curve of the characteristic specimen (#4) from -60°C until it intersects with the simulated CTOD at maximum force curve at about 9°C, and then follows the latter curve to 21°C. Thus, the material might fail by cleavage below 9°C and becomes solely ductile when exceeding 9°C. The DBT curve fits at both -60°C and 21°C which is expected as the model is fitted at both temperatures. However, the DBT curve does not correspond with the experimental scatter in the transition region. The characteristic value at 0°C should a priori be between the second lowest and the lowest fracture CTOD values. The lowest experimental fracture at $0°C$ occurs at CTOD = 0.101mm, and the second lowest fracture at CTOD = 0.175mm. Also, the lowest unloading CTOD value is equal to $0.133mm$ which in turn makes the lowest CTOD at fracture excessively conservative as the unloading happens at a CTOD higher than the lowest fracture value. Nevertheless, the characteristic CTOD at $0°C$ is equal to $0.111mm$ and thus between the two fracture CTOD values. Hence, the brittleness is highly overestimated at $0°C$ which in turn means the model also overestimates the brittleness at $21°C$ when considering the same critical opening stress. Thus, the combined model is too conservative to give an accurate representation of the ductile-to-brittle transition.

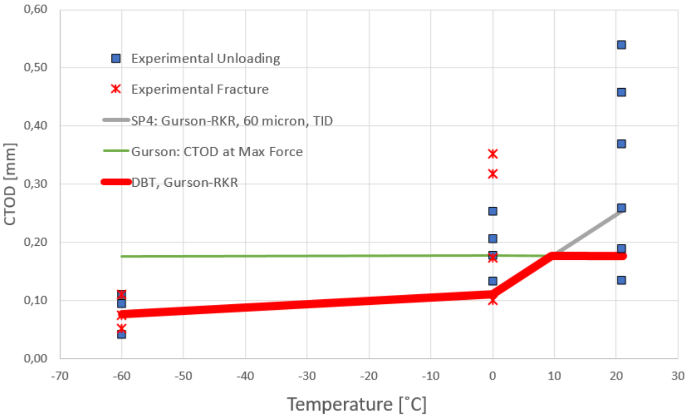

Figure 4.2: DBT with CTOD at maximum force as the competing criteria Temperature independent (TID) critical opening stress fitted at -$60°C$.

The Combined Gurson-RKR Model can describe the material behaviour at -$60°C$ which is expected as the critical opening stress is fitted at this temperature. However, the model is unable to accurately describe the proper material behaviour in the transition and ductile regions, and it is inadequate to only incorporate the true plastic flow curves as temperature dependent material parameters. The initial void volume fraction, f_0 fitted at $21°C$, and the critical opening stress fitted at -$60°C$ are both initially established as temperature independent. The model should a priori simulate more ductile crack growth at $0°C$ prior to brittle fracture, and the initial void volume fraction or the critical opening stress might be temperature dependent. Thus, a temperature dependent critical opening stress may yield a better representation of the experimental fracture toughness scatter at $0°C$ and $21°C$.

4.3 Gurson-RKR Model 2

In order to visualise the DBT regions, the experimental fracture toughness scatter needs to be representative and not based on desired CTOD values where the specimens are unloaded before reaching maximum force, or specimens which are unloaded or fail after reaching the CTOD at maximum force. Even though all the experimental specimens at $21°C$ are unloaded, it is still unknown which ones exceeded the CTOD at maximum force. The following criteria must be fulfilled in order to illustrate the representative scatter plot:

- Experimental specimens which are unloaded before reaching maximum force are redundant as they do not tell anything about how far the specimens are able to bend before fracturing, or if the specimens can survive the critical maximum force. These specimens are removed from the experimental scatter plot.

- Experimental specimens which survives the maximum force and continue bending before either fracturing or are unloaded must be adjusted. The interesting and representative values are the CTOD at maximum force as the material is certain to exhibit ductile behaviour after this point. Thus, all the experimental values which survive the maximum force are set to the CTOD value at maximum force.

None of the specimens reached the maximum force at -60$°C$ which in turn means only the three fractured specimens are representative as it is unknown if the unloaded specimens would cleave before reaching maximum force or not. At 0$°C$, four specimens passed the maximum force before they fractured or were unloaded. Two of them fractured before reaching maximum force, and two specimens were unloaded before reaching maximum force. And at 21$°C$, all the specimens were unloaded where two were unloaded before reaching maximum force, and four unloaded after reaching maximum force. Thus, seven specimens are redundant as they were unloaded before reaching maximum force, and eight specimens passed the maximum force and are set to the CTOD at maximum force.

The critical opening stress as a function of temperature must a priori be approximated from the characteristic experimental values to give a representative description of how the critical opening stress changes with temperature. After removing the redundant specimens, the characteristic value at -60$°C$ is now the lowest fracture CTOD value, and the characteristic experimental value at 0$°C$ is a priori between the lowest unloaded value and the second lowest fracture value. The lowest unloading value at 0$°C$ is for simplicity defined as the characteristic CTOD = 0.133mm without any extrapolation. The experimental approximation curve is illustrated with a stippled blue line in **Figure 4.3**, and the critical opening stresses from the characteristic points at -60$°C$ and 0$°C$ are utilised to approximate a linear relationship between the critical opening stress as a function of temperature.

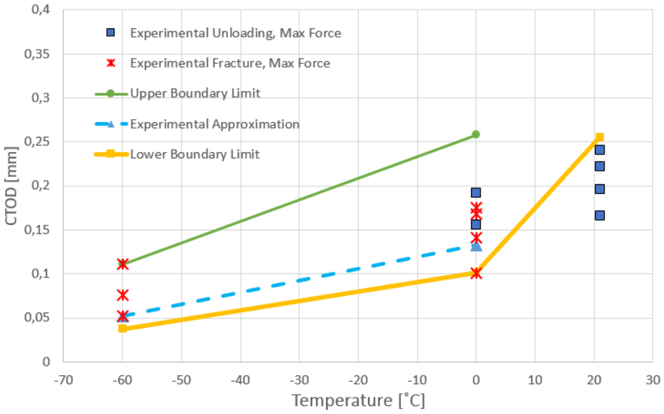

Figure 4.3: Experimental approximation, and upper and lower boundary limits. Experimental CTOD at maximum force.

The critical opening stresses for the lower and upper boundary limits can be established by utilising the linear opening stress approximation in **Figure 4.3**. The lower boundary limit is the lowest CTOD as a function of temperature the material might endure, and the upper boundary limit is the highest CTOD at maximum force the material might endure. As shown in **Figure 4.3**, the lower boundary limit is fitted to the lowest CTOD at $0^\circ C$, and the opening stress approximation is used accordingly to find the critical opening stresses at -60$^\circ C$ and $21^\circ C$. For the upper boundary limit, the opening stress approximation is fitted to the largest CTOD at -60$^\circ C$ which in turn is utilised to approximate the critical opening stresses at $0^\circ C$ and $21^\circ C$. All the critical opening stresses with corresponding CTOD values are exhibited in **Table 4.3**.

Table 4.3: Temperature dependent critical opening stresses and CTODs at failure. x_c = 60 microns

	Exp. Approximation			Lower Boundary Limit			Upper Boundary Limit		
Temperature [$^\circ C$]	-60	0	21	-60	0	21	-60	0	21
σ_c [MPa]	2290	2350	N/A	2285	2345	2364	2375	2435	2456
CTOD [mm]	0.052	0.133	N/A	0.037	0.101	0.255	0.111	0.258	N/A

As shown in **Figure 4.3**, the lower boundary limit reaches its critical opening stress at $21^\circ C$ while the upper boundary limit does not reach its critical opening stress at $21^\circ C$ and will go towards infinity. Thus, another underlying competing criterion must be utilised to describe the respective DBT regions. As the experimental scatter at $21^\circ C$ is only represented by CTOD at maximum force, the competing criterion for the upper boundary limit is the highest experimental CTOD value at $21^\circ C$. Thus, the upper criterion represents the maximum CTOD the material can reach before the specimen endures plastic deformation yielding lower mid-point force with further crack growth, and the lower competing criterion represents the minimum CTOD at maximum force the material must reach in order to exhibit ductile behaviour. The resulting upper and lower boundary limits are shown in **Figure 4.4** where the lowest and highest experimental CTOD at maximum force at $21^\circ C$ are used as the competing criteria.

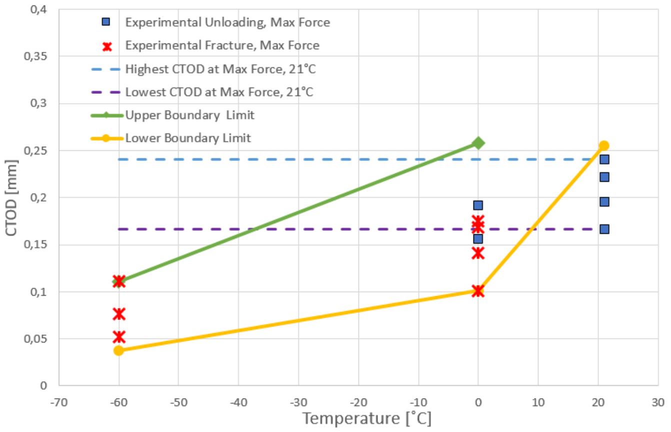

Figure 4.4: Upper and lower boundary limits and competing ductility criteria

The resulting upper boundary limit is fitted to the highest experimental CTOD at -60$^\circ C$ and follows the upper limit Gurson-RKR curve until it intersects with the upper competing criterion and remains constant to $21^\circ C$. The resulting lower boundary limit starts at a point below the lowest experimental CTOD at -60$^\circ C$ and follows the lower limit Gurson-RKR curve until it intersects with the lower competing criterion and follows the latter curve to $21^\circ C$. As shown in **Figure 4.5**, the DBT regions can be visualised by utilising the resulting upper and lower boundary limits. The illustrated curves are described with nonlinear upper and lower boundary limits in order to give a more representative ductile-to-brittle transition. The material is in the brittle region until the upper boundary limit reaches the lower competing ductility criteria and enters the transition region at about -26$^\circ C$. The material remains in the transition region until the lower boundary limit reaches the lower competing criterion and enters the ductile region at about $11^\circ C$.

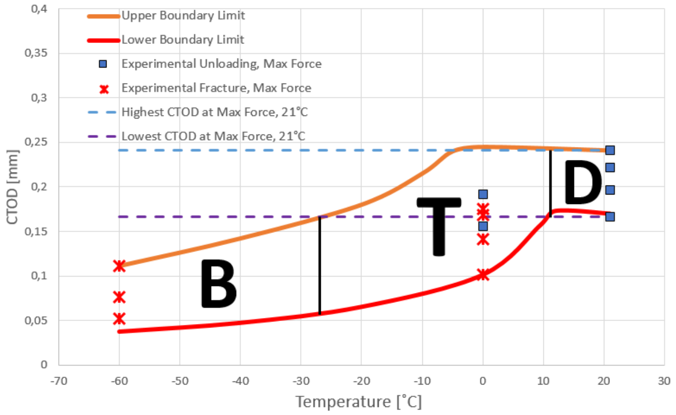

Figure 4.5: The resulting ductile-to-brittle transition regions
B = Brittle, T = Transition, D = Ductile

The Combined Gurson-RKR Model with temperature dependent critical opening stress can visualise the three DBT regions, and by only considering the experimental CTOD values at maximum force, the upper and lower boundary limits can describe the applicable material behaviour regions. The simulated upper and lower boundary limits capture the whole experimental fracture toughness scatter at all temperatures and yields a good representation of the material behaviour with shifting temperature. The linear approximation of the critical opening stress as a function of temperature is plausible but not inevitable. Thus, the model is somewhat inconclusive as the opening stress approximation needs to be tested for other materials in order to conclude the temperature approximation trend. If the opening stress temperature approximation is material independent, the resulting Combined Gurson-RKR Model can reduce the laboratory work required to describe the ductile-to-brittle transition.

4.4 Gurson-RKR Model Evaluation

The primary objective of developing the Combined Gurson-RKR Model is to reduce the experimental laboratory work required to describe the ductile-to-brittle transition of structural steels. Keeping that in mind when evaluating the models highlights several challenges. The Combined Gurson-RKR Model with temperature independent opening stress is too conservative to describe the ductile-to-brittle transition as shown in Section 4.2. Only the true plastic flow curves are initially incorporated as temperature dependent parameters while the critical opening stress, the initial void volume fraction, and the characteristic distance are fitted as temperature independent parameters.

Thus, the critical opening stress is established as temperature dependent in order to give a better representation of the experimental scatter and a less conservative model. As the stress state changes with temperature, it is plausible that the critical opening stress also changes with temperature. A linear approximation of the characteristic experimental values is utilised to create upper and lower boundary limits in order to visualise the full extent of the DBT regions. The resulting material behaviour regions can capture the full extent of the fracture toughness scatter throughout the DBT. However, the linear approximation of the critical opening stress as a function of temperature is plausible but not certain. Thus, to reduce the laboratory work needed to describe the ductile-to-brittle transition, the critical opening stress approximation must be defined as material independent. Without doing any addition simulations for other materials, the critical opening stress as a temperature dependent parameter cannot be concluded. The determination of the critical opening stress, σ_c and the characteristic distance, x_c is also quite challenging. Due to the large element size and rather low mesh resolution, the determination of the critical opening stress is rather difficult. Also, the characteristic distance, x_c is fitted as constant and independent of both microstructure and temperature, and remains questionable as the microstructure might change with temperature and type of material.

All the uncertain parameters and challenges with the Combined Gurson-RKR Model indicate that it might not be adequate to describe the ductile-to-brittle transition. The model can visualise the material behaviour regions accurately when the material parameters are fitted in both the ductile and brittle regions. Whether the model can be used to reduce the laboratory work needed to describe the ductile-to-brittle transition for other materials is still unknown as several material parameters remain uncertain and questionable. If the temperature approximation of the critical opening stress is material independent, it is still doubtful if the model will reduce the laboratory costs as the current Gurson-RKR Model needs fracture mechanics data at an intermediate temperature in order to establish the temperature approximation and the resulting upper and lower boundary limits.

4.4.1 Conclusion

The simulation scheme is developed in order to describe the ductile-to-brittle transition and to visualise the DBT regions. The Complete Gurson Model is utilised to describe the material softening, and the Gurson parameters are estimated at $21°C$ where the material is completely ductile. The distance-based RKR Criterion is utilised as a post-processing criterion in combination with The Complete Gurson Model to predict cleavage fracture initiation, and the RKR parameters are fitted at -$60°C$ where the material is entirely brittle. $0°C$ is used as the intermediate temperature constituting transitional behaviour with concurrent ductile and brittle mechanisms. The Combined Gurson-RKR Model can describe the shifting material behaviour and the fracture toughness temperature dependence.

The original Complete Gurson-RKR Model with a temperature independent critical opening stress as the fracture criterion is not sufficient to describe the ductile-to-brittle transition. The model is too conservative and highly overestimates the steel's brittleness at $0°C$ and $21°C$. The constraint effects at higher temperatures are too elevated with extended crack growth which in turn underestimates the fracture toughness in the transition and ductile regions. The underlying model is improved by converting the critical opening stress to a temperature dependent parameter in order to represent the whole experimental scatter and make it less conservative.

The improved model with temperature dependent critical opening stress can visualise the brittle, transition and ductile regions where the highest and lowest experimental CTOD values at maximum force at $21°C$ are respectively utilised as the competing criteria for the upper and lower boundary limits. The lower boundary limit reaches the critical opening stress at $21°C$ which in turn means the underlying model still overestimates the steel's brittleness in the ductile region. However, the resulting upper and lower boundary limits can visualise the DBT regions and clearly illustrate a temperature dependent fracture toughness. The material is entirely brittle up until -$26°C$ where it enters the transition region and exhibits both ductile and brittle behaviour until the material reaches $11°C$ where the material enters the completely ductile region.

The Combined Gurson-RKR Model gives a good representation of the DBT regions but several material parameters remain questionable, and the objective of the simulation scheme is not unconditionally reached. The characteristic distance is fitted without directly linking it to the microstructure, and the temperature dependent critical opening stress approximation cannot be concluded as material independent without further material testing. Thus, the current simulation scheme needs to be fitted and adjusted accordingly when describing the ductile-to-brittle transition of other materials, and The Combined Gurson-RKR Model must be further improved in order to reduce the laboratory work needed to describe the ductile-to-brittle transition.

The critical opening stress temperature dependence needs to be further investigated, and as the initial yield strength decreases with increasing temperature and the crack tip constraint effects increases with crack growth, the accuracy of the critical opening stress temperature dependence remains uncertain. Another brittle fracture model can substitute the RKR Criterion to predict unstable crack propagation and the following work needed to drive the microcrack far enough to yield cleavage fracture. A cohesive zone model as described in Section 3.1.2 can be used to simulate these features which in turn can eliminate the current challenges of determining the critical opening stresses. Another approach is to describe the fracture toughness by considering statistical features in the process of microcrack formation where a typical Weibull-based Beremin model as described in Section 3.1.3 can be used to compute the probability of brittle fracture. Thus, the Weibull-based Beremin model will give a more representative characterisation of the material behaviour regions based on statistical confidence intervals with material parameters independent of fracture geometry and constraint levels.

Chapter 5

Material and Model Implementation

This chapter describes the material characterisation and the model implementation methods in order to provide a profound understanding of how the models work in combination with the simulation tools. The scope is to find the most adaptable and versatile implementation methods in order to make the final simulation as time efficient as possible.

5.1 Material

A weld simulated CGHAZ 420 MPa steel with the weld cooling time, $\Delta t_{8/5} = 5s$ is further utilised and examined in the subsequent sections. SINTEF initially conducted fracture mechanics and uniaxial tensile tests at five temperatures; -90°C, -60°C, -30°C, 0°C, and room temperature (21°C). The yield strengths and the ultimate tensile strengths are exhibited in **Table 5.2**, and the chemical composition is described in **Table 5.1**. The Young's modulus equals 208 GPa, and the Poisson's ratio equals 0.3. This weld simulated steel is the only available material in the SINTEF database with adequate fracture mechanics and tensile tests in the ductile region which is crucial when calibrating the Gurson parameters.

Table 5.1: Chemical composition [%wt]

C	Si	Mn	Cu	Ni	CE
0.09	0.19	1.54	0.28	0.72	0.42

Table 5.2: Yield strength and ultimate tensile strength

Temperature [°C]	Yield strength [MPa]	UTS [MPa]
-90	733	1001
-60	697	961
-30	680	931
0	676	900
21	667	889

5.1.1 Flow Curves

Simple uniaxial tensile tests are conducted in order to construct stress-strain curves and to characterise specific material parameters such as E, σ_{ys}, σ_{UTS} and v. By utilising true stress-strain curves as shown in **Figure 5.2** instead of load-elongation or engineering stress-strain as shown in **Figure 5.1**, the material characteristics become independent of test specimen geometry and shifting dimensions during testing.

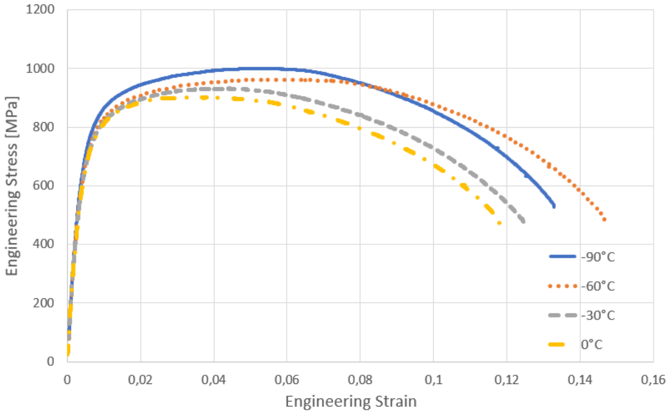

Figure 5.1: Engineering stress-strain curves from the uniaxial tensile tests

The experimental true plastic flow curves must first be interpreted and abated into manageable small sets of material input data in order to get representative input data for the constitutive ABAQUS simulation models. The true stress and true strain are initially calculated from the engineering stress and strain as

$$\sigma = s(1+e), \qquad \epsilon = ln(1+e) \quad , \ \sigma < \sigma_{UTS} \tag{5.1}$$

where s is the engineering stress, and e is the engineering strain. The resulting true stress-strain are exhibited in **Figure 5.2**, and the true stress and true strain are calculated up until necking initiation at $\sigma = \sigma_{UTS}$ where Equation 5.1 becomes invalid as the specimen starts deforming locally which in turn makes dimension updating nearly impossible with simple material characterisation equations. However, more advanced simulation models such as The Complete Gurson Model in Section 3.2.1 can be utilised to characterise the material behaviour beyond necking initiation.

The uniaxial stress-strain behaviour is characterised with a void-free $(f = 0)$ material matrix and background material, and the resulting true stress-strain curves follow the Ramberg-Osgood relationship expressed as

$$\epsilon = \begin{cases} \sigma/E & , \quad \sigma < \sigma_0 \\ C(\sigma/E)^n & , \quad \sigma \geq \sigma_0 \end{cases} \tag{5.2}$$

where ϵ is the true strain, σ_0 is the initial tensile yield strength, C is a material constant, σ is the current true stress, E is the Young's Modulus, and n denotes the strain hardening exponent.

The latter Ramberg-Osgood approximation in Equation 5.2 can be further simplified if the yield strength is known. The simplified Ramberg-Osgood equation can thus be deduced to

$$\epsilon = \begin{cases} \sigma/E & , \quad \sigma < \sigma_0 \\ \alpha(\sigma/E)(\sigma/\sigma_0)^{n-1} & , \quad \sigma \geq \sigma_0 \end{cases} \tag{5.3}$$

with α defined as $\alpha = C(\sigma_0/E)^{n-1}$ which in turn substitutes the initial C in Equation 5.2 where $\alpha(\sigma_0/E)$ is defined as the yield offset (usually 0.002). The first part of both Equation 5.2 and 5.3 $(\sigma < \sigma_0)$ represents the linear elastic material behaviour region solely based on the Young's modulus defined as the slope of the stress-strain curve in the elastic region. [108] The second part $(\sigma \geq \sigma_0)$ represents the plastic region and the true plastic flow curves where the material exhibits plastic deformation and material softening.

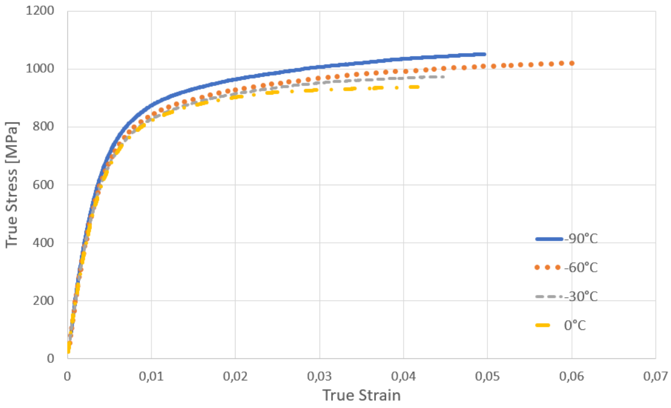

Figure 5.2: True stress-strain curves from the uniaxial tensile tests

An optimisation scheme in Microsoft Excel can be utilised to determine the constitutive Ramberg-Osgood constants in Equation 5.2. Do natural logarithm of the true plastic flow curves and run a mean least square linear regression of the logarithmic plot in order to find the strain hardening exponent defined as the slope of the logarithmic regression function. The resulting regression is virtually found by doing simple linear trend regression of the logarithmic true plastic flow curves, and additional statistics such as material constant confidence intervals can be estimated by using the regression function in the Microsoft Excel add-on 'Data Analysis Tools'. However, a more efficient approach is suggested as the yield strength is effortlessly identified from the uniaxial tensile tests. The material constant α is readily calculated from the yield offset, $0.002 = \alpha(\sigma_0/E)$ by utilising Equation 5.3, and the strain hardening exponent, n is calibrated by fitting the estimated and experimental true plastic flow curves. The resulting material input is illustrated in **Figure 5.3** where the material input is solely based on the optimised Ramberg-Osgood equation (5.3) fitted to experimental tensile test output.

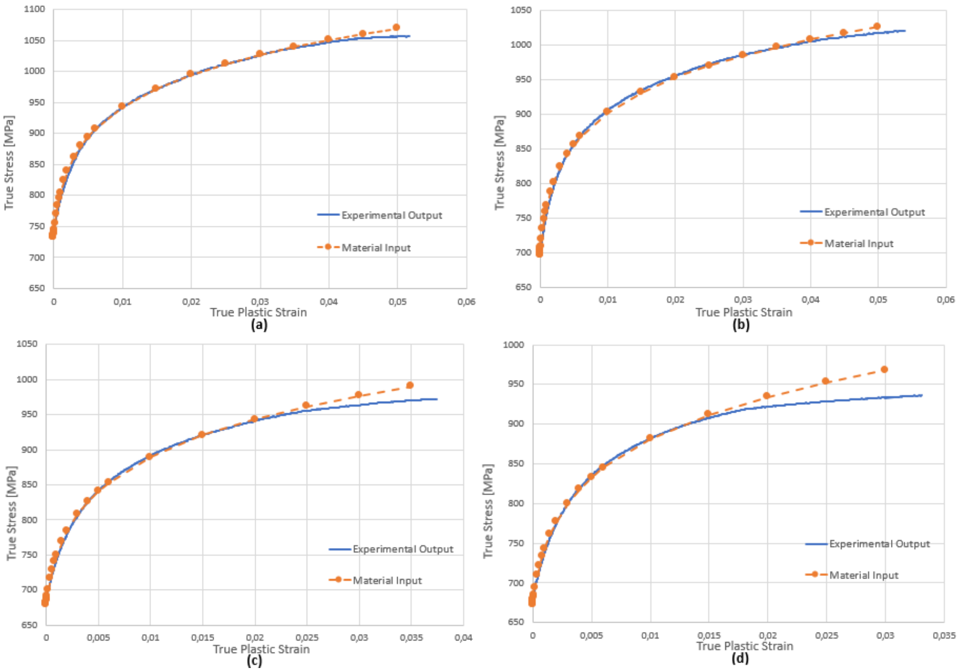

Figure 5.3: Experimental and Ramberg-Osgood estimated true plastic flow curves (a) -90°C, (b) -60°C, (c) -30°C, (d) 0°C

The Ramberg-Osgood estimated material input data points exhibited in **Figure 5.3** are utilised to characterise the material behaviour after yielding. As discussed earlier in this section, the true stress and strain are only valid up until the ultimate tensile strength, σ_{UTS}, which means the Ramberg-Osgood equation is only able to characterise the material up until necking initiation. The material input in **Figure 5.3 (a) and (b)** fits the experimental output, and are thus considered as accurate material input for the ABAQUS FE-models described in Section 5.2. However, the material input in **Figure 5.3 (c) and (d)** somewhat deviate from the experimental output at large true plastic strain levels. The large deviations with increasing strain levels are due to the local material deformation after necking initiation. Nevertheless, following the constitutive ultimate tensile strengths in **Table 5.2** and the material fitting in **Figure 5.3**, all the material input flow curves fit the experimental output up until the corresponding ultimate tensile strength. Hence, the material input from the Ramberg-Osgood optimisation scheme, regardless of temperature, is accurate up until necking initiation and can thus be applied as representative material input.

5.2 Fracture Mechanics Testing and Finite Element Model

All the applicable fracture mechanics tests are single edge notched bend (SENB) specimens as shown in **Figure 5.4** and are made from rolled plates where the rolling direction might influence the results. After the specimen is cut with the right dimensions, a notch is machined into the specimen edge creating a fatigue pre-crack with a small crack radius and a small plastic zone. The specimen is equipped with loading cells and clips to respectively measure the mid-point force and CMOD in order to plot corresponding Force-CMOD curves. The crack extension and plastic blunting are measured by cracking the specimen open and examining the fracture surface with an optical microscope. Thus, the resistance curves can be plotted, and the CTOD and K_I values can be calculated.

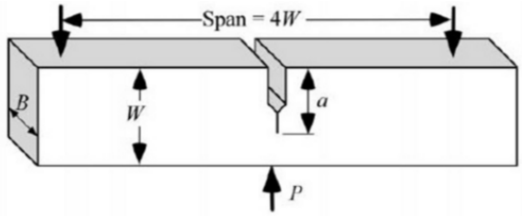

Figure 5.4: SENB specimen with constitutive dimensions, fatigue pre-crack, and loads [4]

As shown in **Figure 5.4**, only half of the specimen needs to be simulated in ABAQUS due to symmetry in the fracture mechanics test specimens. The finite element models are made in 2D with unit thickness, and the applicable finite element mesh model, boundary conditions, and dimensions are exhibited in **Table 5.3** and **Figure 5.5**.

Table 5.3: Dimensions CAE-models

Model	W [mm]	a [mm]	a/W	S [mm]	Length [mm]	Crack-tip mesh size [mm^2]
SENB05$_A$	10	5	0.5	20	40	0.05x0.10
SENB05$_B$	10	5	0.5	20	40	0.05x0.05
SENB02	10	2	0.2	20	40	0.05x0.10

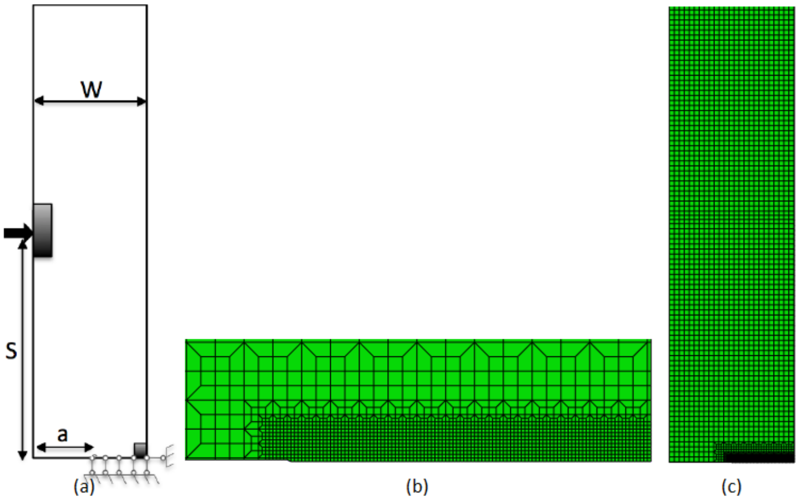

Figure 5.5: (a) Boundary conditions, material selection and dimensions for the SENB models, (b) Detailed mesh in the crack region, (c) Full-scale finite element model used in the analysis

Simple 4-noded 2D plane strain elements (CPE4) are used, and nonlinear effects (NLGEOM in ABAQUS) are accounted for in the simulations. The full-scale finite element mesh model is shown in **Figure 5.5 (c)**, and the detailed crack tip mesh is exhibited in **Figure 5.5 (b)** where a small element size is imperative to get accurate crack simulations. Two different mesh sizes are initially considered, one with mesh element length $0.05mm$ and one with mesh element length $0.10mm$. **Figure 5.5 (a)** illustrates the boundary conditions where the specimen is constrained at the bottom right side making it unable to follow the displacement and forces the specimen to bend. The FE-model is constrained at the bottom along the crack ligament due to symmetry, and will thus simulate the desired bending. The arrow indicates the modelled displacement and the black sections illustrate the elastic material used to mitigate the stress concentration at the respective nodes.

5.3 Implementation of the Weibull-based Beremin Model

The Beremin model is based on the weakest-link principles and the Weibull approach, and is closely related to the stress field ahead of the crack and the fracture process zone as described in Section 3.1.3. As the model predicts the probability of brittle fracture, the fitting procedure is initially conducted in the brittle region where the material exhibits solely brittle characteristics with a flaw distribution following the Weibull distribution and weakest-link principles in Equation 3.2 and 3.4. However, it becomes crucial to use an appropriate Weibull calibration method as the reliability of the Weibull parameters and the Beremin model are highly dependent on the number of test specimens. The reliability of the Weibull parameters might also be biased as there exist several parameter calibration methods yielding different parameter estimates. Thus, a bias-corrected maximum likelihood estimation method could be used for brittle materials in case of biased Weibull parameter estimates. [141]

All the ABAQUS CAE models are developed in 2D with representative boundary conditions and displacement according to the experimental fracture mechanics tests described and illustrated in Section 5.2. Only the Ramberg-Osgood estimated true plastic flow curves from the experimental tensile tests following Equation 5.3 are used as material parameters in the constitutive ABAQUS models during the initial calibration procedure. The critical experimental fracture mechanics data are then measured for each fracture specimen in the brittle region where the critical CTOD values related to the displacement and time increments are examined. The resulting ABAQUS database file (.odb) are then implemented into an in-house stand-alone finite element post-processor program called LINKpfat as described by Wormsen, Fjeldstad and Härkegård in multiple papers. [150] [44] LINKpfat calculates the Weibull stress from Equation 3.8 by considering the maximum principal stresses in all elements, and the Weibull stress can then be described as a function of either time increments or corresponding fracture toughness. See Appendix B.2 for a more comprehensive description of LINKpfat and its Weibull stress calculation.

All the time increments in the fracture mechanics simulation are identified for each critical fracture toughness from the experimental results. Further, the Weibull stresses and their corresponding time increments are identified in LINKpfat and sorted in ascending order. The rank probability, P_{rank} described in Section 3.1.3 is then calculated accordingly for each fracture specimen and plotted as a function of Weibull stress. Lastly, the Weibull modulus is calibrated by doing an iterative fitting procedure of rank probabilities and critical Weibull stresses following the Weibull parameter study in Section 5.3.1 where the Weibull scale parameter, σ_u in Equation 3.7 is defined as the Weibull stress corresponding to 63.2% probability of failure and is indirectly determined after the Weibull modulus calibration is concluded.

5.3.1 Weibull Parameter Calibration

The Weibull modulus, m and the Weibull scale parameter, σ_u can be estimated by several different calibration procedures yielding biased parameter estimates. [141] The Weibull parameters should a priori be geometry and constraint independent as they represent a fixed flaw distribution only depending on material specific parameters as discussed in Section 2.8.2 and 3.1.3. The constitutive calibration procedure is a simplified approach based on an iterative process which applies median rank probabilities of experimental results and their corresponding critical Weibull stresses. Thus, the Weibull parameters are calibrated by considering only one constraint level at one temperature which in turn makes it fast and accurate for the recognised constraint level. The calibration procedure is based on the mean least square method of rank probabilities and Weibull stresses, and is successfully implemented by Xia and Cheng [151], and Gao et al. [46], among others.

The mean least square method is based on $f(x) = ax + b$ as the resulting linear regression function by determining the minimum of $R^2(a,b) = \sum_{i=1}^{n}[y_i - f(x_i)]^2$ for n test specimens with characteristic value y_i. The probability of brittle failure in Equation 3.7 is first rearranged, and then natural logarithms are done twice which in turn yields:

$$ln\left[ln\left(\frac{1}{1-P_F}\right)\right] = m \cdot ln(\sigma_w) - m \cdot ln(\sigma_u) \tag{5.4}$$

Equation 5.4 can then be described as the linear function, $y = m \cdot ln(\sigma_w) + c$ where m is the slope of the curve, $ln(\sigma_w)$ is defined as x, and $m \cdot ln(\sigma_u)$ is defined as c in the corresponding regression function $f(x) = m \cdot x + c$. The rank probability, P_F is obtained by ranking the critical Weibull stresses in ascending order by utilising the median rank probability corresponding to a 50% confidence level defined as

$$P_F = P_{rank} = \frac{i - 0.3}{n + 0.4} \quad , i \in [1, n] \tag{5.5}$$

where i is the rank number for n test samples. Rank number 1 (one) corresponds to the smallest Weibull stress, and rank number n corresponds to the largest Weibull stress. Both Wallin [141] and Fothergill [45] proved the rank probability in Equation 5.5 to be the best Weibull distribution approximation regardless of calibration methods like the maximum likelihood method and the mean least square method. Nevertheless, rank probabilities such as $P_{rank} = (i - 0.5)/n$ and $P_{rank} = i/(n + 1)$ have been successfully implemented by Gao et al. [46], and Xia and Cheng [151], respectively. The Weibull modulus is initially assumed to be an arbitrary value, m_k before computing the critical Weibull stresses by post-processing the observed experimental cleavage fracture points. Further, the rank probability as a function of Weibull stress is plotted according to Equation 5.4 and 5.5, and a mean least square regression is run which in turn results in a new Weibull modulus, m_{k+1}. If $m_k \neq m_{k+1}$, the post-processing is rerun with the new m_{k+1} value, and this procedure is repeated until the new value m_{k+1} converges to the previously simulated m_k.

The constitutive mean least square calibration steps:

1. Assume an arbitrary Weibull modulus, m_k
2. Compute the Weibull stresses for the corresponding experimental cleavage fracture points by doing an FE post-processing routine in LINKpfat
3. Rank the Weibull stresses in ascending order and plot rank probability vs σ_w following Equation 5.5 and 5.4.
4. Use P_F as the rank probability from Step 3 and σ_w from Step 2 to run the mean least square linear regression of $ln(ln[1/(1-P_F)])$ vs $ln(\sigma_w)$.
5. The linear regression in Step 4 results in a new Weibull modulus, m_{k+1} defined as the slope of the curve. Check if $m_k \approx m_{k+1}$ is fulfilled. If not, determine m_{k+1} as the new m_k and repeat Step 2-5 until $m_k \approx m_{k+1}$.

A more user-friendly and representative method is readily available to substitute the mean least square method. Thus, the maximum likelihood estimation method can be used to calibrate the constitutive Weibull parameters which in turn does not rely on mean rank probabilities and is solely based on the experimental fracture points. As illustrated in **Figure 5.6**, a Weibull modulus is first initialised before the generated Weibull stress as a function of fracture toughness is plotted. The experimental fracture points are first identified in the FEA before the critical Weibull stresses are calculated at the corresponding critical time increments in LINKpfat. Integrated functions in Matlab (see Appendix B.1) are then used to estimate the Weibull parameters and plot the Weibull cumulative probability distribution function. The newly estimated Weibull modulus, $\hat{m}$ is then reused in another iteration until the estimated Weibull modulus remains somewhat constant.

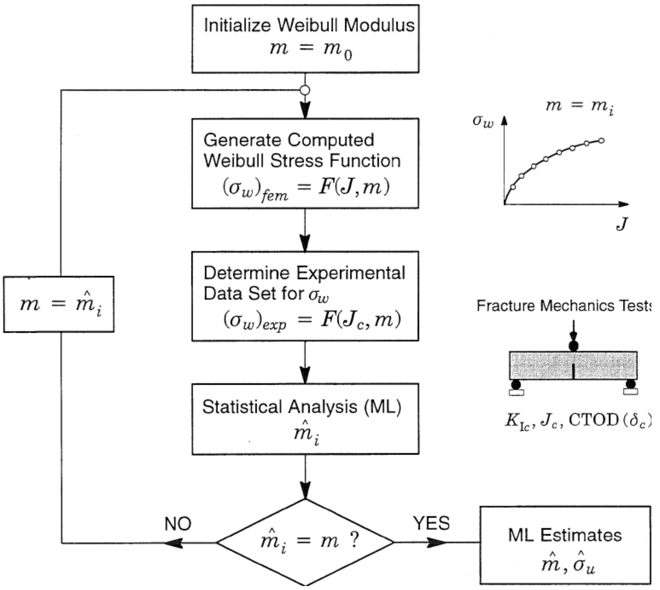

Figure 5.6: Maximum likelihood estimation algorithm for Weibull parameter calibration [124]

The mean least square (LSQ) method and the maximum likelihood (ML) method are based on one single constraint level and are thus limited to this constraint level without any extent of relation to other fracture geometries. Nevertheless, it is shown that the calibrated Weibull modulus for lower constraint levels is relatively identical with the calibrated Weibull modulus for high constraint specimens. Nonetheless, the estimation process becomes difficult with limited experimental fracture mechanics data, and a small fracture dataset might thus lead to relatively large Weibull modulus confidence intervals which ultimately converge the Weibull modulus exponentially. [124]

However, an alternative approach can be utilised to calibrate the Weibull parameter estimates if the fracture dataset is too small to calibrate unbiased Weibull parameter estimates from the LSQ and ML methods. By conducting a toughness scaling procedure of one fracture geometry with a high constraint level (configuration A) and one fracture geometry with a low constraint level (configuration B), the Weibull modulus can be calibrated by comparing the experimental fracture toughness and the simulated Weibull stresses. As shown in **Figure 5.7 (a)**, the initial Weibull parameter estimates for the high constraint specimen are used to describe the probability of failure as a function of Weibull stress which in turn constructs confidence intervals of the preliminary Weibull estimates. These parameters estimates are thus used to check if the same probability of failure prevails in the low constraint specimen in **Figure 5.7 (c)** by comparing the predicted fracture toughness values with the simulated probability of failure in the high constraint specimen. Hence, the Weibull modulus is properly calibrated when both configurations yield the same probability of failure at the same critical Weibull stresses as shown in **Figure 5.7 (b)**. [122]

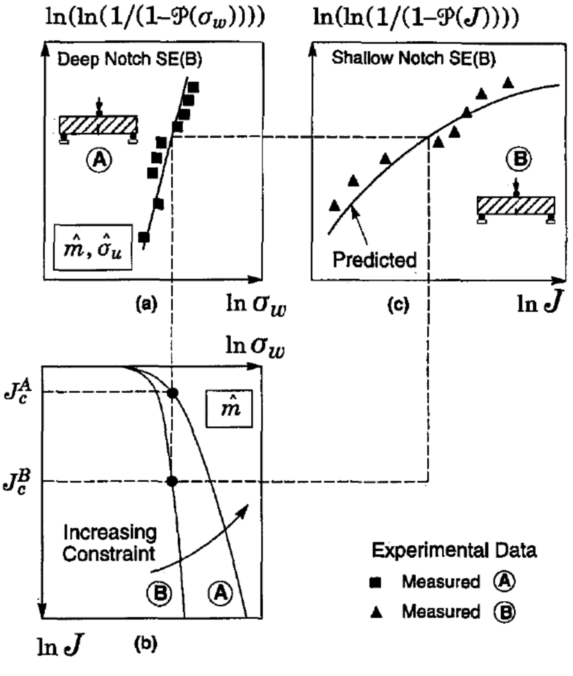

Figure 5.7: Toughness scaling procedure employed with two different crack configurations J-integral as the measured fracture toughness. [122]

The toughness scaling should a priori incorporate the near crack-tip stress field changes due to ductile tearing, constraint loss, volume stress effects, and its micromechanical features of cleavage fracture. As shown in **Figure 5.7 (b)**, the toughness scaling procedure ultimately attain equal Weibull stresses to trigger cleavage fracture even though the fracture toughness and constraint levels are considerably different. Thus, one configuration might be used to predict the fracture toughness distributions of other fracture geometries at a given temperature or material behaviour region.

5.3.2 Numerical Implementation

According to Ruggeri and Dodds [122], the cumulative probability of failure as a function of Weibull stress must be similar regardless of fracture test specimen geometry and constraint level. Thus, all the test specimens must yield approximately the same Weibull cumulative probability of failure vs Weibull stress relationship in order to apply the toughness scaling concept correctly. As the Weibull modulus is fitted for one or two of the fracture geometries according to the procedure in Section 5.3.1, the same Weibull modulus should a priori yield similar Weibull cumulative probability of failure vs Weibull stress relationships for other fracture geometries. If the toughness scaling is fulfilled, the Beremin model with its constitutive Weibull parameters is thus capable of constraint-correcting the fracture geometries. However, the toughness scaling is only valid for the respective temperature and may not be representative for other temperatures yielding different material characteristics. Thus, the Beremin model can be validified for all the test temperatures in the ductile-to-brittle transition by conducting toughness scaling of different constraint levels at the respective temperatures.

A third Weibull parameter can a priori be introduced to straighten out the P_F vs σ_w curve if it happens to illustrate a concave or convex trend. However, if the curve still does not straighten out, the current two or three-parameter Weibull distribution could either be characterised as incapable of representing the fracture mechanics data or the Weibull distribution could be represented with multiple populations of fracture data with so-called Mixed Weibull Analysis. [68] [66] The mixed analysis may be required for bi-modal grain size distributed materials with two or more independent populations with different fracture mechanisms as discussed in Section 2.2.3. The mean least square regression and the maximum likelihood estimation can be applied by utilising the Statistics and Machine Learning Toolbox in Matlab [85] which in turn constructs Weibull parameter confidence intervals and Weibull cumulative distribution functions. However, the maximum likelihood estimation method is often recommended for cases with small fracture datasets instead of the mean least square method due to the readily available Matlab functions for ML estimation (MLE). The MLE does not require any rank probability estimation nor plotting positions and can exclusively consider the critical Weibull stresses. Another comprehensive program for Weibull statistics is Weibull++ developed by ReliaSoft [109] which is supported by the ROSS Gemini Centre at NTNU/SINTEF. More about the constitutive Matlab functions to estimate the Weibull parameters in Appendix B.1.

The resulting confidence intervals following the semi-analytic expression in Equation 3.11 can be established after the Weibull parameters, m and σ_u are determined or calibrated at one or multiple temperatures. The entirely analytic approach is to use either the two or three parametric Weibull distribution following the cumulative probability of brittle failure in Equation 3.7 and 3.10, respectively. The probabilistic cleavage fracture model will thus be able to describe the fracture toughness with corresponding critical Weibull stresses at all the test temperatures and plot confidence intervals accordingly.

5.4 Implementation of The Complete Gurson Model

The Complete Gurson Model consists of equations coupling plasticity and ductile damage where the damage is considered as an internal state-dependent variable within the continuum mechanics model. It is coupled to the material strain-stress field and their constitutive true plastic flow curves which in turn is derived from a local approach to fracture constituting the ductile rupture stages in Section 2.4 in order to describe the damaged process zone. The experimental true plastic flow curves are initially used as the material input implemented in the Gurson FE-model material. Thus, true stresses for desired true strains can be obtained and utilised to find the strain hardening exponent, n from the necking phase. The deformation and failure can be predicted with high accuracy when using finite element tools which in turn can demonstrate accurate material damage models. However, the models are highly mesh-dependent as they are susceptible to damage localisation and strain. [19]

The input parameters in The Complete Gurson model are the true plastic flow curves in **Figure 5.3** and the Gurson parameters, f_0 and f_c. Several constitutive data files are generated by running the first job from the ABAQUS CAE model; the output file (.dat), the input file (.inp), and the ABAQUS database file (.odb). The material characterisation section in the input file is manually updated with the Gurson parameters, f_0 and f_c, and the Ramberg-Osgood estimated data points from the temperature dependent true plastic flow curves in Section 5.1.1. The rest of the simulation is conducted directly in the input file by implementing the Gurson model equations and characteristics through a user subroutine. The constitutive subroutine is defined by a user-defined material (UMAT) which is not part of the original ABAQUS library and requires manually implemented material input data and state-dependent variables (Appendix C.3). The simulation is then run by activating a short command (.cmd, Appendix C.1) which concurrently runs the Gurson UMAT (Appendix C.2) and the input file in the ABAQUS solver. It may be necessary to manually renumber the nodes along the crack ligament with consecutive numbers as the user subroutine is element and node dependent. If undone, the only output will be from the first element at the crack tip which in turn is unable to describe the applicable fracture toughness as a function of ductile crack growth.

A new output file is created after the simulation is conducted, and another commando script is utilised (Appendix C.4) to initiate a python script made by SINTEF in order to extract the respective CTOD and crack growth from the output file (.dat). The extracted data is then utilised to plot the CTOD-Δa resistance curves at all temperatures. Thus, the CTOD can be plotted as a function of Δa at different temperatures in order to illustrate the accuracy of the ductile mechanisms from The Complete Gurson Model by comparing the simulated and experimental resistance curves. However, the Gurson parameters must be refitted by trial and error if the simulated resistance curve at the highest temperature in the ductile region does not fit the experimental results.

5.4.1 Gurson Parameters

The Gurson model requires state-dependent variables and material input data consisting of the Gurson parameters and the true plastic flow curves. Since the Thomason's plastic limit load model in Section 3.2.1 only partly solves the void coalescence criterion, the critical void volume fraction, f_c and the initial void volume fraction, f_0 must be fitted accordingly. Thus, f_c becomes a by-product of the coalescence prediction while f_0 must be determined by comparing the simulated and experimental resistance curves. The Gurson parameters are fitted in the ductile region where it will solely describe ductile mechanisms and yield accurate predictions compared to the experimental results. Thus, the simulated resistance curve is fitted to the experimental resistance curve in the ductile region by testing multiple initial void volume fractions. However, the material might cleave after some extent of ductile crack growth in the transition region which in turn means the Gurson parameters may not be able to describe accurate resistance curves in this region. As the Gurson model is unable to predict cleavage fracture initiation, the model will overestimate the loss of load-bearing capacity and force void-induced ductile crack growth where the crack extension will continue regardless of temperature and brittle characteristics.

The Gurson model will not capture the appropriate material behaviour in the brittle region as the material exhibit solely brittle characteristics. The material will yield brittle fracture even before any plastic flow is initiated, and the void-induced ductile crack growth will continue indefinitely as the Gurson model is unable to identify the cleavage fracture initiation.

5.4.2 Mesh Sensitivity

The void volume fraction controls the material softening and is calculated at the element node integration points in the finite element model. The length of the crack growth step determines the material crack extension due to the discontinuous process of void coalescence. It might be challenging to incorporate the optimal length scale necessary to account for the material softening as the Gurson model is dependent on the individual crack integration points along the elements. Tvergaard and Needleman [94] incorporated the mesh length scale, l_c as a material parameter directly into the analysis in order to solve the softening issue.

The mesh size sensitivity is further investigated in Section 6.3.1 where the mesh element length along the crack ligament is $0.10mm$ for SENB05$_A$ and $0.05mm$ for SENB05$_B$ (see **Table 5.3**). The damage zone and mesh element size will both change accordingly as the void volume fraction is localised in between the integration points due to localisation where each element contains a void which is treated as a nucleation point. As described in **Table 5.3**, the damage zone is set to $0.05mm$ for both models, and the resulting resistance curve slope shifts accordingly when the mesh element length is changed.

Chapter 6

Results and Discussion

This chapter comprises the results of the experimental fracture mechanics tests along with a brief discussion of the reliability of the datasets. Further, the experimental data is utilised to calibrate the material characterisation models to calculate brittle failure probabilities and simulate ductile mechanisms. First, the Beremin model with its constitutive Weibull parameters are estimated with a material solely based on the true plastic flow curves. The Gurson model parameters are after that calibrated and a user-defined material (UMAT) is developed by utilising the constitutive Gurson parameters in combination with the true plastic flow curves in order to simulate void-induced ductile mechanisms. Lastly, the Beremin model and the Gurson UMAT are combined to give a better representation of the material behaviour throughout the ductile-to-brittle transition. The Gurson UMAT describes the ductile mechanisms, and the Beremin model is used as a post-processing routine to calculate the probability of brittle failure.

6.1 Fracture Mechanics Testing

The fracture mechanics tests used as a basis for the simulation scheme are from two separate projects conducted by SINTEF Industry; one from the Arctic Materials I project [129] and one recent project which constituted additional tests in the ductile region. The weld simulated CGHAZ steel described in Section 5.1 is used for all the single edge notched bend specimens at temperatures from -90$°C$ to 21$°C$. The cross-section for all the specimens is 10x10mm^2, electrical discharge machining (EDM) is used to obtain desired initial crack depths, and liquid nitrogen is used to constrain the desired low test temperatures.

During bending, the CMOD and the mid-point load are concurrently monitored which in turn results in corresponding Force-CMOD curves. After the test series are finalised, the specimens are cracked open, and an optical microscope is utilised to examine the crack propagation. The crack extension is then measured using a nine-point measuring procedure based on the average crack growth by comparing the initial crack from the EDM and the crack growth after the test is conducted. Equation 2.22 is then used to calculate corresponding CTOD fracture toughness values which in turn can be used to plot representative resistance curves (see Section 2.10) at any given temperature.

The Arctic Material I project series is based on testing until exhibiting sudden brittle fracture, while the recent SENB05 test series is based on unloading at desired CMOD values. Several specimens exhibit pop-ins and brittle characteristics before unloading when reviewing the experimental Force-CMOD curves. As the crack growth is measured after the fracture mechanics test is finished, several specimens exhibit unobtainable crack growth values which distinctly affects the resulting R-curves and makes them less comprehensive. As exhibited in **Figure 6.1**, the measured crack growth at the CMODs indicated with red squares might deviate from the applicable CMODs at the brittle increments illustrated with arrows. Since both CMOD and crack growth are utilised when calculating the corresponding CTOD values (see Equation 2.22), the inconsistently measured crack growth will severely bias the resulting fracture toughness values.

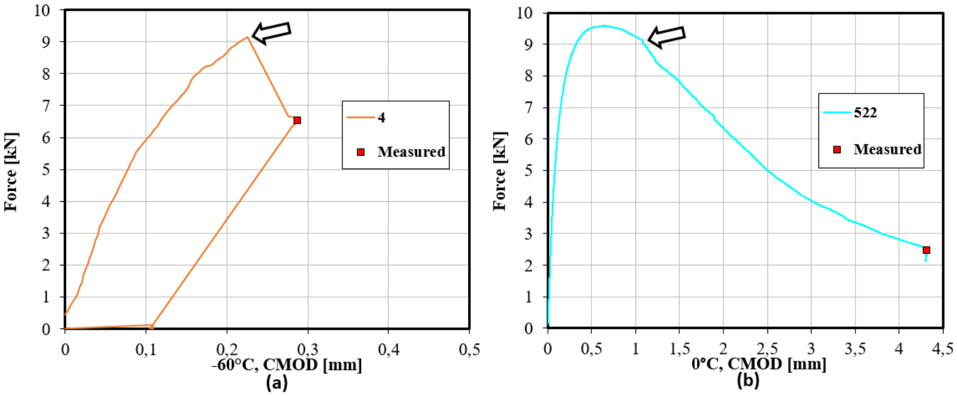

Figure 6.1: Experimental SENB05: Red squares indicating measured crack growth and arrows indicating critical brittle characteristics points. (a) Specimen 4 at -60°C, (b) Specimen 522 at 0°C

Nevertheless, at lower temperatures such as in **Figure 6.1 (a)**, the crack growth is negligible as the material is in the solely brittle region and the resulting CTOD values will not be affected. The same conclusion prevails in the solely ductile region as all the specimens are unloaded without brittle characteristics, and the resulting CTOD values will not be affected as the measured crack growth remains accurate. However, at temperatures in the transition region such as in **Figure 6.1 (b)**, the material is expected to exhibit some ductile crack growth prior to yield brittle characteristics. Hence, the biased crack growth and fracture toughness in the transition region are taken into consideration when reviewing the Force-CMOD and resistance curves. All the specimens which randomly exhibit brittle characteristics prior to unloading cannot be concluded with accurate crack growth and thus neither representative CTOD values.

As exhibited in **Figure 6.2**, representative experimental resistance curves can be described after excluding all the specimens which had inconclusive crack growth values. Only the SENB05 test series comprises crack growth values in all the ductile-to-brittle transition regions ranging from -90°C to 21°C due to the particular focus in the recent SENB05 project where several specimens were unloaded before yielding brittle characteristics which in turn provided representative resistance curves. However, the fracture toughness specimens from Arctic Materials I did only supply a certain amount of valid crack growth values from the SENB05 and SENB02 test series. See Appendix D.4 for the comprehensive tables of the fracture mechanics test data which accurately characterise the validity of the experimental data for every specimen.

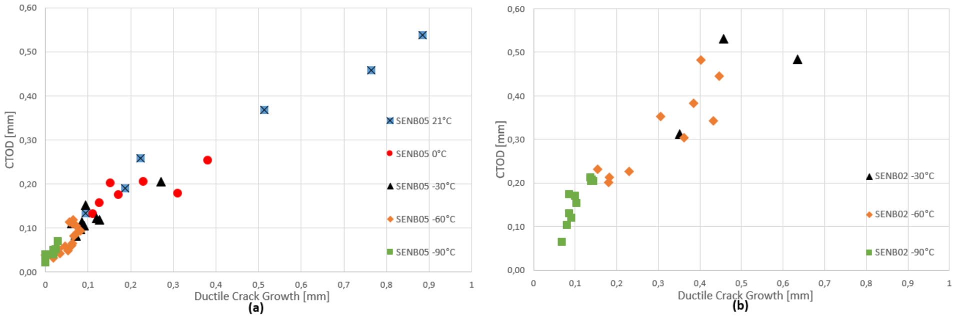

(a)

(b)

Figure 6.2: Experimental CTOD-Δa resistance curves at all temperatures (a) SENB05 Fracture and Unloading Values, (b) SENB02 Fracture Values

As exhibited in **Figure 6.2**, the measured crack growth and CTOD at low temperatures are notably smaller compared to the CTOD and crack growth at higher temperatures. Hence, the steel is brittle at lower temperatures where the material yields cleavage fracture at a microscopically low crack growth level and more ductile crack growth at higher temperatures. The material is able to endure additional crack growth prior to cleavage as the temperature increases due to the evolving plastic zone ahead of the crack tip as discussed in Section 2.6.5. For high temperatures in the upper transition and ductile regions, the material experience relaxation of both stress triaxiality and constraints which in turn lead to ductile tearing and a notably higher crack growth level.

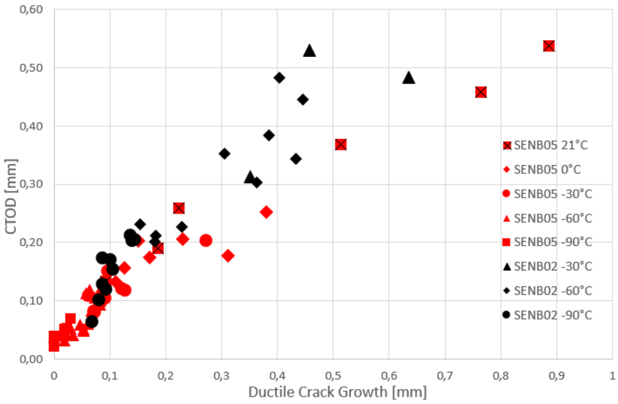

Figure 6.3: Experimental resistance curves. SENB05 (red) and SENB02 (black)

Figure 6.3 illustrates a comparison of the resistance curves in **Figure 6.2 (a) and (b)** which respectively represents the results from the SENB05 and SENB02 fracture mechanics test series. A rather strong geometry dependency emerges as the constraint level clearly affects the slope of the resistance curve. As SENB05 has a higher constraint level than SENB02, the resulting resistance curves illustrate an increasing slope with decreasing constraint level. However, the resistance curves are consistently linear even with shifting temperature for both geometries which in turn reveals a linear resistance curve trend independent of temperature and material characteristics.

The material requires increasing driving forces in order to maintain the crack growth level during crack extension, and as exhibited in **Figure 6.4**, the fracture toughness clearly increases with increasing temperature which is in agreement with the DBT discussion in Section 2.7. **Figure 6.4** exhibits all the *fractured* specimens from the fracture mechanics test series which experienced brittle failure. As the unloaded specimens are redundant in the subsequent sections concerning the probability of brittle failure they are exclusively used to make resistance curves to calibrate the Gurson parameters. More about the Gurson model with its constitutive Gurson parameter study in Section 6.3. All the fracture mechanics data from both the unloaded and fractured specimens are described in the comprehensive tables in Appendix D.4, and the valid fractured and unloaded DBTs are displayed in Appendix D.2.

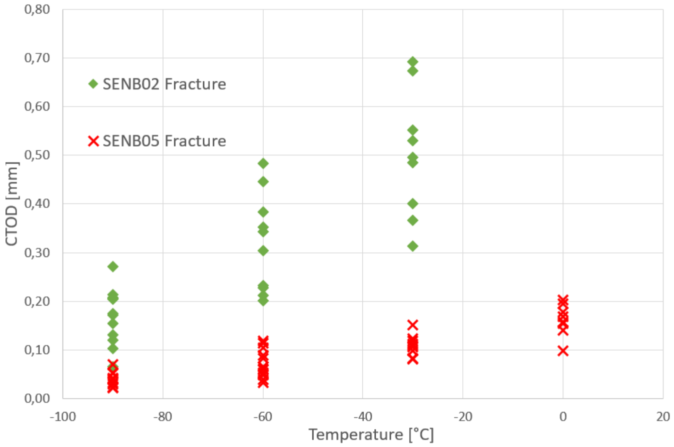

Figure 6.4: Experimental ductile-to-brittle transition fracture toughness scatter plot

The fracture toughness values illustrated in **Figure 6.4** are increasing with increasing temperature which in turn means the material follows a brittle-to-ductile transition from -90°C to 0°C. Some of the cleaved specimens at -30°C and 0°C exhibit a significant increase in CTOD compared to -90°C and -60°C which indicate a rather distinctive transition between -30°C and 0°C. The scatter expansion phenomenon is due to either the heterogeneous distribution of second-phase particles and defects as described in Section 2.2.2 and 2.3.1 or a bi-modal grain size distributed matrix material as described in Section 2.2.3. As the temperature increases, the mobility of dislocation increases accordingly, and it is required lower stresses in order to move them which in turn will increase the plastic deformation. However, at lower temperatures, the local stresses are high enough to break the local bonds and nucleate microcracks at broken second-phase particles which in turn leads to brittle fracture. The plastic flow during ductile tearing will ultimately lead to constraint relaxation which results in large fracture toughness scatter banners in the transition and ductile regions. The resulting scatter banner will a priori become larger as the geometry constraint level decreases, and the ductile-to-brittle transition temperature will decrease will decreasing constraint level as seen in **Figure 6.4**. Thus, the high constraint SENB05 fracture specimens will yield much lower fracture toughness values than SENB02 due to its high constraint level.

6.1.1 Experimental and Simulated Force-CMOD Curves

In order to get representative simulations in ABAQUS for further model implementation, the FE-models described in Section 5.2 must be established with material characteristics and boundary conditions which can accurately represent the experimental material behaviour from both the uniaxial tensile tests and the fracture mechanics tests. As discussed in Section 5.1.1, the constitutive material properties are defined from the true plastic flow curves which in turn are implemented as the FE-model material properties following the Ramberg-Osgood equation (5.3). The simulated Force-CMOD curves are compared with the corresponding experimental Force-CMOD curves in order to examine whether or not the FE-model and the constitutive material parameters can accurately describe the experimental material behaviour.

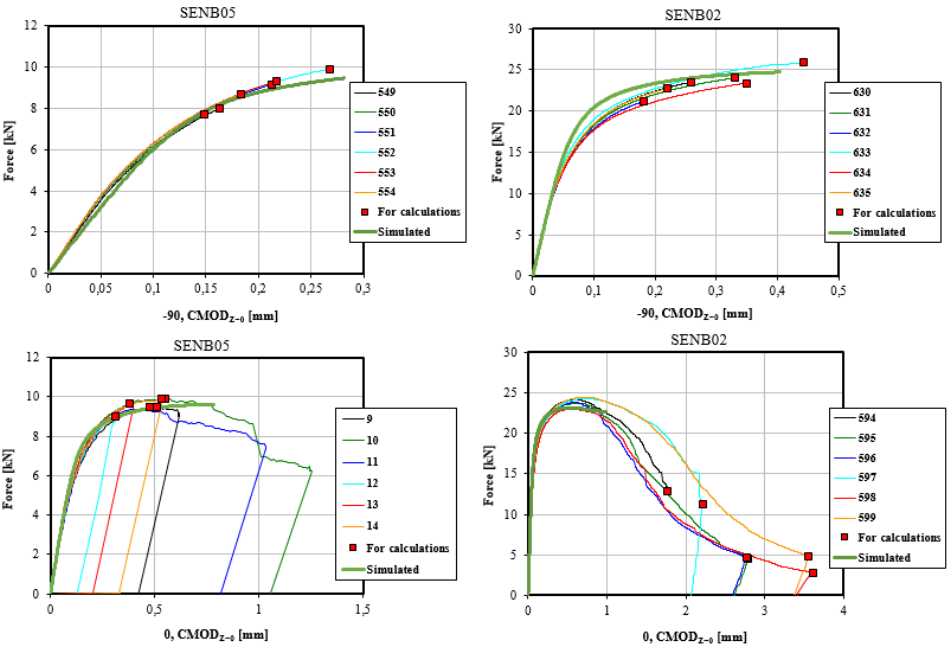

Figure 6.5: Simulated and experimental Force-CMOD. SENB05 and SENB02 at -90°C and 0°C

Figure 6.5 exhibits some of the experimental Force-CMOD curves with corresponding simulated Force-CMOD curves for SENB05 and SENB02 at -90°C and 0°C. The ABAQUS FE-models are able to simulate rather accurate Force-CMOD curves for both temperatures and fracture geometries which in turn means the FE-models can be used to simulate representative fracture mechanics test data. The red squares indicate the initially measured fracture data points where a few of them do not represent valid CMOD values as previously discussed in Section 6.1. All the simulated and experimental Force-CMOD curves are displayed in Appendix D.3, and the comprehensive fracture mechanics data tables containing valid fracture data are presented in Appendix D.4. All the simulated Force-CMOD curves fit the experimental Force-CMOD curves at all temperatures ranging from -90°C to 21°C which in turn means the FE-models are adequate to simulate representative fracture mechanics data throughout the ductile-to-brittle transition.

6.2 Probability of Brittle Failure Analysis

The Weibull-based Beremin model in Section 3.1.3 can be used to calculate the probability of brittle fracture, and the fracture criterion is exclusively based on the specimens yielding cleavage fracture. As the Beremin model is usually based on two or three-parameter Weibull distributions as discussed in Section 3.1.3, the constitutive distribution of the fracture toughness values and their corresponding scale and shape parameter must be determined in order to examine whether or not the weld simulated steel described in Section 5.1 has Weibull distributed fracture mechanics data.

The experimental fracture toughness values in **Figure 6.4** are sorted in ascending order, and the rank probability of each fracture toughness value is calculated following the mean rank probability in Equation 6.1 where i is the rank number of n specimens. As shown in **Figure 6.6**, the fracture data points from all the temperatures are plotted as a function of rank probability. The fracture data points as a function of temperature are with constant rank probability illustrating increasing fracture toughness with increasing temperature which in turn is evidence of a brittle-to-ductile transition. Thus, the material is able to endure more plastic deformation prior to cleavage fracture with increasing temperature due to dislocation movement and increased plastic zone in front of the crack tip.

$$P_F = P_{rank} = \frac{i - 0.3}{n + 0.4} \qquad , i \in [1, n] \tag{6.1}$$

The two-parameter Weibull distribution is considered to represent the fracture toughness distribution as it will also be recognised in subsequent Beremin model sections. The cumulative distribution function of the two-parameter Weibull distribution is defined by Equation 6.2 where λ is the scale parameter, δ is the CTOD, and k is the shape parameter.

$$P_F(\delta) = 1 - e^{-(\delta/\lambda)^k} \tag{6.2}$$

The scale parameter represents the fracture toughness value at 63.2% $(P_F = 1 - e^{-1})$ probability of failure and λ is the flaw distribution of the fracture dataset where a large shape parameter is equivalent with a steep Weibull CDF. Thus, both the Weibull parameters must be estimated in order to conclude whether or not the material fracture toughness data follows a two-parameter Weibull distribution.

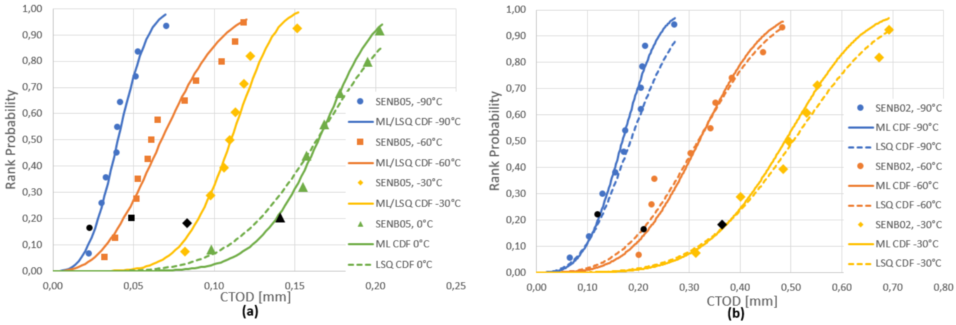

Figure 6.6: Cumulative distributions of (a) SENB05 (high constraint), (b) SENB02 (low constraint) ML = Maximum Likelihood, LSQ = Least Square, CDF = Cumulative Distribution Function

As discussed in Section 5.3.1, there are primarily two methods to estimate the constitutive Weibull parameters in a two-parameter Weibull distribution. One method is to utilise maximum likelihood estimation (MLE) which in turn estimates the parameters by maximising a likelihood function of the given fracture data. [87] [95] The parameters are thus readily estimated by utilising integrated Weibull fitting functions in Matlab as described in Appendix B.1. The second method is to solve Equation 6.2 directly by utilising mean least square (LSQ) linear regression. First, the Weibull probability of failure is rearranged before natural logarithms are done twice which in turn yields:

$$ln\left[ln\left(\frac{1}{1-P_F(\delta)}\right)\right] = k \cdot ln(\delta) - k \cdot ln(\lambda) \tag{6.3}$$

Equation 6.3 follows a linear regression function where $ln[ln(\frac{1}{1-P_F(\delta)})]$ represents y, k is the slope of the curve, $ln(\delta)$ is the variable x, and $k \cdot ln(\lambda)$ is the constant, c yielding the linear regression function $y = k \cdot x + c$. By conducting the latter procedure, all the fracture data points in **Figure 6.6** are converted accordingly. Mean least square linear regression of the converted fracture data points are then conducted which in turn results in the linear regression curves in **Figure 6.7**.

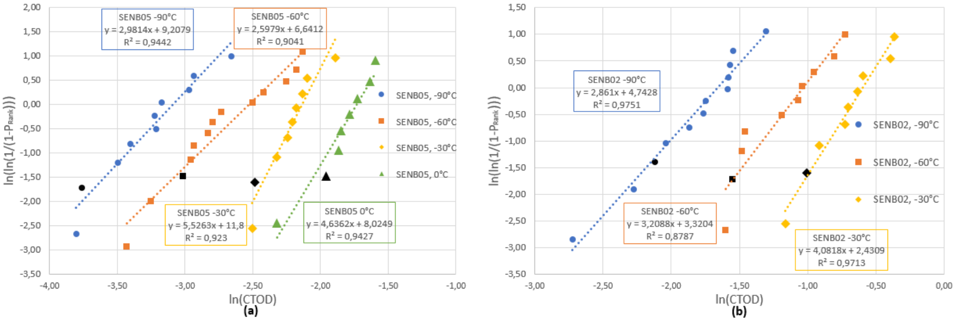

Figure 6.7: Ln-ln plot of rank probability and CTOD. (a) SENB05, (b) SENB02. Black data points indicate MOTE values according to **Table D.1**

The fracture data points in **Figure 6.7** follows a somewhat linear trend which partly confirms a two-parameter Weibull distribution. The fracture data points in **Figure 6.7 (a)** fit the linear regression functions except for some of the lowest fracture toughness values and a population of fracture data points at -60°C. The deviating population may be due to material heterogeneity or different defect populations in the weld simulated CGHAZ. A similar trend is displayed in **Figure 6.7 (b)** where a few fracture toughness points at -60°C deviate from the original regression function. The resulting square roots, R^2 can be used to determine the accuracy of the mean least square regression curves which in turn also indicate poor values for the fracture mechanics test series at -60°C. As seen from the resulting slopes in **Figure 6.7** and the plotted parameter trend in **Figure 6.8**, the mean least square estimated shape parameter is increasing with temperature. However, the scale parameter is also increasing with increasing temperature as the material becomes more ductile and exhibits larger fracture toughness values. The relatively constant shape parameter between -90°C and -60°C in **Figure 6.8** is likely due to the brittleness of the material. As the material is still in the brittle region at -60°C, the flaw distribution should a priori remain relatively constant throughout the brittle region. The material allows more dislocation movement with increasing temperature, but as the material is still brittle the flaw distribution will remain relatively constant. Further, the scale parameter increases linearly with temperature which is evidence of enhanced plastic blunting and ductility with increasing temperature where the material will endure increased plastic deformation before reaching 63.2% probability of brittle failure. The steep SENB02 scale parameter trend in **Figure 6.8 (b)** is due to its low constraint level which evidently leads to larger fracture toughness values compared to the SENB05 specimens. However, the shape parameter in **Figure 6.8 (b)** does not exhibit the same transition trend as in **Figure 6.8 (a)** which may indicate the SENB02 specimens already have entered the lower transition region at -90°C even though the resulting shape parameters are somewhat identical when comparing the corresponding values in **Figure 6.8 (a) and (b)**

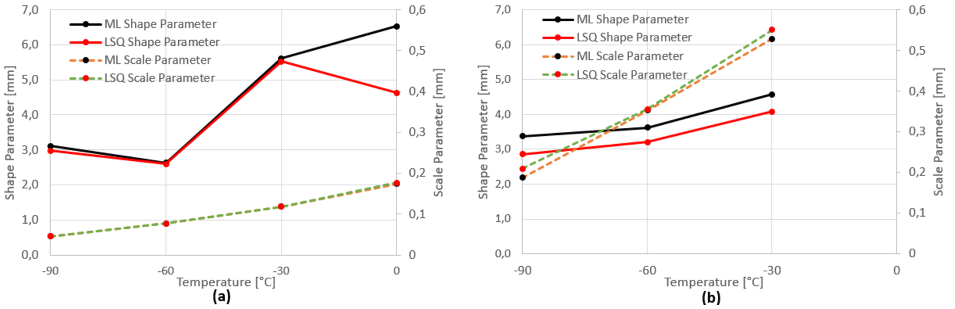

Figure 6.8: Scale and shape parameter transitions. (a) SENB05, (b) SENB02
ML = Maximum Likelihood, LSQ = Least Square

The maximum likelihood estimation and the mean least square method should yield a priori approximately the same parameter estimates. As exhibited in **Figure 6.8 (a)**, the curves are identical except for the mean least square estimated shape parameter which is deviating from the maximum likelihood estimated shape parameter at 0°C. The maximum likelihood shape parameter is characterised as the most probable estimate as the shape parameter a priori should not decrease with increasing temperature. The CDF curves are plotted by generating random material data in order to find the most accurate parameter estimates by utilising integrated Matlab functions along with a Matlab script as described in Appendix B.1. The resulting LSQ and ML CDF curves in **Figure 6.6 (a)** at 0°C fit the fracture data points. However, the LSQ CDF curve highly overestimates the fracture probability of the lowest fracture data point which results in an inaccurate prediction of several subsequent data points. Thus, the maximum likelihood estimate is the most accurate which in turn means the increasing shape parameter trend in **Figure 6.8** prevails. The remaining CDF curves follow the same trend functions and are thus able to represent the fracture toughness in **Figure 6.6** accurately.

The resulting MLE cumulative distribution functions can then be used to establish confidence intervals for the ductile-to-brittle transition of both crack configurations. The MLE CDFs follows the two-parameter Weibull cumulative failure probability in Equation 6.1 where the Weibull parameters are separately estimated at all the test temperatures. As exhibited in **Figure 6.9**, the MLE [10%, 90%] confidence intervals can account for the whole fracture toughness scatter except for a few extreme values. In conclusion, the constitutive fracture toughness data, parameter regression curves, and Weibull CDFs are evidence of a material which follows a two-parameter Weibull distribution which in turn allows further analysis of the Weibull parameters in the Beremin model.

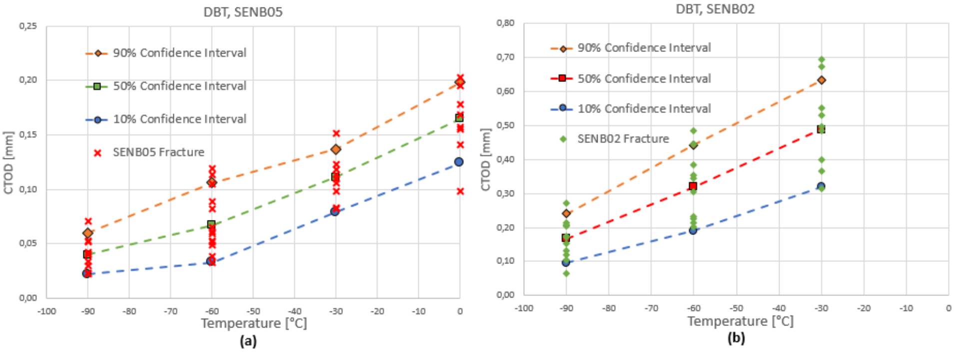

Figure 6.9: Ductile-to-brittle transition and MLE Weibull confidence intervals
(a) SENB05, (b) SENB02

6.2.1 Beremin Model: Weibull Parameter Study

The constitutive Weibull parameters must first be calibrated accordingly in order to conduct representative simulations with the Weibull-based Beremin model. The true plastic flow curves are initially implemented as the material properties in the FE-model to account for the applicable stress-strain relationship for both elastic and plastic behaviour. However, the Weibull parameter calibration procedures are limited to the solely brittle region as the original Beremin model is based on the flaw distribution of defects without any extent of ductile tearing. The SENB05 fracture mechanics test series comprise ten valid fracture data points at -90$^\circ C$ and thirteen valid fracture data points at -60$^\circ C$.

Both the maximum likelihood parameter estimation and the mean least square method described in Section 5.3.1 are conducted at -90$^\circ C$ and -60$^\circ C$ to calibrate the constitutive Weibull parameters for SENB05 and ultimately other fracture geometries. The time increments of the corresponding critical fracture toughness values are first identified in the ABAQUS FEA which in turn provides all the critical fracture data points to consider in the subsequent Weibull calibration procedures. Thus, by utilising the in-house finite element post-processing program LINKpfat, the corresponding Weibull stresses can be calculated. The reference volume, V_0 is taken equal to $0.001mm^3$ (detailed mesh element volume), and the thickness and symmetry axes are accounted for in the LINKpfat simulation model (.pfp) in order to represent a full-scale 3D fracture mechanics test specimen.

For the mean least square parameter estimation, the critical Weibull stresses are first arranged in ascending order, and corresponding rank probabilities are calculated for each fracture specimen by utilising the mean rank probability in Equation 6.1. Thus, the Weibull modulus can a priori be calibrated by conducting the iterative calibration procedure described in Section 5.3.1. A similar process is independently conducted with the maximum likelihood estimation method which is solely based on the critical Weibull stresses and the Weibull cumulative failure probability in Equation 6.4.

$$P_F(\sigma_w) = 1 - exp\Big[- \Big(\frac{\sigma_w}{\sigma_u}\Big)^m \Big] \tag{6.4}$$

However, neither of the Weibull parameter calibration methods are able to converge the Weibull modulus to a specific value. As exhibited in **Figure 6.10**, the Weibull modulus converges exponentially regardless of the calibration method. The same calibration procedure was conducted at -60$°C$ as it comprised three more fracture specimens but the same exponential Weibull modulus trend prevails. There are several explanations for this particular phenomenon; the material experiences some extent of ductile tearing before fracturing, the constraint effects are inconsistent without a ductile simulation model, or the amount of fracture mechanics data in the test series is too small to calibrate the Weibull parameters accurately. Inadequate model sectioning in LINKpfat will also promote large Weibull parameter confidence intervals and must be taken into consideration when calibrating the constitutive Weibull parameters.

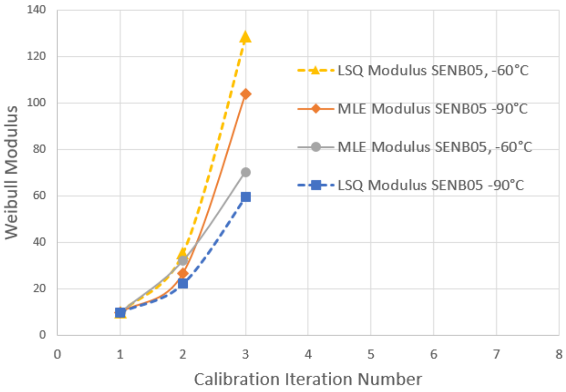

Figure 6.10: SENB05 LSQ and MLE Weibull modulus calibration

The most probable explanations for the non-converging Weibull modulus are the limited fracture dataset or inadequate model sectioning in LINKpfat. Due to the small set of fracture data points, the resulting Weibull modulus confidence interval becomes substantially large for each iteration and is unable to converge the Weibull modulus estimate. The first iteration of the Weibull dataset results in the 90% Weibull modulus confidence interval [19.3, 25.0] which is too large to accurately estimate the Weibull modulus. Similar non-converging Weibull modulus prevails in several scientific papers, and one example is when Bakker & Koers [73] tried to determine the Weibull modulus for ferritic steel. They were unable to converge the Weibull modulus estimate at -110$°C$ with about twenty fracture data points, but the same calibration procedure was successful at -170$°C$ with the same amount of fracture data points. Hence, the latter phenomenon demonstrates the extreme limitation to both the maximum likelihood estimation and the mean least square method concerning both microscopical plasticity and the extent of fracture mechanics data.

An alternative approach is thus used to get proper Weibull parameter estimates as the initial Weibull modulus calibration procedures are unable to converge the Weibull parameter estimates for one single fracture mechanics geometry. As discussed in Section 5.3.1, the Weibull parameters can be estimated by toughness scaling two fracture mechanics geometries with different constraint levels which in turn eliminates the non-uniqueness in the previous calibration methods. The Weibull-based toughness scaling of one high constraint geometry (SENB05) and one low constraint geometry (SENB02) will a priori be able to estimate a unique Weibull modulus which can constraint-correct the two fracture geometries with identical Weibull cumulative distribution functions following Equation 6.4. The toughness scaling as a calibration method will thus be able to estimate a unique set of Weibull parameters at the respective temperature if both the fracture geometries are in the solely brittle region with no ductile tearing prior to cleavage fracture.

As exhibited in **Figure 6.11**, when the constraint level increases the corresponding Weibull stresses as a function of fracture toughness will inevitably increase due to the elevated stress field ahead of the crack tip which in turn yields large local principal stresses at high constraint levels. However, the resulting Weibull stresses as a function of fracture toughness increases accordingly as the Weibull modulus is decreased which is reasonable as a decreasing Weibull modulus will promote larger Weibull stresses and steeper CDFs. The Weibull stress will after a certain amount of plastic deformation stabilise at a given Weibull stress due to the onset of constraint loss and a reduced rate of constraint relaxation under further loading as exhibited in **Figure 6.11**. However, the characteristic transition temperature for the different geometries will change due to the loss of constraint and is further discussed in the subsequent sections.

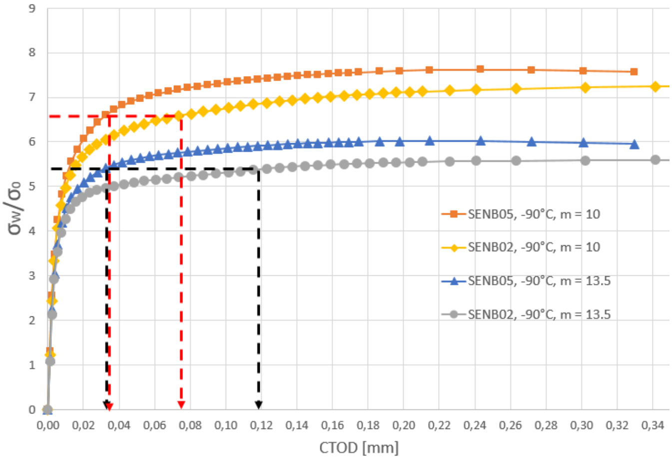

Figure 6.11: Toughness scaling and constraint effects. SENB05 and SENB02 fails at the same Weibull stress yielding the same probability of failure at different critical CTODs

One of the most exciting features of the constitutive Weibull stress functions in **Figure 6.11** is their ability to quantify constraint effects. As indicated with black and red stippled lines, identical Weibull stress can yield the same failure probability for two constraint levels with different fracture toughness at failure. As the Weibull stress scales with the failure probability, the Weibull stress will exclusively account for the local stress field ahead of the crack tip and can a priori be used to define equivalent fracture toughness values for different fracture geometries in the brittle region. The applicability of the toughness scaling is limited to the brittle region as the Weibull stresses will deviate considerably with ductile tearing as the current Beremin model does not simulate crack extension. Thus, overlapping critical Weibull stresses with equal rank probabilities means the Weibull parameters can constraint-correct the fracture geometries at the respective temperatures.

The toughness scaling is initially conducted at -90°C by comparing critical Weibull stresses with corresponding rank probabilities as both SENB05 and SENB02 are assumed to be in the solely brittle region at this temperatures. By following the toughness scaling procedure in Section 5.3.1, the two fracture geometries are constraint-corrected accordingly to calibrate a unique Weibull modulus estimate at -90°C. As exhibited in **Figure 6.12**, a range of Weibull modulus values are tested in order to find the best constraint-correcting estimate. The Weibull modulus, m = 13.5 in **Figure 6.12 (c)** is the best fit and can thus accurately constraint-correct the two fracture geometries. The appropriate fracture values are identified by utilising LINKpfat and the implemented ABAQUS database file (.odb) which in turn calculates Weibull stresses for the corresponding fracture toughness values. Thus, the resulting Weibull parameters yield equal Weibull stresses with equal probability of brittle failure for both fracture geometries at -90°C.

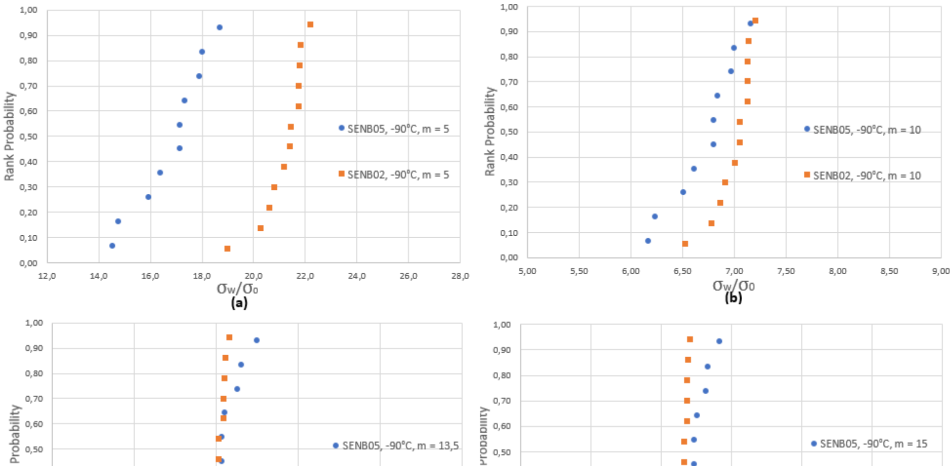

Figure 6.12: Toughness scaling: Weibull modulus estimation. SENB05 and SENB02. T = -90°C (a) m = 5, (b) m = 10, (c) m = 13.5, (d) m = 15

The simulated and experimental CDFs are then compared in **Figure 6.13**. The experimental failure probabilities are mean rank probabilities following Equation 5.5, and the theoretical CDFs are plotted with MLE Weibull parameters from the resulting critical Weibull stresses following Equation 6.4. The figure shows a good agreement between the MLE CDF curve and the experimental Weibull stresses when adopting the Weibull modulus, m = 13.5 in LINKpfat and the MLE scale parameter, σ_u = 4065MPa.

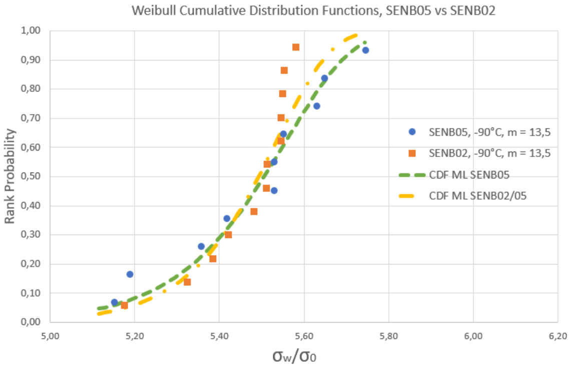

Figure 6.13: Rank probability vs normalised Weibull stress, m = 13.5, T = -90°C
MLE CDF for SENB05 and the aggregate MLE CDF for both SENB05 and SENB02

As exhibited in **Figure 6.13**, the resulting SENB02 critical Weibull stresses do not coincide perfectly with the MLE CDFs nor the critical Weibull stresses of the SENB05 fracture data points. The fit is perfect up until about 70% probability of failure where the SENB02 Weibull stresses become basically constant due to the constraint relaxation as shown in **Figure 6.11** where the Weibull stresses stabilise at large fracture toughness values. The relatively constant Weibull stress after 70% probability of failure may be evidence of ductile tearing prior to cleavage which in turn yields inaccurate Weibull stresses as the current Beremin model does not simulate crack extension nor constraint effects. The concave probability curve trend may also indicate a three-parameter Weibull distribution as discussed in Section 5.3.2 or inadequate model sectioning in LINKpfat leading to biased Weibull stresses at large plastic deformation. Nevertheless, the current toughness scaling with the constitutive Weibull parameters are considered as adequately accurate to quantify the constraint-correction in the brittle region.

6.2.2 Beremin Model: The Ductile-to-Brittle Transition

The original Beremin model is based on the assumption of material dependent Weibull parameters characterised from the microstructure. Hence, the parameters should a priori be independent of geometry and constraint level in the brittle region with predominant cleavage fractures and negligible ductile damage. A large Weibull modulus corresponds to narrow Weibull stress scatter bands and steep CDFs, and the resulting scale parameter is likely to decrease with larger m-values as the Weibull stresses become smaller at corresponding fracture toughness values.

Nevertheless, the calibrated Weibull modulus in Section 6.2.1 should a priori be able to account for the constraint-correction throughout the brittle region. As exhibited in **Figure 6.14**, the constant Weibull parameters can accurately describe the Weibull cumulative fracture probability for SENB05 at -60°C except for the deviating Weibull stresses between 40-70% probability of failure. However, the SENB02 Weibull stresses start deviating from the other distributions at about 50% which in turn can be evidence of either ductile damage or inadequate model sectioning in LINKpfat with biased Weibull stress computation. The material may endure lower critical Weibull stresses when constant Weibull parameters are assumed as the Weibull stress as a function of fracture toughness is seemingly decreasing with increasing temperature. Thus, the constant Weibull parameters cannot simulate representative Weibull stresses to describe the SENB02 fracture toughness scatter banner at -60°C and neither at the respective temperatures in the transition region.

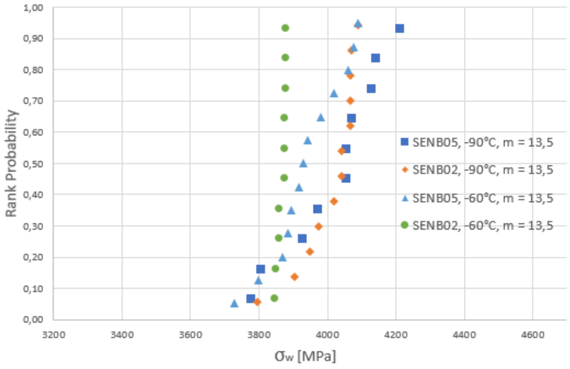

Figure 6.14: Rank probability vs Weibull stress in the brittle region SENB05 and SENB02 at -90°C and -60°C. m = 13.5

A full-scale DBT with temperature independent Weibull parameters can nonetheless be established by only considering the SENB05 fracture mechanics data. As exhibited in **Figure 6.15**, the MLE confidence intervals [10%, 90%] with constant and temperature independent Weibull parameters can be described for SENB05 from -90°C to 0°C. The confidence intervals are simulated by utilising the Weibull cumulative probability of failure following Equation 6.4 and the MLE Weibull parameters from the initial toughness scaling procedure in Section 6.2.1. The constant Weibull parameters and the constitutive confidence intervals can account for the whole fracture toughness scatter banner at both -90°C and -60°C which is expected from the preliminary study in **Figure 6.14**. At -30°C, the confidence intervals can account for the fracture toughness scatter banner even though the 50% and 10% confidence intervals somewhat overestimate the steel's brittleness. However, at 0°C, the confidence intervals are unable to accurately capture the whole fracture toughness scatter banner as the confidence intervals overestimate the steel's brittleness. The overestimated brittleness is expected as the current Beremin model does not simulate the appropriate crack extension nor constraint effects which in turn will yield large Weibull stresses due to non-existent constraint loss.

The original Beremin model with constant and temperature independent Weibull parameters is based on estimated Weibull parameters at the lowest temperature which in turn is a priori only able to predict accurate failure probabilities in the brittle region. As the material exhibit some extent of ductile tearing at both -30°C and 0°C (see **Figure 6.2**), the Beremin model will evidently not be able to calculate the appropriate Weibull stresses as the current model does not simulate crack growth in the elasto-plastic analysis.

The resulting confidence intervals in **Figure 6.15** are relatively linear with increasing temperature which in turn means they are unable to simulate the somewhat abrupt transition happening between -30°C and 0°C. The brittleness of the material is overestimated at both -30°C and 0°C and thus inadequate to simulate the increasing fracture toughness with increasing temperature. The non-consideration of the ductile damage effect on the stress-strain distribution in the transition region makes the current Beremin model with temperature independent Weibull parameters and no crack growth unable to accurately describe the ductile-to-brittle transition. Nevertheless, the current model is able to capture the changing stress-state with increasing temperature which is evidence of a brittle-to-ductile transition.

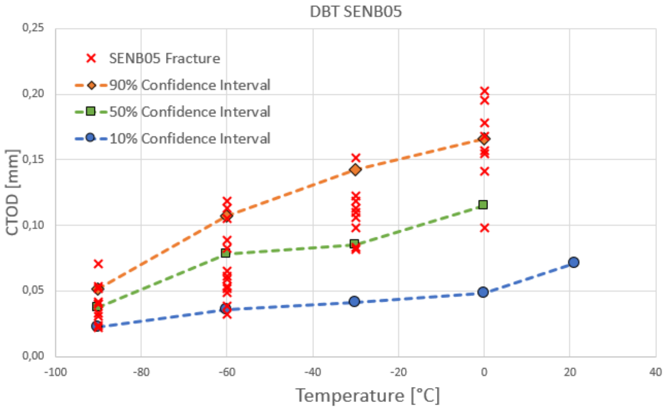

Figure 6.15: DBT SENB05: Beremin model with temperature independent Weibull parameters

A few theoretical concerns also arise with the current temperature independent Weibull parameters. As the plastic zone expands, the initial defect and microcrack distribution are assumed to be constant regardless of temperature which is questionable for ductile ferritic steels during plastic deformation. There is also frequently observed cleavage crack arrest at grain boundaries [81] or plastic blunting of microcracks at higher temperatures which violate the weakest-link principles described in Section 2.8.1. Hence, the original Beremin model needs an underlying model which can accurately simulate adequate crack growth and temperature dependent flow stress with ductile mechanisms. Thus, The Complete Gurson Model (see Section 3.2.1) is utilised to describe a more representative ductile-to-brittle transition by combining it with the Weibull-based Beremin model. The combined model should a priori be able to simulate representative material characteristics in all the DBT regions and provide the required ductile mechanisms to calculate appropriate Weibull stresses at high temperatures.

6.3 Ductile Tearing: The Complete Gurson Model

The Gurson model study is exclusively based on specimen SENB05$_A$ as described in Section 5.2 and **Table 5.3** since it is the only fracture geometry with the applicable fracture mechanics data in the ductile region. Hence, only the fracture toughness values exhibited in **Figure 4.1** and **Table 4.1** are utilised in the Gurson parameter study. The Complete Gurson Model is used to simulate ductile tearing from material void growth and void coalescence yielding loss of bearing capacity. Thus, the Gurson parameters f_0 and f_c are fitted at the highest temperature ($21°C$) with solely ductile characteristics in order to get representative simulation in the transition region.

6.3.1 Evaluation of Mesh Size and Blunting

As described in Section 5.2 and **Table 5.3**, two different mesh are tested; one with element size 0,05x0,05mm^2 and one with element size 0,05x0,10mm^2 along the crack ligament. The smaller element size is tested in order to get a higher resolution of the stress field ahead of the crack tip to get more representative principal stresses and plastic blunting. As exhibited in **Figure 6.16**, the resulting Gurson simulated resistance curve yields a steeper slope and simulates values closer to zero crack growth when reducing the element size at room temperature (21$°C$). The steeper resistance curve slope is equivalent to the effect from a smaller initial void volume fraction, f_0 as described in Section 6.3.2 and 5.4.2.

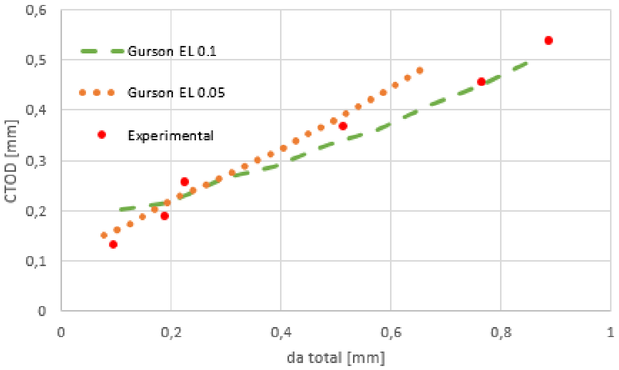

Figure 6.16: Element size effect on CTOD and total crack growth, f_0 = 0.0014, T = 21$°C$

The smaller mesh size initially seems like a better solution in order to get more accurate simulations. However, errors emerged in the output file when conducting the Gurson simulation with element size 0,05x0,05mm^2 at 0$°C$. The simulation is unable to obtain convergence for the equilibrium iterations between each time increment, and regardless of several cutbacks in the automatic time increments, the simulation is still unable to achieve convergence between the equilibrium iterations. This issue only emerges in the Gurson simulation at 0$°C$ with element size 0.05x0.05mm^2. The Gurson simulations at -60$°C$ and 21$°C$ work with the small element size, and all the simulations work with element size 0.05x0.10mm^2. The UMAT code with corresponding user subroutine in the Gurson model did not indicate any immediate reason for the convergence problem. Neither could the issue be solved by changing the time increment criteria in the input file nor by changing the base mesh size outside the critical damage zone along the crack ligament. The most likely reason for the convergence problem at 0$°C$ is an inconsistent UMAT description in the constitutive input file (.inp). However, element size 0.05x0.10mm^2 is utilised in all the simulations in the subsequent sections as it did not yield any errors when running the Gurson simulations which in turn also requires less computer power.

The Complete Gurson Model only accounts for the void growth and void coalescence which in turns means just ductile tearing is simulated with the Gurson model. Hence, the initial plastic blunting must be subtracted in order to estimate the appropriate Gurson parameters and fit the Gurson simulated resistance curve to the experimental results. Thus, the Gurson simulation results at 21$°C$ can be compared to the experimental ductile tearing in order to calibrate the constitutive Gurson parameters.

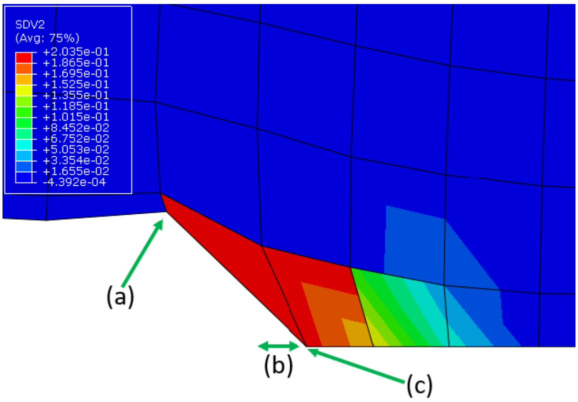

Figure 6.17: FE-model crack region. (a) CTOD-node, (b) Simulation Blunting, (c) Crack tip-node

As exhibited in **Figure 6.17**, the Gurson simulations in ABAQUS also present a small simulation blunting before ductile tearing initiating due to the large element size. The applicable simulation blunting must be subtracted from the ductile tearing values in order to get solely ductile tearing results from the Gurson simulation. The SDV2 value in **Figure 6.17** represents the state-dependent variable defined as the void volume fraction at the end of the time increment (see Appendix C.3).

6.3.2 Gurson Parameter Study

As shown in **Figure 6.16**, the Gurson simulated resistance curve at room temperature (21 $°C$) fits the experimental resistance curve with initial void volume fraction, $f_0 = 0.0014$. However, the Gurson parameters must be refitted when the experimental blunting and the simulation blunting illustrated in **Figure 6.17** are subtracted.

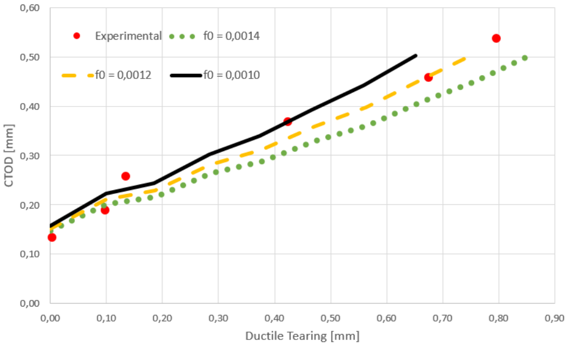

Figure 6.18: Gurson parameter study of the initial void volume fraction, f_0. T = $21°C$, $f_c = 0.2$

Only the initial void volume fraction, f_0 must be estimated since the preliminary Gurson resistance curve ($f_0 = 0.0014$) in **Figure 6.3.2** fits quite well at ductile tearing initiation. Thus, the resulting critical void volume fraction, f_c is defined as a by-product of the initial void volume fraction and is equal to 0.2 as it can accurately describe the appropriate resistance curve in **Figure 6.18**. As previously shown in **Figure 6.17**, the element starts tearing when SDV2 (current void volume fraction) exceeds 0.2 which in turn determines the critical void volume fraction, f_c where the element loses its bearing capacity.

The slope of the Gurson simulation curve increases with decreasing initial void volume fraction as exhibited in **Figure 6.18** where f_0 is readily fitted to the experimental results. f_0 = 0.0012 is chosen as the most suitable estimate and all the simulated resistance curves are extrapolated from 0.1 to zero ductile tearing as the Gurson simulated resistance curves should a priori be linear immediately after ductile tearing initiation. The slope trend is thus reasonable as smaller initial void volume fractions will constitute elements that require additional void-induced damage before reaching the critical void volume fraction.

6.3.3 Gurson: Resistance Curves

As discussed in Section 5.4, the CTOD values as a function of ductile tearing can be plotted after all the Gurson simulations are conducted and analysed accordingly. The original material data from the recent SENB05 test series are utilised to illustrate the Gurson resistance curves as they represent all the ductile-to-brittle transition regions. The R-curves are presented in **Figure 6.19** and compared to the experimental crack growth results.

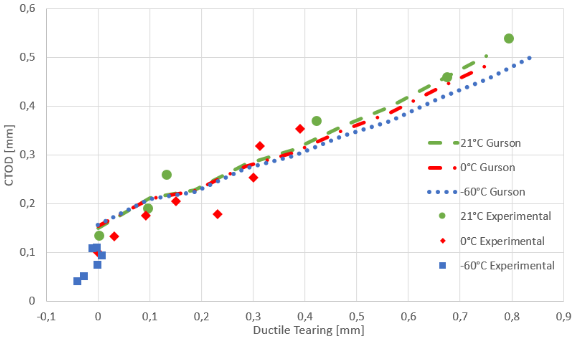

Figure 6.19: Gurson simulated resistance curves and experimental crack growth. Negative values at -60°C due to the large average experimental blunting

As shown in **Figure 6.19**, the Gurson simulation fits the experimental values at 21°C which is expected as the Gurson simulated R-curve is initially fitted to the experimental ductile tearing at room temperature. The initial void volume fraction, f_0 is temperature independent, and the true plastic flow curves from the respective temperatures are the only temperature dependent parameters. As shown in **Table 5.1**, the yield strength increases with decreasing temperature which in turn indicates that the material becomes more brittle with decreasing temperature. Since the Gurson model is unable to describe brittle characteristics, the Gurson model should exhibit some problems in the 0°C simulation as the material exhibit concurrent ductile and brittle mechanisms. Nevertheless, as shown in **Figure 6.19**, the remaining experimental ductile tearing fits the Gurson simulated resistance curve when the experimental blunting is subtracted.

At -60°C, the experimental results exhibit no ductile tearing prior to cleavage which in turn demonstrates solely brittle characteristics. As shown in **Figure 6.19**, the Gurson simulated resistance curve does not fit the experimental values at -60°C which is expected as the Gurson model is unable to describe the plastic blunting prior to ductile tearing initiation.

The Gurson model is unable to describe the crack growth under $0.1mm$ and CTOD values under $0.15mm$ due to the large element size and the relatively low mesh resolution which in turn cannot describe the correct plastic blunting at the crack tip. Thus, smaller element size and higher mesh resolution are initially tested to characterise the plastic blunting. However, the current subroutine with its constitutive Gurson parameters cannot solve the resolution challenge as described in Section 6.3.1. The temperature dependence of the experimental and simulated resistance curves are illustrated in **Figure 6.19** as lower temperatures yield smaller CTOD with corresponding Δa which is reasonable as brittle materials promote horizontal resistance curves as described in Section 2.6.5. However, the Gurson model is simulating material softening and ductile tearing regardless of temperature which in turn results in sloped resistance curves even in the brittle region.

In order to conclude whether or not the constitutive Gurson simulation models can simulate accurate ductile crack growth (plastic blunting and ductile tearing), the experimental blunting is added to the simulated ductile tearing curves instead of subtracting the experimental blunting from the experimental results. Thus, the difference between the experimental and simulated resistance curves is unaffected after ductile tearing initiation. The blunting can then be extrapolated to the origin by assuming constant plastic blunting rate following the theoretical resistance curve trend in **Figure 2.10**. As shown in **Figure 6.20 (a)**, the simulated SENB05 resistance curves can describe accurate plastic blunting and ductile tearing regardless of temperature which in turn means the simulation models are consistent for the whole ductile-to-brittle transition.

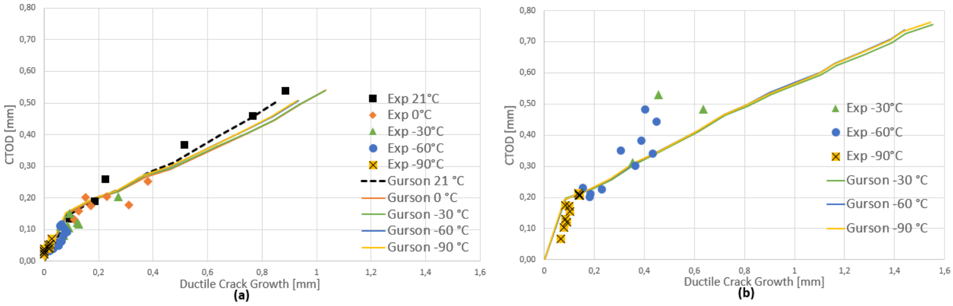

Figure 6.20: Simulated and experimental resistance curves. (a) SENB05, (b) SENB02

The accuracy of the simulated plastic blunting is also reasonable as all the specimens at -90°C and -60°C cleaved before ductile tearing initiation where the simulations precisely characterise the Force-CMOD curves as shown in **Figure 6.5 and D.6**. The simulated resistance curves follow the same ductile tearing trend up until about $\Delta a = 0.4$ where the 21°C R-curve deviates from the other curves which in turn is reasonable as the material is in the solely ductile region at 21°C and should simulate a steeper resistance curve.

However, the simulated SENB02 resistance curves in **Figure 6.20 (b)** are not entirely consistent with the experimental results. The slope during ductile tearing is too low to simulate the experimental values accurately at -60°C and -30°C where the simulation overestimates the ductile tearing as a function of fracture toughness. Nevertheless, the resulting plastic blunting and ductile tearing are relatively accurate for the lowest temperatures and can be considered as adequate for simulations in the brittle region and the lower transition region. A smaller initial void volume fraction would be able to simulate perfect SENB02 resistance curves, but it must remain identical for both fracture geometries as f_0 is defined as a material dependent parameter. All the simulated resistance curves are approximately similar when the experimental blunting is incorporated which is predominantly due to the constant and temperature independent Gurson parameters even though the true plastic flow curves are temperature dependent material parameters. As exhibited in **Figure 6.20 (a)**, all the specimens at -90°C and -60°C fail during blunting which in turn means the SENB05 specimens are in the solely brittle region at the respective temperatures. However, the fractured specimens in **Figure 6.20 (b)** do not fail during blunting at -60°C and exhibit ductile tearing prior to cleavage which may indicate the specimen is in the lower transition region. At -90°C, most of the SENB02 specimens fail during blunting which in turn demonstrates a brittle-to-transition region shift between -90°C and -60°C.

As shown in **Figure 6.21**, the simulated resistance curves for SENB05 and SENB02 at 21°C are essentially the same in the blunting phase and both rise at a constant rate during crack extension. The simulated resistance curves depend on the crack growth where deeper initial crack and higher constraint level lead to lower CTOD values for the corresponding crack extension. Nevertheless, the moderately increasing trend shows a relatively weak crack size dependence from the simulated R-curves. However, the resulting resistance curves can be utilised to describe geometry transferability of different constraint levels in order to assess fracture toughness estimates and crack extension.

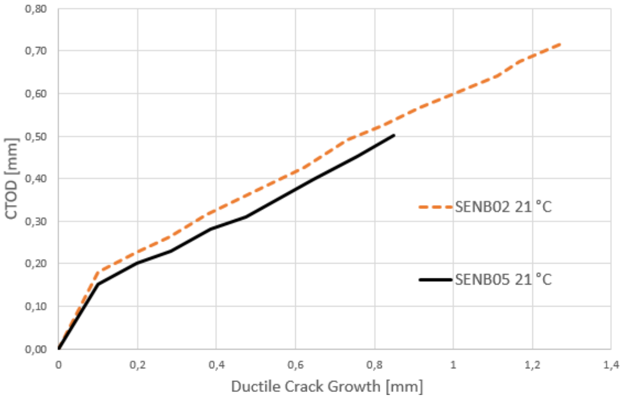

Figure 6.21: Simulated resistance curves. SENB02 and SENB05 at 21°C. $f_0 = 0.0012$

In conclusion, The Complete Gurson Model with its constitutive Gurson parameters fitted in the ductile region is able to accurately simulate ductile crack growth for a range of temperatures and constraint levels. However, even though the simulation scheme can accurately simulate plastic blunting at low temperatures when assuming constant plastic blunting rate prior to ductile tearing initiation, the Gurson model is unable to describe the cleavage fracture initiation nor any brittle characteristics. Thus, the Weibull-based Beremin model as a post-processing routine is combined with The Complete Gurson Model to describe when brittle failure prevails and to compute the appropriate probability of brittle failure throughout the ductile-to-brittle transition.

6.4 The Beremin-Gurson Model

The Complete Gurson Model and the Weibull-based Beremin model are in this section combined in order to simulate appropriate ductile mechanisms and calculate the probability of brittle failure throughout the ductile-to-brittle transition. The Gurson model with its constitutive Gurson UMAT is used as the FE-model material constituting temperature dependent true plastic flow curves and temperature independent Gurson parameters. The Beremin model is then used as a post-processing routine in combination with the Gurson UMAT to calculate the probability of brittle failure as described in Section 3.3.2. The Gurson parameters are calibrated by fitting simulated and experimental resistance curves at the highest temperature in the ductile region, and the Weibull parameters are calibrated at the lowest temperature in the brittle region. The following list constitutes the consecutive steps in order to develop the Gurson UMAT and calibrate the constitutive material parameters for both The Complete Gurson Model and the Weibull-based Beremin model.

1. **Determine material properties:** Conduct uniaxial tensile tests at all temperatures
   (a) Analyse the engineering stress-strain curves
      i. Determine the material parameters; E, v, σ_{ys} and σ_{UTS}
   (b) Review and plot true plastic flow curves
      i. Calculate the true stress and true strain and plot the equivalent true plastic flow curves for all temperatures
      ii. Calibrate the stress hardening exponent, n by fitting the Ramberg-Osgood equation to the experimental true plastic flow curves. Generate true plastic flow curves with a manageable small dataset for simple FE-model material implementation
2. **Fracture mechanics data analysis**: Conduct SENB fracture mechanics tests and review the material output data
   (a) Conduct fracture mechanics tests
      i. Measure and describe the concurrent mid-point load and CMOD. Plot the corresponding Force-CMOD curves
      ii. Measure the plastic blunting and ductile tearing of all the specimens by cracking them open and then use the nine-point measuring procedure to calculate the equivalent crack extension
   (b) Analyse the reliability of the experimental data
      i. Study the experimental Force-CMOD curves to identify valid and invalid fracture mechanics data. Exclude the invalid fracture mechanics data
      ii. Calculate the CTOD values by utilising the corresponding CMOD and Δa-values at valid fracture data points (see Section 2.6.4)
   (c) Plot the experimental scatter of all the fractured specimens in order to describe the ductile-to-brittle transition as a function of CTOD

3. **Develop the ABAQUS Gurson UMAT:** Establish the FE-model material
   (a) Create ABAQUS finite element models with adequate boundary conditions and displacement according to the experimental fracture mechanics tests
      i. Establish a detailed mesh ahead of the crack tip with a mesh element length, $l_c = 0.10mm$ or smaller
      ii. Incorporate temperature dependent true plastic flow curves, E, v, n, and σ_{ys} as material parameters
      iii. Compare simulated and experimental Force-CMOD curves to examine the accuracy of the simulation models
   (b) Set $f_c = 0.2$ and $f_0 = 0.0012$ as the initial Gurson parameter estimates. Calibrate f_0 by fitting the simulated and experimental resistance curves at the highest test temperature. The fitting procedure should be carried out without experimental and simulated blunting
4. **Examine the fracture toughness distribution:** Check whether or not the experimental fracture toughness values follow the two-parameter Weibull distribution
   (a) Calculate the mean rank probabilities for all the fractured specimens and their corresponding fracture toughness values
   (b) Plot rank probabilities as a function of fracture toughness at all temperatures
   (c) Estimate Weibull parameters at all the temperatures by either utilising the mean least square method or the maximum likelihood estimation method in Matlab: $phat = wblfit(data)$
   (d) Plot the resulting Weibull cumulative distribution functions by utilising the estimated Weibull parameters and the integrated Matlab function: $cdf = wblcdf(data, phat(1), phat(2))$
5. **Calibrate the Weibull parameters:** Combine the Gurson UMAT as the FE-model material with the Weibull-based Beremin model
   (a) Establish a LINKpfat simulation (.pfp) and implement the ABAQUS database file
      i. Set the reference volume, $V_0 = 0.001mm^3$
      ii. Set the analysis type to Weakest Link, define the material from the ABAQUS database file (.odb), measure first principal stresses from nodes, and specify the correct symmetry axes and thickness of the specimen
      iii. Define the initial Weibull modulus estimate, $m_0 = 10$
   (b) Calibrate the Weibull parameters with one fracture mechanics geometry
      i. Identify critical Weibull stresses corresponding to critical experimental fracture toughness values in the LINKpfat simulation at the lowest temperature
      ii. Utilise either the mean least square method or the maximum likelihood estimation method to calibrate the Weibull parameters (see Section 5.3.1)

(c) Contingency/Alternative approach: Calibrate the Weibull parameters by toughness scaling two fracture geometries with different constraint levels
   - i. Identify the critical Weibull stresses corresponding to the critical experimental fracture toughness values in the LINKpfat simulation for both the fracture geometries at the lowest temperature
   - ii. Calculate the rank probabilities for the corresponding critical Weibull stresses and compare the results from the two fracture geometries
   - iii. Repeat step ii by changing the Weibull modulus until the cumulative rank probabilities with equivalent Weibull stresses coincide
   - iv. (If applicable) Use the Weibull modulus from step iii as m_0 to toughness scale the critical Weibull stresses at the remaining temperatures in order to find the temperature dependent Weibull parameters

The material properties and the calibrated parameters from Section 5.1, 6.2.1, and 6.3 are described in **Table 6.1**. All the Gurson and Weibull parameters are temperature independent in the preliminary study, and only the true plastic flow curves are temperature dependent.

Table 6.1: Constitutive parameters from the uniaxial tensile tests, fracture mechanics tests, and the preliminary temperature independent Gurson and Beremin studies

T $^\circ C$	E [GPa]	v	σ_{ys} [MPa]	σ_{UTS} [MPa]	f_0	f_c	l_c [mm]	m	σ_u [MPa]
-90	208	0.3	733	1001	0.0012	0.2	0.10	13.5	4065
-60			697	961					
-30			680	931					
0			676	900					
21			667	889					

6.4.1 Temperature Independent Weibull Parameter Study

The original Beremin model is able to constraint-correct SENB05 and SENB02 in the brittle region but is unable to account for the changing stress state and constraint effects during ductile tearing. Hence, the preliminary Beremin model is inadequate to accurately compute the probability of brittle failure in the transition region when temperature independent Weibull parameters are assumed. The Complete Gurson Model is combined with the original Beremin model by incorporating the Gurson UMAT as the FE-model material to describe the appropriate ductile mechanisms and crack extension. Thus, the combined model can a priori describe the geometry constraint effects as both the simulated resistance curves in **Figure 6.20** and the simulated Force-CMOD curves in **Figure 6.5** correlates with the experimental results.

The Beremin-Gurson Weibull modulus is first estimated by conducting two separate calibration methods. As described in Section 5.3.1, the mean least square and maximum likelihood estimation methods are utilised to calibrate Weibull modulus estimates by only considering one fracture geometry. As exhibited in **Figure 6.22**, the two calibration methods are able to converge respective Weibull modulus estimates, but the estimates converge to different values. The mean least square method estimates, $m = 17.6$, and the maximum likelihood estimation method estimates, $m = 22.5$ which in turn means one or both

Weibull modulus estimates might be biased. The small fracture dataset yields large estimate confidence intervals which in turn means both the calibration methods might result in biased Weibull modulus estimates.

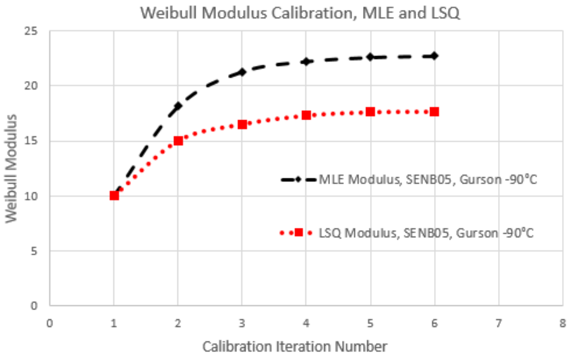

Figure 6.22: SENB05: Iterative Weibull modulus calibration. Gurson UMAT. T = -90°C

As exhibited in **Figure 6.22**, both the calibration methods only require a limited amount of calibration iterations and converge approximately at the same rate. Thus, the Beremin-Gurson approach is compared to the original Beremin model in Section 6.2.1 able to calibrate appropriate Weibull modulus estimates with a small fracture dataset by only considering one fracture geometry. The Gurson UMAT simulates higher stresses at large plastic blunting which in turn calculates critical Weibull stresses following the two-parameter Weibull distribution in Equation 6.4. However, the plain material without Gurson material equations in the original Beremin model is unable to simulate the Weibull distribution precisely which is evidently due to the large estimate confidence intervals and inadequate model sectioning in LINKpfat.

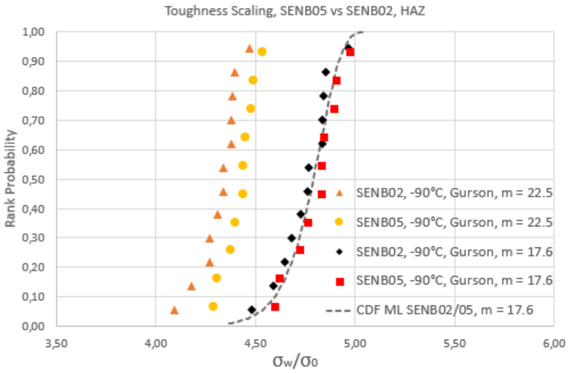

Figure 6.23: Toughness scaling to determine the best Weibull modulus estimate

Toughness scaling of the critical Weibull stresses from SENB02 and SENB05 can readily be performed at -90°C instead of bias-correcting both the Weibull modulus estimates. As shown in **Figure 6.23**, $m = 22.5$ is unable to constraint-correct the probability of brittle failure with corresponding critical Weibull stresses. However, $m = 17.6$ is able to constraint-correct the fracture geometries at -90°C which in turn confirms the Weibull modulus estimate from the mean least square calibration procedure as adequate without any significant bias-correction.

The original Beremin model is based on the weakest-link principles in Section 2.8.1 and Weibull stress calculation based on plastic elements exhibiting principal stresses which exceed the yield strength as discussed in Section 3.1.3. However, the LINKpfat Weibull stress calculation program bases its calculation on the weakest-link principles of all the elements regardless of stress level. Thus, the calculated Weibull stress can be severely biased when considering the whole FE-model. As exhibited in **Figure 6.24**, the full-scale model highly overestimates the Weibull stress as the base model accommodate a significant amount of elements with intermediate stresses which do not exceed the yield strength.

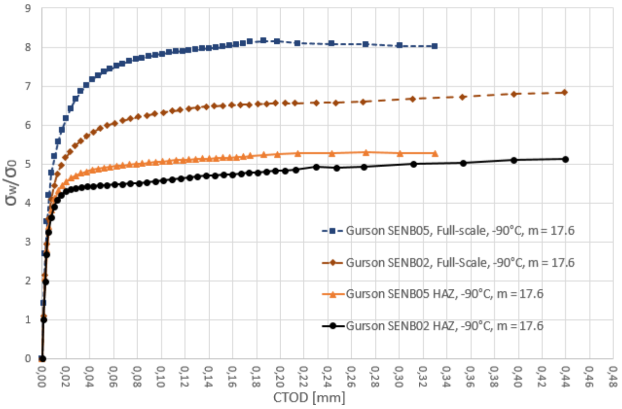

Figure 6.24: Model sectioning effects. The full-scale model compared to the heat affected zone

The resulting Weibull stresses from the full-scale model might be able to describe the ductile-to-brittle transition of the individual fracture specimen geometries as the constitutive Weibull stresses will change accordingly with temperature. However, the constraint-correction remains beyond the bounds of possibility as the SENB05 model will simulate higher Weibull stresses compared to the SENB02 model due to its high constraint level and amount of intermediate principal stresses in the model body. Thus, the ABAQUS model is sectioned with separate model body and weld zone to solve the weakest-link limitation in LINKpfat. As shown in **Figure 6.23 and 6.24**, the resulting Weibull stresses from the heat affected zones can be constraint-corrected with identical Weibull stresses following the same fracture probability distribution.

The Weibull stresses are affected by the constraint effects during ductile tearing and the onset of constraint relaxation when the Gurson UMAT is combined with the Beremin post-processing routine. Thus, the constraint relaxation will prevail at two separate crack extensions due to the different constraint levels in SENB05 and SENB02. As exhibited in **Figure 6.25**, the Weibull stress in the SENB05 weld zone increases with increasing crack extension until reaching 0.3mm ductile tearing. The constraint effects ahead of the crack tip leads to elevated stress fields during crack growth which in turn results in higher Weibull stresses. The constraint relaxation starts dominating after a certain amount of ductile tearing which in turn will cause lower Weibull stress with further crack extension. The same phenomenon appears in the SENB02 weld zone where the constraint effects prevail until 1.2mm ductile tearing before the specimen starts experiencing constraint relaxation. SENB05 has a high constraint level compared to SENB02 which in turn leads to a steeper Weibull stress elevation at small crack extensions which is a priori reasonable as the SENB05 specimens yield lower fracture toughness due to its high constraint level.

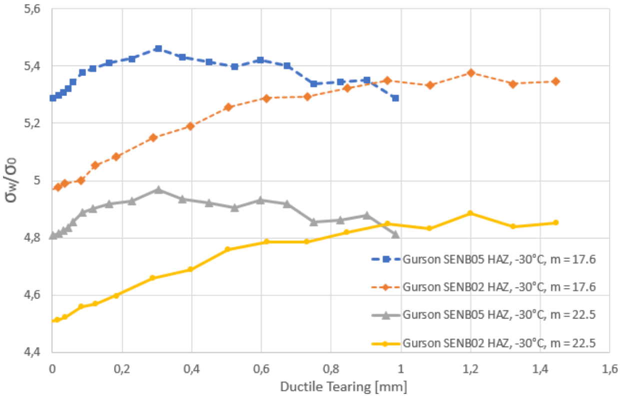

Figure 6.25: Ductile tearing effects. Normalised Weibull stress vs ductile tearing

As exhibited in **Figure 6.25**, the resulting Weibull stress increases accordingly as the Weibull modulus is decreased. Thus, the Weibull modulus shift will moderately affect the Weibull stress ratio between the two specimens even though the Weibull stress trends are not particularly affected. Hence, there should exist a Weibull modulus which can accurately constraint-correct the two fracture geometries. Nevertheless, as the stress field experiences notable changes throughout the transition region, the resulting Weibull parameters might change with temperature even though the flaw distribution a priori should remain relatively constant when identical weld simulation and heat treatment are assumed.

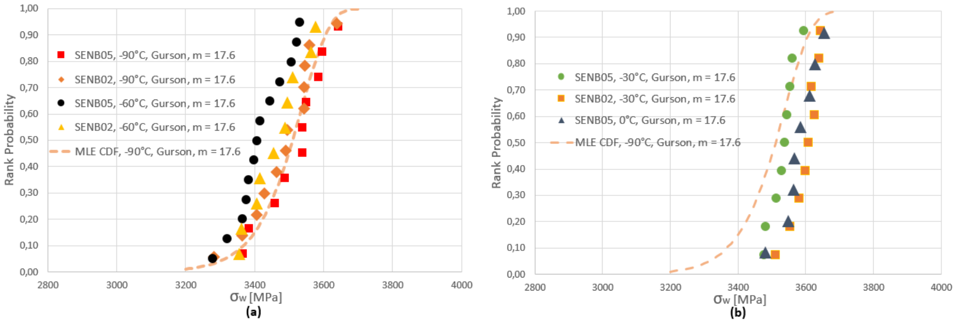

Figure 6.26: Constraint-correction with constant Weibull modulus
(a) -90°C and -60°C, (b) -30°C and 0°C

Figure 6.26 (a) and (b) respectively illustrate the critical Weibull stresses in the assumed brittle and transition regions from the SENB05 and SENB02 test series. As exhibited in **Figure 6.26 (a)**, the maximum likelihood estimated distribution function at -90°C is able to describe the experimental Weibull stresses. However, the SENB05 fracture series at -60°C deviates from the other distributions between 30-80% probability of failure. The same deviating population also prevails in the initial fracture toughness analysis in Section 6.2 and in the Weibull parameter study in Section 6.2.1 which in turn means that the fracture mechanics test series does not follow the two-parameter Weibull distribution. Nonetheless, the concave trend can usually be solved by introducing a third Weibull parameter, but since only the mid population deviates from the two-parameter Weibull distribution, the deviating Weibull stress population is presumably due to experimental errors or flawed weld simulation causing heterogeneous microstructure.

By considering temperature independent Weibull parameters, the resulting CDF at -90°C in **Figure 6.26 (a)** can accurately constraint-correct the two fracture geometries at -90°C and -60°C without any particular Weibull parameter changes. However, the estimated CDF in **Figure 6.26 (b)** is unable to capture the lower fracture points as the lower bound confidence interval does not increase accordingly in the transition region. Nevertheless, the upper bound confidence interval can account for the applicable transition with increasing temperature. Thus, the Beremin-Gurson approach with temperature independent Weibull parameters can constraint-correct the fracture geometries in the brittle region and to some extent in the transition region. It is nonetheless unable to capture the lower bound transition trend which might be due to the low mesh resolution, inconsistent Weibull stress calculation in LINKpfat or temperature dependent Weibull parameters.

6.4.2 Temperature Dependent Weibull Parameter Study

The Beremin-Gurson model with temperature independent Weibull parameters is unable to describe the shifting Weibull stresses in the transition region. Thus, a more comprehensive Weibull parameter study is conducted to determine the temperature dependence of the constitutive Weibull parameters. As exhibited in **Figure 6.27 (a)**, all the CDFs follow the same distribution trend which is evidence of a constant Weibull modulus in the brittle region as it defines the flaw distribution and the slope of the Weibull cumulative distribution function. However, the transition region CDFs illustrated in **Figure 6.27 (b)** exhibit a slightly steeper distribution trend. Thus, the Weibull modulus is evidently increasing when entering the transition region as larger Weibull modulus promotes steeper Weibull cumulative distribution functions.

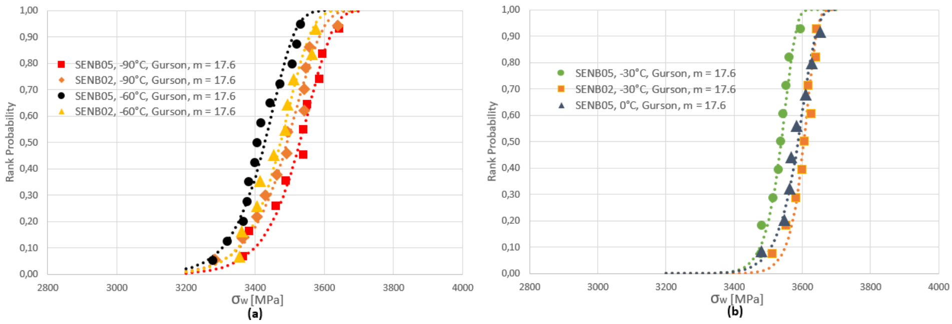

Figure 6.27: Failure probability vs Weibull stress calculated with the Beremin-Gurson model MLE CDFs as stippled lines. (a) -90°C and -60°C, (b) -30°C and 0°C

$$P_F(\sigma_w) = 1 - exp\Big[-\Big(\frac{\sigma_w}{\sigma_u}\Big)^m\Big] \tag{6.5}$$

The Weibull modulus, m in Equation 6.5 characterises the flaw distribution of second-phase particles and defects which may yield cleavage fracture initiation as described in Section 2.3. The likelihood of changing the flaw distribution in the microstructure just by increasing the temperature is not the most probable scenario when equal heat treatment and weld simulation are assumed. However, the scale parameter, σ_u might change accordingly as the dislocation movement changes with temperature. σ_u as a temperature dependent parameter may describe the changing stress state, material flow properties, and Weibull stress throughout the ductile-to-brittle transition. The scale parameter characterises the steel's resistance to cleavage fracture which in turn means large σ_u is equivalent with higher resistance to cleavage fracture. However, the σ_u temperature dependence becomes quite ambiguous as the brittle crack initiation barriers change from second-phase particles and defects at low temperatures to grain boundaries at high temperatures. Hence, there might exist a non-unique Weibull parameter set as the material might exhibit changes in the defect population with shifting temperature.

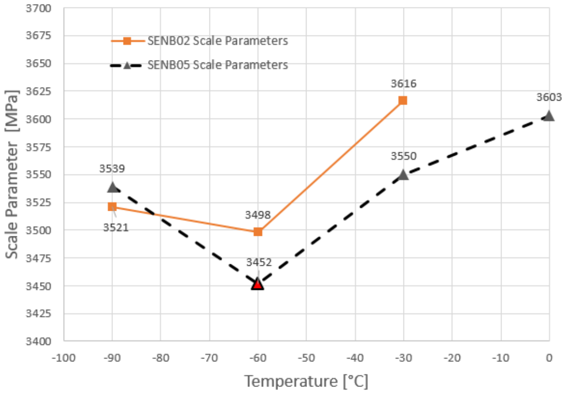

Figure 6.28: Scale parameter DBT. Temperature independent Weibull modulus, $m = 17.6$ SENB05 at -60°C marked as red due to deviating Weibull stress population

The constitutive scale parameter, σ_u can from the CDFs in **Figure 6.27** readily be defined as the Weibull stress yielding $P_F = 1 - e^{-1} = 0.632$, and **Figure 6.28** exhibits all the scale parameters from the SENB02 and SENB05 CDFs as a function of temperature. The SENB02 scale parameter remains relatively constant in the brittle region and increases when entering the transition region, and the SENB05 scale parameter decreases in the brittle region before it increases in the transition region. The scale parameters almost coincide at -90°C which is reasonable as the Weibull parameters are fitted at this temperature. However, the scale parameter deviates moderately at -60°C even though most of the rank probabilities with corresponding Weibull stresses coincide at this temperature which in turn is due to the deviating Weibull stress population as shown in **Figure 6.27**. On the assumption the SENB05 series at -60°C follows a projected two-parameter Weibull distribution, the resulting SENB05 scale parameter would decrease at the same rate as SENB02.

Thus, the scale parameter remains somewhat constant in the brittle region and increases with increasing temperature in the transition region. Nevertheless, it is worth noticing the scale parameters do not change more than 1.8% between -90$^\circ C$ and 0$^\circ C$ for SENB05, and 2,7$\%$ between -90$^\circ C$ and -30$^\circ C$ for SENB02 which is slightly diminishing. The resulting resistance to cleavage fracture will thus increase with increasing temperature by assuming constant flaw distribution (m = constant) which is reasonable as the material is less likely to yield cleavage fracture at high temperatures.

The Beremin-Gurson model is unable to constraint-correct the two fracture geometries at high temperatures by assuming constant flaw distribution which in turn means the Weibull modulus may change with shifting temperature. The constitutive critical Weibull stresses from the two fracture geometries are thus toughness scaled respectively at all the test temperatures to find the best Weibull modulus estimates throughout the DBT. As exhibited in **Figure 6.29 (a)**, the best toughness scaling prevails at m = 17 for the critical Weibull stresses at -90$^\circ C$, m = 22.5 at -60$^\circ C$, and m = 25 at -30$^\circ C$. The corresponding scale parameter changes accordingly as larger Weibull modulus yield smaller scale parameters at the respective temperatures.

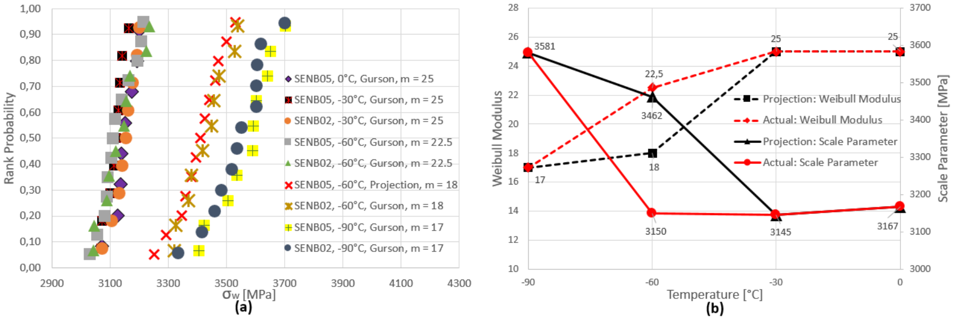

Figure 6.29: Temperature dependent Weibull parameters fitted at all the test temperatures (a) Toughness scaling, (b) m and σ_u temperature trends

As exhibited in **Figure 6.29 (b)**, the same temperature trend prevails as a small Weibull modulus yields a large scale parameter and vice versa. The Weibull modulus increases with increasing temperature which in turn means the flaw distribution increases and the Weibull CDF becomes steeper. The temperature trend is somewhat reasonable as the critical Weibull stresses become somewhat constant during ductile tearing which in turn promotes steep CDFs in the transition region. However, the Weibull modulus at -90$^\circ C$ and -60$^\circ C$ deviate considerably even though the SENB05 specimens are in the brittle region without any significant ductile damage. As some of the SENB02 specimens experience ductile tearing prior to cleavage at -60$^\circ C$, the Weibull modulus must be changed accordingly in order to constraint-correct the different stress states. Also, SENB05 at -60$^\circ C$ constitute a deviating Weibull stress population which does not follow the two-parameter Weibull distribution (see **Figure 6.27**) and might also bias the toughness scaling and the resulting Weibull modulus at -60$^\circ C$. Thus, a projection of the two-parameter Weibull distribution function is established for SENB05 at -60$^\circ C$ in order to further investigate the Weibull parameter temperature trends. As shown in **Figure 6.29 (a)**, the best toughness scaling of the projected distribution prevails at m = 18 which in turn largely affects the scale parameter as exhibited in **Figure 6.29 (b)**.

By considering the bias-corrected Weibull modulus at -60°C and the Weibull parameter trends in **Figure 6.29**, the Weibull modulus is seemingly increasing when entering the transition region and remains relatively constant throughout the transition region. However, the same trends prevail at different magnitudes when considering the temperature dependent Weibull modulus and scale parameter independently. The scale parameter decreases from -90°C to -60°C in both the analyses due to the inconsistent SENB05 Weibull stress population and moderately increases throughout the transition region with somewhat constant Weibull modulus. The decreasing scale parameter trend from -90°C to -60°C is also due to the different stress states of the two fracture geometries where the SENB02 specimens are in the lower transition region, and the SENB05 specimens are still in the brittle region at -60°C. The projected parameter trends in **Figure 6.29 (b)** demonstrate somewhat constant Weibull parameters in the brittle region which is expected as the material behaviour is rather consistent. However, the Weibull modulus increases as the specimens enter the transition region where the scale parameter decreases accordingly. Both parameters remain relatively constant throughout the transition region, and the projected Weibull modulus trend is the opposite of the scale parameter trend as larger Weibull modulus yields smaller scale parameter and vice versa. Thus, the parameter temperature trends in **Figure 6.29 (b)** are quite distinctive as they remain relatively constant in both the brittle region and the transition region where the parameters exhibit a brittle-to-transition shift.

6.4.3 Final Beremin-Gurson Model: DBT

The Beremin-Gurson model with temperature independent Weibull parameters is able to constraint-correct SENB02 and SENB05 in the brittle region and demonstrates relatively constant Weibull parameters at -90°C and -60°C. The temperature independent Weibull parameters are unable to describe the lower bound confidence intervals accurately in the transition region and do not constraint-correct the fracture geometries properly at -30°C (1.86% deviation). The Beremin-Gurson model is nonetheless able to describe the upper bound limit of the fractured specimens throughout the ductile-to-brittle transition from -90°C to 0°C.

A temperature dependent Weibull parameter study is thus conducted as the temperature independent Weibull parameters are unable to constraint-correct the two fracture geometries in the transition region. The parameter study discloses rather conclusive temperature dependent Weibull parameter trends when toughness scaling the fracture data at the respective test temperatures. The Weibull modulus is relatively constant in the brittle region and increases accordingly as the fracture test series enter the transition region. The resulting Weibull parameters are then utilised to establish Weibull cumulative distribution functions by maximum likelihood estimation in Matlab (see Appendix B.1). As exhibited in **Figure 6.30**, the constitutive MLE CDFs are used to establish confidence intervals at all the test temperatures in order to examine the applicability of the temperature dependent Weibull parameters to concurrently constraint-correct the fracture geometries and predict the appropriate fracture toughness values throughout the ductile-to-brittle transition. The MLE confidence intervals in **Figure 6.30 (b)** can describe the whole ductile-to-brittle transition within a [10%, 90%] confidence interval which is expected as all the fracture test series follow the two-parameter Weibull distribution and are toughness scaled accordingly.

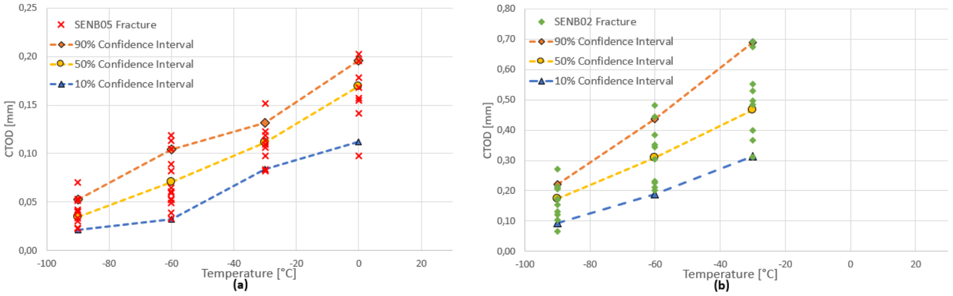

Figure 6.30: DBT with MLE confidence intervals. Temperature dependent Weibull parameters (a) SENB05, (b) SENB02

However, the SENB05 confidence intervals in **Figure 6.30 (a)** follow a somewhat volatile trend due to the inconclusive fracture mechanics test series at -60°C which comprises several fracture specimens deviating from the two-parameter Weibull distribution as frequently discussed in Chapter 6. The insufficient fracture mechanics data at -60°C is presumably due to experimental errors or flawed weld simulation. The MLE confidence intervals are nevertheless able to describe the ductile-to-brittle transition from -90°C to 0°C which in turn means the constitutive Weibull parameters can describe the transition at 0°C accurately without toughness scaling. Nonetheless, the lower 5% confidence interval at 0°C is somewhat overestimating the steel's brittleness as the lowest fracture point largely biases the MLE CDF. In conclusion, the Beremin-Gurson model with temperature independent parameters can describe the fracture toughness scatter in the brittle region but are only to some extent able to describe the fracture toughness values in the transition region as the lower bound limit overestimates the steel's brittleness. However, the Beremin-Gurson model with temperature dependent Weibull parameters can constraint-correct fracture geometries and demonstrate the ductile-to-brittle transition accurately. The constitutive Weibull parameters are seemingly following distinctive temperature trends as the specimens leave the brittle region and enter the transition region.

6.4.4 Discussion: The Beremin-Gurson Model

The current Beremin-Gurson model comprises two separate material characterisation models and is developed to among other things reduce the required laboratory work needed to describe the ductile-to-brittle transition of structural steels. The simulation scheme must constitute precise fracture toughness characterisations at a low-cost level with low time consumption and must be able to describe both ductile and brittle material characteristics. The constitutive models are also required to describe the appropriate fracture toughness values for bi-modal grain size distributed steels throughout the ductile-to-brittle transition, and should ideally only need fracture mechanics testing at one temperature in the brittle region and one temperature in the ductile region. Keeping the scope and objective in mind when evaluating the combined Beremin-Gurson model features several challenges and controversial aspects. The models are first assessed separately before reviewing the combined simulation model since the Beremin model as a post-processing routine is conducted independently of the Gurson model.

The Complete Gurson Model is able to describe the crack growth and material softening throughout the DBT by fitting the simulated resistance curve to the experimental results in the solely ductile region. Only the true plastic flow curves are temperature dependent material parameters, and f_0, f_c, and n are temperature independent parameters. f_0 is a material dependent parameter fitted in the ductile region and determines the slope of the resistance curve where smaller initial void volume fractions yield steeper resistance curves and vice versa. The temperature independent initial void volume fraction is not unconditionally able to simulate the correct resistance curve slope of the low constraint geometry which in turn means the current nucleation model might be biased when simulating several constraint levels with somewhat different mesh even though the size of the smallest elements are the same. The initial void volume fraction, f_0 as a temperature independent parameter is also questionable as the void growth and void coalescence are temperature dependent in the current simulation scheme. The Gurson model depends considerably on the mesh element size as each element comprises a void which in turn is treated as a nucleation site. The length scale of the mesh elements, l_c represents the size of the cracked segments and the direction of the crack propagation and controls the integration points of the crack extension. The length scale is reduced to $0.05mm$ in order to get a better resolution of the plastic blunting and the principal stresses ahead of the crack tip. The attempt fails as the Gurson user subroutine is unable to achieve convergence between the time increments with mesh element size 0.05x0.05mm^2. The underlying Gurson user subroutine must be improved to make it versatile and adaptable in order to establish meshes with any given element size. As each element in the FE-model represents a nucleation site for the void-induced damage model, the element length should ideally be equal to the average void distance in order to describe the appropriate void distribution. The underlying user subroutine markedly limits the adaptability of The Complete Gurson Model to high-resolution meshes, but the convergence problem is solvable by rewriting the constitutive Gurson UMAT by incorporating adequate material input from the true plastic flow curve. Thus, the most efficient Gurson UMAT comprises thirty-one (31) data points from the Ramberg-Osgood estimated true plastic flow curve, but as the material yields at considerable lower σ_{ys} and σ_{UTS} with increasing temperature, the Ramberg-Osgood estimation procedure may not be accurate when utilising similar true strain data points. Hence, the model may be optimised by either estimating the constitutive material input directly from the experimental true plastic flow curves or by reducing the true strain interval between each data point at higher temperatures.

The Beremin model is able to constraint-correct and describe the fracture toughness in the brittle region but is unable to constraint-correct nor calculate appropriate Weibull stresses in the transition region. The in-house Weibull stress calculation program LINKpfat demonstrates several controversial features as the program is initially designed to calculate fatigue lifetime. The principal stresses in all the elements contribute to the simulated Weibull stress yielding severely biased Weibull stress calculations. The fundamental weakest-link principles in the Beremin model is based on a fracture process zone (FPZ) consisting of only the elements which exceed certain threshold stress usually defined as the yield strength. Thus, the Weibull stress will be markedly biased compared to the original criterion when several elements exhibit intermediate stresses below the threshold limit. The LINKpfat weakest-link limitation is partly solved by sectioning the weld zone and model body separately which in turn will exclude all the Weibull stress contributions in the model body. However, the remaining elements in the weld zone are somewhat biased when considering the original Beremin principles even after the model sectioning are properly conducted. In order to get unbiased Weibull stress calculations, LINKpfat must either be further improved by incorporating a threshold limit characterisation of the fracture process zone or by substituting LINKpfat with another Weibull stress calculation tools such as WSTRESS [121] [124] and Weibull++ [109].

The Beremin-Gurson model is able to constraint-correct different fracture geometries and describe the fracture toughness values throughout the DBT when considering temperature dependent Weibull parameters where the mean least square method is used to calibrate the representative Weibull modulus in the brittle region by only considering one constraint level. Nevertheless, the constitutive calibration methods are somewhat biased by the Weibull stress calculations in LINKpfat which in turn leads to large Weibull parameter confidence intervals. The combined model is nevertheless able to simulate both constraint effects and constraint relaxation accurately and to constraint-correct the fracture geometries throughout the DBT. The resulting temperature dependent Weibull parameters can describe the appropriate fracture toughness values, but the relatively low mesh resolution is a priori inadequate to calculate appropriate Weibull stresses. The lower bound confidence interval in the DBT is markedly affected as the stress field must be immensely detailed ahead of the crack tip in order to simulate accurate Weibull stresses during plastic blunting. The current 4-node 2D plane strain elements should ideally be either 8-node 2D elements or 20-node 3D bricks which in turn requires extensive computing power compared to the current FE-model mesh. As the Beremin model is used as a post-processing routine independently of the Gurson simulation, the competing void-induced ductile damage from the Gurson model and the brittle failure probability from the flaw distribution in the Beremin model do not characterise a representative probability of voids. Thus, the Weibull stress calculation should ideally contain a probability of void nucleation factor P_{void} which takes the void nucleation from second-phase particles into account. On the assumption the applicable void is nucleated from a defect, the element which contains the defect will not promote cleavage fracture and hence diminish the Weibull stress contribution of the applicable element by a factor of $(1 - P_{void}), P_{void} \in [0, 1]$. Thus, the competing flaw distribution of defects as cleavage initiation sites and the voids as nucleation sites might contradict the underlying weakest-link principles if there is no common probability factor in the Weibull stress calculation.

The current Weibull calibration procedures constitute several biases as they are highly limited to negligible ductile damage and the size of the fracture dataset at any given temperature. Also, none of the fracture toughness values are censored which in turn may result in markedly biased Weibull parameter estimates. LINKpfat is unable to identify the applicable fracture process zone with corresponding V_p which in turn might yield inconsistent Weibull stress calculations. The material in question follows a two-parameter Weibull distribution, but the current Beremin-Gurson model is not sufficient in case of three-parameter Weibull distributed materials nor bi-modal grain size distributed materials. Even though the model is able to describe the characteristic Weibull parameter DBTs, it cannot identify the appropriate transition temperature without utilising competing ductility criteria. However, by using the same competing criteria as the Gurson-RKR model in Section 4.3, the SENB05 transition region starts at about -15$°C$ which is reasonable within the 90$\%$ fracture confidence interval. In conclusion, the current Beremin-Gurson model is adequate to describe the ductile-to-brittle transition from -90$°C$ to 0$°C$ but the constitutive Weibull stress computation and several model parameters remain uncertain and questionable.

Chapter 7

Conclusion and Future Work

Conclusion

The master's thesis discloses the Gurson-RKR and Beremin-Gurson models in order to describe the ductile-to-brittle transition (DBT) of structural steels by considering experimental results from uniaxial tensile tests and two different single edged notched three-point bending (SENB) specimens ($\frac{a}{W}$ equal to 0.2 and 0.5) conducted from -90$^\circ C$ to 21$^\circ C$. The Gurson-RKR model is established in a preliminary study and is thus separately discussed and evaluated in Section 4.4.1. The Gurson-RKR model is able to visualise and describe the DBT regions by utilising the RKR Criterion as a post-processing routine to predict cleavage fracture initiation, and The Complete Gurson Model to describe ductile mechanisms and void-induced material damage. The Beremin-Gurson model is unlike the distance-based Gurson-RKR model based on statistically independent volume elements where the Beremin model is used as a post-processing routine by considering principal stresses in the volume elements ahead of the crack tip. A separate discussion of the combined Beremin-Gurson model are described in Section 6.4.4, and only the concluding arguments and future work is presented in this section.

The fracture toughness values from all the fracture mechanics tests of both fracture geometries follow a two-parameter Weibull distribution. The experimental fracture toughness values are ranked in ascending order of mean rank probabilities as a function of fracture toughness which in turn fit the maximum likelihood estimated (MLE) two-parameter Weibull cumulative distribution functions (CDF) at all temperatures. The SENB02 and SENB05 specimens are both in the brittle region at -90$^\circ C$ and just the SENB05 specimens are unambiguously in the brittle region at -60$^\circ C$. The scale parameter which describes the resistance to cleavage fracture increases with increasing temperature, and the shape parameter which represents the failure rate is seemingly region dependent as it is constant in the brittle region and shifts to another value in the transition region.

The original Beremin model with temperature independent Weibull parameters is unable to compute appropriate Weibull stresses in the transition region but can constraint-correct the fracture geometries in the brittle region. The model is able to describe the distinctive ductile-to-brittle transition with temperature independent Weibull parameters for the individual specimens but cannot constraint-correct them in the transition region. The Weibull parameters is fitted at the lowest temperature (-90$^\circ C$) where the specimen is assumed to be in the brittle region with negligible ductile damage which in turn makes the flaw distribution unbiased. The original Beremin model overestimates the steel's brittleness in the transition region as it computes high Weibull stresses and no crack extension nor constraint effects. The mean least square linear regression and maximum likelihood estimation methods are unable to calibrate the Weibull modulus at -90$°C$ by just considering one fracture geometry, and only the toughness scaling method can estimate an appropriate Weibull modulus with a fracture dataset comprising ten fracture specimens.

The Complete Gurson Model with temperature independent Gurson parameters and temperature dependent true plastic flow curves is fitted to the experimental resistance curve at the highest temperature ($21°C$) in the ductile region with solely ductile characteristics. The model is able to simulate perfect resistance curves for the whole ductile-to-brittle transition for the high constraint specimens ranging from -90$°C$ to $21°C$ when assuming constant plastic blunting rate prior to ductile tearing initiation. Both the experimental and simulated resistance curves follow the same linear trend function during ductile tearing regardless of temperature. The low constraint specimen (SENB02) has a steeper resistance curve and larger blunting zone than the high constraint specimen (SENB05), but the Gurson model is unable to simulate the appropriate resistance curve slope of the low constraint specimen when assuming geometry independent Gurson parameters.

The Beremin-Gurson model combines The Complete Gurson Model to describe the appropriate ductile mechanisms and crack extension, and the Weibull-based Beremin model as a post-processing routine to compute the probability of brittle failure throughout the ductile-to-brittle transition. The whole simulation scheme is based on determining material properties from uniaxial tensile tests, conducting and reviewing fracture mechanics tests, developing ABAQUS models with Gurson user-defined materials (UMAT) constituting Gurson parameters and true plastic flow curves, and calibrating Weibull parameters by considering rank probabilities and Weibull stresses. Both the mean least square (LSQ) linear regression method and the maximum likelihood estimation (MLE) method can calibrate appropriate Weibull modulus estimates at -90$°C$. The LSQ estimate is able to constraint-correct the fracture geometries at -90$°C$, but the LINKpfat FE-model must be separately sectioned with weld zone and model body in order to get accurate Weibull stress calculations and proper constraint effects. LINKpfat calculates the Weibull stress from all the elements in the model and somewhat contradicts the weakest-link principles in the Beremin model. The Beremin-Gurson model can describe appropriate constraint effects and constraint relaxation at the respective temperatures but the temperature independent Weibull parameters fitted at -90$°C$ is unable to describe the ductile-to-brittle transition. The temperature independent Weibull parameters can constraint-correct the fracture geometries in the brittle region and describe the upper limit transition from -90$°C$ to $0°C$ but the lower limit transition curve overestimates the steel's brittleness. The scale parameter remains constant in the brittle region and increases as the specimens enter the transition region when constant Weibull modulus and flaw distribution are assumed. Thus, temperature dependent Weibull parameters are estimated by toughness scaling the two fracture geometries at all the test temperatures. The Weibull parameters are constant in the brittle region and shifts as the specimens enter the transition region. The Weibull modulus, $m = 17$ in the brittle region and changes to $m = 25$ in the transition region, and the scale parameter is about 3500MPa in the brittle region and about 3150MPa in the transition region. The temperature dependent Weibull parameters can constraint-correct the two fracture geometries throughout the ductile-to-brittle transition which means the underlying criteria can illustrate geometry independent Weibull parameters.

The current Beremin-Gurson model presents several advantages compared to the distance-based preliminary Gurson-RKR model as it can be readily applied in LINKpfat to calculate the Weibull stress by implementing the ABAQUS database file (.odb) directly. The model is also able to constraint-correct fracture geometries and capture the fracture toughness throughout the ductile-to-brittle transition by combining the ductile mechanisms from the Gurson model and the probability of brittle failure calculation from the Beremin model. However, the model parameters and the whole simulation scheme remains uncertain as the LINKpfat program has proven to be highly biased as it somewhat contradicts the constitutive weakest-link principles in the Beremin model. Even though the model fulfils some of the intended objectives such as describing the geometry constraint effects, criteria for application and qualification of steels and extending the application range, the objective of reducing or substituting laboratory work is not unconditionally reached. The model can reduce the required laboratory work to describe the DBT but only if the Weibull parameter temperature dependence trends are concluded as material independent. The current simulation scheme can ease the material characterisation process if the Weibull parameter temperature trends prevail in other materials as only one fracture geometry is necessary in order to calibrate the geometry independent Weibull parameters.

Recommended Future Work

The following list comprises several approaches to further enhance the current Beremin-Gurson model in order to make it more versatile, unbiased and cost-efficient:

- Make the LINKpfat Weibull stress calculation unbiased by incorporating a threshold limit function in order to define the fracture process zone. Establish a script which can extract all the Weibull stresses from all the time increments to make the procedures less time-consuming
- Consider utilising J-integral and Charpy V-notch tests which in turn can lower the laboratory costs in order to get the appropriate and unbiased fracture mechanics data
- Test the Beremin-Gurson model with three constraint levels in order to conclude the geometry independent Weibull parameters and the toughness scaling procedure
- Identify the temperature dependent Weibull parameters from another material by utilising the same simulation scheme in order to conclude the Weibull parameter temperature trends
- Consider bias-correcting the Weibull parameter estimates and censor the fracture toughness values before doing the finite element analyses
- Compare the applicability of the Beremin-Gurson model compared to the standard master curve approach and the SINTAP procedure
- Conduct a temperature dependence study and examine the constraint effects of the constitutive Gurson parameters in order to conclude them as geometry and temperature independent parameters

Bibliography

[1] O. Akselsen, Ø. Grong, and J. Solberg. Structure–property relationships in intercritical heat affected zone of low-carbon microalloyed steels. *Materials science and technology*, 3(8):649–655, 1987.

[2] O. Akselsen, J. Solberg, and O. Grong. Effects of martensite-austenite (ma) islands on intercritical heat-affected zone toughness of low-carbon microalloyed steels. *Scandinavian journal of metallurgy*, 17(5):194–200, 1988.

[3] R. Ale, J. Rebello, and J. Charlier. A metallographic technique for detecting martensite-austenite constituents in the weld heat-affected zone of a micro-alloyed steel. *Materials characterization*, 37(2-3):89–93, 1996.

[4] T. L. Anderson. *Fracture mechanics: Fundamentals and Applications*, volume 3. Taylor Francis, Boca Raton, Fla, 2005.

[5] T. L. Anderson, D. Stienstra, and R. H. Dodds. A theoretical framework for addressing fracture in the ductile-brittle transition region. In *Fracture mechanics: twenty-fourth volume*. ASTM International, 1994.

[6] A. Andrieu, A. Pineau, J. Besson, D. Ryckelynck, and O. Bouaziz. Bimodal beremin-type model for brittle fracture of inhomogeneous ferritic steels: Theory and applications. *Engineering Fracture Mechanics*, 95:84–101, 2012.

[7] S. D. Antolovich, A. Saxena, and G. Chanani. Increased fracture toughness in a 300 grade maraging steel as a result of thermal cycling. *Metallurgical Transactions*, 5(3):623–632, 1974.

[8] Apos, N. Dowd, and C. Shih. Family of crack-tip fields characterized by a triaxiality parameter. part i. structure of fields. *Journal of the Mechanics and Physics of Solids*, 39(8):989–1015, 1991.

[9] Apos, N. Dowd, and C. Shih. Family of crack-tip fields characterized by a triaxiality parameter. part ii. fracture applications. *Journal of the Mechanics and Physics of Solids*, 40(5):939–963, 1992.

[10] A. Argon, J. Im, and R. Safoglu. Cavity formation from inclusions in ductile fracture. 6(4):825–837, April 1975.

[11] ASTM. Standard test method for determination of reference temperature, t0, for ferritic steels in the transition range. *Annual Book of ASTM Standards*, 3:1068–1084, 1921.

[12] ASTM. Standard test method for crack-tip opening displacement (ctod) fracture toughness measurement. ASTM E 1290, 2008.

[13] H. Azizi-Alizamini, M. Militzer, and W. Poole. A novel technique for developing bimodal grain size distributions in low carbon steels. *Scripta Materialia*, 57(12):1065–1068, 2007.

[14] T. Becker Jr, R. Cannon, and R. O. Ritchie. A statistical rkr fracture model for the brittle fracture of functionally graded materials. In *Materials science forum*, volume 308, pages 957–962. Trans Tech Publ, 1999.

[15] A. Benzerga. Micromechanics of coalescence in ductile fracture. *Journal of the Mechanics and Physics of Solids*, 50(6):1331–1362, 2002.

[16] A. Benzerga and J.-B. Leblond. Ductile fracture of void growth to coalescence. *Adv. Appl. Mech.*, 44:169–305, 2010.

[17] F. Beremin. Cavity formation from inclusions in ductile fracture of a508 steel. *Metallurgical Transactions A*, 12(5):723–731, May 1981.

[18] F. Beremin, A. Pineau, F. Mudry, J.-C. Devaux, Y. D'Escatha, and P. Ledermann. A local criterion for cleavage fracture of a nuclear pressure vessel steel. *Metallurgical Transactions A*, 14(11):2277–2287, November 1983.

[19] J. Besson. Continuum models of ductile fracture: A review. *International Journal of Damage Mechanics*, 19(1):3–52, January 2010.

[20] J. Besson, C. McCowan, and E. Drexler. Modeling flat to slant fracture transition using the computational cell methodology. *Engineering Fracture Mechanics*, 104:80–95, 2013.

[21] C. Betegon and J. Hancock. Two-parameter characterization of elastic-plastic crack-tip fields. *Journal of Applied Mechanics, Transactions ASME*, 58(1):104–110, March 1991.

[22] H. Bhadeshia and R. Honeycombe. *Steels: Microstructure and Properties*. Elsevier Science, Amsterdam, 3rd edition, 2006.

[23] B. Bilby, I. Howard, and Z. Li. Mesh independent cell models for continuum damage theory. *Fatigue & Fracture of Engineering Materials & Structures*, 17(10):1221–1233, 1994.

[24] N. Bonora, D. Gentile, A. Pirondi, and G. Newaz. Ductile damage evolution under triaxial state of stress: theory and experiments. 21(5):981–1007, 2005.

[25] S. Bordet, A. Karstensen, D. Knowles, and C. Wiesner. A new statistical local criterion for cleavage fracture in steel. part i: model presentation. *Engineering fracture mechanics*, 72(3):435–452, 2005.

[26] W. Brocks, J. Besson, O. Chabanet, I. Scheider, and D. Steglich. Modeling of crack growth in sheet metal. *Zeitschrift Fur Angewandte Mathematik Und Mechanik*, 81:133–136, 2001.

[27] W. Brocks and W. Schmitt. Quantitative assessment of the role of crack tip constraint on ductile tearing. Number 1171, pages 64–78. Publ by ASTM, 1993.

[28] F. Bron and J. Besson. Simulation of the ductile tearing for two grades of 2024 aluminum alloy thin sheets. *Engineering Fracture Mechanics*, 73(11):1531–1552, 2006.

[29] F. Bron, J. Besson, and A. Pineau. Ductile rupture in thin sheets of two grades of 2024 aluminum alloy. *Materials Science Engineering A*, 380(1):356–364, 2004.

[30] BSI. Guide to methods for assessing the acceptability of flaws in metallic structures. *British Standards Institution*, BS 7910, 2005.

[31] D. Chakrabarti, M. Strangwood, and C. Davis. Effect of bimodal grain size distribution on scatter in toughness. *Metallurgical and Materials Transactions A*, 40(4):780–795, 2009.

[32] C. X. Chen, W. S. Li, and H. F. Peng. Investigation on ma constituent in weld cghaz of high-strength microalloyed steel. In *Materials Science Forum*, volume 575, pages 690–695. Trans Tech Publ, 2008.

[33] J. Chen and R. Cao. *Micromechanism of Cleavage Fracture of Metals : A Comprehensive Microphysical Model for Cleavage Cracking in Metals*. Micromechanism of Cleavage Fracture of Metals. Elsevier Science, Burlington, 2014.

[34] J. Chen, Y. Kikuta, T. Araki, M. Yoneda, and Y. Matsuda. Micro-fracture behaviour induced by ma constituent (island martensite) in simulated welding heat affected zone of ht80 high strength low alloyed steel. *Acta Metallurgica*, 32(10):1779–1788, 1984.

[35] A. Cottrell. Theoretical aspects of fracture. pages 20–53, 1959.

[36] T. Cox and J. Low. An investigation of the plastic fracture of aisi 4340 and 18 nickel-200 grade maraging steels. *Metallurgical Transactions*, 5(6):1457–1470, June 1974.

[37] D. A. Curry and J. F. Knott. Effects of microstructure on cleavage fracture stress in steel. *Metal Science*, 12(11):511–514, 1978.

[38] C. Davis and J. King. Cleavage initiation in the intercritically reheated coarse-grained heat-affected zone: Part i. fractographic evidence. *Metallurgical and materials transactions A*, 25(3):563–573, 1994.

[39] R. M. Denys. Wide-plate testing of weldments: Part ii–wide-plate evaluation of notch toughness. In *Fatigue and Fracture Testing of Weldments*. ASTM International, 1990.

[40] R. H. Dodds, T. L. Anderson, and M. T. Kirk. A framework to correlate a/w ratio effects on elastic-plastic fracture toughness (j c). *International Journal of Fracture*, 48(1):1–22, 1991.

[41] P. Eikrem, Z. Zhang, E. Østby, and B. Nyhus. Numerical study on the effect of prestrain history on ductile fracture resistance by using the complete gurson model. *Engineering Fracture Mechanics*, 75(15):4568–4582, 2008.

[42] J. Elmer and J. Wong. Welding science-a new look at a fundamental technology. *Lawrence Livermore National Laborat01y/Science & Technology Review*, 79(4):1–11, 2001.

[43] D. Fairchild. Fracture toughness testing of weld heat-affected zones in structural steel. In *Fatigue and Fracture Testing of Weldments*. ASTM International, 1990.

[44] A. Fjeldstad. *Modelling of fatigue crack growth at notches and other stress raisers*, volume 231. Norwegian University of Science and Technology, Faculty of Engineering Science and Technology, Department of Engineering Design and Materials, Trondheim, 2007.

[45] J. Fothergill. Estimating the cumulative probability of failure data points to be plotted on weibull and other probability paper. *IEEE transactions on electrical insulation*, 25(3):489–492, 1990.

[46] X. Gao, J. Faleskog, and C. F. Shih. Analysis of ductile to cleavage transition in part-through cracks using a cell model incorporating statistics. *Fatigue and Fracture of Engineering Materials and Structures*, 22(3):239–250, 1999.

[47] X. Gao, C. Ruggieri, and R. Dodds. Calibration of weibull stress parameters using fracture toughness data. *International Journal of Fracture*, 92(2):175–200, 1998.

[48] W. Garrison and N. Moody. Ductile fracture. *Journal of Physics and Chemistry of Solids*, 48(11):1035–1074, 1987.

[49] D. L. Gautier, K. J. Bird, R. R. Charpentier, A. Grantz, D. W. Houseknecht, T. R. Klett, T. E. Moore, J. K. Pitman, C. J. Schenk, J. H. Schuenemeyer, K. Sørensen, M. E. Tennyson, Z. C. Valin, and C. J. Wandrey. Assessment of undiscovered oil and gas in the arctic. *Science (New York, N.Y.)*, 324(5931), May 2009.

[50] M. Gologanu, J.-B. Leblond, G. Perrin, and J. Devaux. Theoretical models for void coalescence in porous ductile solids. i. coalescence ”in layers”. *International Journal of Solids and Structures*, 38(32):5581–5594, 2001.

[51] S. Goods and L. Brown. Overview no. 1: The nucleation of cavities by plastic deformation. *Acta Metallurgica*, 27(1):1–15, 1979.

[52] G.R.Irwin. Analysis of stresses and strains near the end of a crack traversing a plate. A-187:229–260, 1946.

[53] A. Gurson. Continuum theory of ductile rupture by void nucleation and growth: Part 1 - yield criteria and flow rules for porous ductile media. *Journal of Engineering Materials and Technology, Transactions of the ASME*, 99(1):2–15, January 1977.

[54] G. T. Hahn. The influence of microstructure on brittle fracture toughness. *Metallurgical and Materials Transactions A*, 15(6):947–959, June 1984.

[55] T. Hanamura, F. Yin, and K. Nagai. Ductile-brittle transition temperature of ultrafine ferrite/cementite microstructure in a low carbon steel controlled by effective grain size. *ISIJ international*, 44(3):610–617, 2004.

[56] J. Hancock and A. Mackenzie. On the mechanisms of ductile failure in high-strength steels subjected to multi-axial stress-states. *Journal of the Mechanics and Physics of Solids*, 24(2-3):147–160, 1976.

[57] J. W. Hancock, W. G. Reuter, and D. M. Parks. Constraint and toughness parameterized by t. In *Constraint effects in fracture*. ASTM International, 1993.

[58] V. Hardenacke, J. Hohe, V. Friedmann, and D. Siegele. Enhancement of local approach models for assessment of cleavage fracture considering micromechanical aspects. In *19th European Conference on Fracture: Fracture Mechanics for Durability, Reliability and Safety, ECF 2012*, 2012.

[59] M. Hauge, H. G. Holm, et al. Statistical interpretation of fracture toughness test data for qualification of weldability and integrity assessment of arctic structures. In *The Twenty-first International Offshore and Polar Engineering Conference*. International Society of Offshore and Polar Engineers, 2011.

[60] R. W. Hertzberg. *Deformation and fracture mechanics of engineering materials*. Wiley, New York, 4th edition, 1996.

[61] H.M.Westergaard. Bearing pressures and cracks. *Journal of Applied Mechanics*, 6:49–53, 1939.

[62] E. Hornbogen and K. Friedrich. On the use of partial properties to interpret the bulk crack propagation behaviour of coarse two-phase materials. *Journal of Materials Science*, 15(9):2175–2182, 1980.

[63] G. Hütter. *Multi-scale simulation of crack propagation in the ductile-brittle transition region*. Technische Universitaet Bergakademie Freiberg Universitaetsbibliothek ”Georgius Agricola”, 2013.

[64] G. Hütter, T. Linse, U. Mühlich, and M. Kuna. Simulation of ductile crack initiation and propagation by means of a non-local gurson-model. *International Journal of Solids and Structures*, 50(5):662–671, 2013.

[65] H. Ikawa, H. Oshige, and T. Tanoue. Effect of martensite-austenite constituent on haz toughness of a high strength steel. *Transactions of the Japan Welding society*, 11(2):87–96, 1980.

[66] S. Jiang and D. Kececioglu. Graphical representation of two mixed-weibull distributions. *IEEE Transactions on Reliability*, 41(2):241–247, 1992.

[67] R. Kabir, A. Cornec, and W. Brocks. Simulation of quasi-brittle fracture of lamellar [gamma]tial using the cohesive model and a stochastic approach. *Computational Materials Science*, 39(1), March 2007.

[68] D. B. Kececioglu and W. Wang. Parameter estimation for mixed-weibull distribution. In *Reliability and Maintainability Symposium, 1998. Proceedings., Annual*, pages 247–252. IEEE, 1998.

[69] M.-C. Kim, Y. J. Oh, and J. H. Hong. Characterization of boundaries and determination of effective grain size in mn-mo-ni low alloy steel from the view of misorientation. *Scripta materialia*, 43(3):205–211, 2000.

[70] M. T. Kirk and R. H. Dodds. J and ctod estimation equations for shallow cracks in single edge notch bend specimens. *Journal of Testing and Evaluation*, 21(4):228–238, 1993.

[71] O. Knoll. *A Probabilistic Approach in Failure Modelling of Aluminium High Pressure Die-Castings*, volume 137. Norwegian University of Science and Technology, Faculty of Engineering Science and Technology, Department of Structural Engineering, Trondheim, 2015.

[72] J. F. Knott. Local approach concepts and the microstructures of steels. *Engineering Fracture Mechanics*, 75(11):3560–3569, 2008.

[73] R. W. Koers, A. H. Krom, and A. Bakker. Prediction of cleavage fracture in the brittle to ductile transition region of a ferritic steel. In *Constraint Effects in Fracture Theory and Applicatons: Second Volume*. ASTM International, 1995.

[74] A. Lambert-Perlade, A.-F. Gourgues, J. Besson, T. Sturel, and A. Pineau. Mechanisms and modeling of cleavage fracture in simulated heat-affected zone microstructures of a high-strength low alloy steel. *Metallurgical and Materials Transactions A*, 35(13):1039–1053, 2004.

[75] S. Lee, B. Kim, and D. Lee. Fracture mechanism in coarse grained haz of hsla steel welds. *Scripta metallurgica*, 23(6):995–1000, 1989.

[76] P. Leevers and J. Radon. Inherent stress biaxiality in various fracture specimen geometries. *International Journal of Fracture*, 19(4):311–325, 1982.

[77] L. Leng. Ordinary least square regression, orthogonal regression, geometric mean regression and their applications in aerosol science. *Journal of Physics: Conference Series*, 78(1), July 2007.

[78] Y. Li and T. Baker. Effect of morphology of martensite–austenite phase on fracture of weld heat affected zone in vanadium and niobium microalloyed steels. *Materials Science and Technology*, 26(9):1029–1040, 2010.

[79] J. Liao, K. Ikeuchi, and F. Matsuda. Toughness investigation on simulated weld hazs of sqv-2a pressure vessel steel. *Nuclear Engineering and Design*, 183(1-2):9–20, 1998.

[80] T. Lin, A. Evans, and R. Ritchie. Statistical analysis of cleavage fracture ahead of sharp cracks and rounded notches. *Acta Metallurgica*, 34(11):2205–2216, 1986.

[81] T. Lin, A. Evans, and R. Ritchie. Stochastic modeling of the independent roles of particle size and grain size in transgranular cleavage fracture. *Metallurgical and Materials Transactions A*, 18(4):641–651, 1987.

[82] T. Lindley, G. Oates, and C. Richards. A critical of carbide cracking mechanisms in ferride/carbide aggregates. *Acta Metallurgica*, 18(11):1127–1136, 1970.

[83] S. Machida, T. Miyata, M. Toyosada, and Y. Hagiwara. Study of methods for ctod testing of weldments. In *Fatigue and fracture testing of weldments*. ASTM International, 1990.

[84] E. Mahgoub, X. Deng, and M. A. Sutton. Three-dimensional stress and deformation fields around flat and slant cracks under remote mode i loading conditions. *Engineering Fracture Mechanics*, 70(18):2527–2542, 2003.

[85] Mathworks. Matlab: Statistics and machine learning toolbox. *mathworks.com/products/statistics*, March 2018.

[86] R. M. McMeeking. Finite deformation analysis of crack-tip opening in elastic-plastic materials and implications for fracture. *Journal of the Mechanics and Physics of Solids*, 25(5):357–381, 1977.

[87] W. Q. Meeker. *Statistical methods for reliability data*. Wiley series in probability and statistics, Applied probability and statistics section. Wiley, New York, 1998.

[88] M.L.Williams. On the stress distribution at the base of a stationary crack. *Journal of Applied Mechanics*, 24:109–114, 1957.

[89] S. Moeinifar, A. Kokabi, and H. M. Hosseini. Influence of peak temperature during simulation and real thermal cycles on microstructure and fracture properties of the reheated zones. *Materials & design*, 31(6):2948–2955, 2010.

[90] T. Morgeneyer and J. Besson. Flat to slant ductile fracture transition: Tomography examination and simulations using shear-controlled void nucleation. *Scripta Materialia*, 65(11):1002–1005, 2011.

[91] T. Morgeneyer, J. Besson, H. Proudhon, M. Starink, and I. Sinclair. Experimental and numerical analysis of toughness anisotropy in aa2139 al-alloy sheet. *Acta Materialia*, 57(13):3902–3915, 2009.

[92] T. F. Morgeneyer, H. Proudhon, and J. Besson. Study of the flat to slant crack transition in ductile thin sheet material : simulations and experiments. *Fracture of materials and structures from micro to macro scale - ECF 18*, 2010.

[93] F. Mudry. A local approach to cleavage fracture. *Nuclear Engineering and design*, 105(1):65–76, 1987.

[94] A. Needleman and V. Tvergaard. An analysis of ductile rupture in notched bars. *Journal of the Mechanics and Physics of Solids*, 32(6):461–490, 1984.

[95] W. Nelson. Applied life data analysis. *Wiley series in probability and mathematical statistics*, pages 313–404, 522–557, 1982.

[96] E. T. Neto and C. Ruggieri. Micromechanics characterization of constraint and ductile tearing effects in small scale yielding fracture. *International journal of solids and structures*, 38(10-13):2171–2187, 2001.

[97] D. Neville and J. Knott. Statistical distributions of toughness and fracture stress for homogeneous and inhomogeneous materials. *Journal of the Mechanics and Physics of Solids*, 34(3):243–291, 1986.

[98] J. Newman, J. Crews, C. Bigelow, and D. Dawicke. Variations of a global constraint factor in cracked bodies under tension and bending loads. Number 1244, pages 21–42, January 1995.

[99] N. O'dowd and C. F. Shih. Family of crack-tip fields characterized by a triaxiality parameterii. fracture applications. *Journal of the Mechanics and Physics of Solids*, 40(5):939–963, 1992.

[100] A. Ohmori, S. Torizuka, and K. Nagai. Strain-hardening due to dispersed cementite for low carbon ultrafine-grained steels. *ISIJ international*, 44(6):1063–1071, 2004.

[101] E. Østby, C. Thaulow, O. Akselsen, et al. Fracture toughness scatter and effect of constraint in weld thermal simulated haz microstructures at-60 c. In *The Twenty-first International Offshore and Polar Engineering Conference*. International Society of Offshore and Polar Engineers, 2011.

[102] E. Østby, C. Thaulow, and B. Nyhus. Constraint effects in weld thermal simulated steel specimens. In *ASME 2008 Pressure Vessels and Piping Conference*, pages 923–932. American Society of Mechanical Engineers, 2008.

[103] T. Pardoen and J. Hutchinson. An extended model for void growth and coalescence. *Journal of the Mechanics and Physics of Solids*, 48(12):2467–2512, 2000.

[104] A. Pineau. Practical application of local approach methods. *Comprehensive Structural Integrity*, 7:177–225, July 2007.

[105] A. Pineau. Modeling ductile to brittle fracture transition in steelsmicromechanical and physical challenges. *International Journal of Fracture*, 150(1-2):129–156, 2008.

[106] A. Pineau, A. Benzerga, and T. Pardoen. Failure of metals i: Brittle and ductile fracture. *Acta Materialia*, 107:424–483, April 2016.

[107] A. Pirondi and N. Bonora. Modeling ductile damage under fully reversed cycling. *Computational Materials Science*, 26:129–141, January 2003.

[108] W. Ramberg and W. Osgood. *Description of stress-strain curves by three parameters*. July 1943.

[109] ReliaSoft. Weibull++ - reliability life data analysis. *reliasoft.com/weibull*.

[110] S. Renevey, S. Carassou, B. Marini, C. Eripret, and A. Pineau. Ductile-brittle transition of ferritic steels modelled by the local approach to fracture. *Le Journal de Physique IV*, 6(C6):C6–343, 1996.

[111] F. Reusch, B. Svendsen, and D. Klingbeil. A non-local extension of gurson-based ductile damage modeling. *Computational Materials Science*, 26:219–229, 2003.

[112] J. Rice and D. Tracey. On the ductile enlargement of voids in triaxial stress fields. *Journal of the Mechanics and Physics of Solids*, 17(3):201–217, 1969.

[113] J. R. Rice. A path independent integral and the approximate analysis of strain concentration by notches and cracks. *Journal of applied mechanics*, 35(2):379–386, 1968.

[114] J. R. Rice and D. M. Tracey. On the ductile enlargement of voids in triaxial stress fields. *Journal of the Mechanics and Physics of Solids*, 17(3):201–217, 1969.

[115] R. O. Ritchie, J. F. Knott, and J. R. Rice. On the relationship between critical tensile stress and fracture toughness in mild steel. *Journal of the Mechanics and Physics of Solids*, 21(6):395–410, 1973.

[116] A. Rossoll, C. Berdin, and C. Prioul. Determination of the fracture toughness of a low alloy steel by the instrumented charpy impact test. *International Journal of Fracture*, 115(3):205–226, 2002.

[117] S. Roth and M. Kuna. Numerical study on interfacial damage of sprayed coatings due to thermo-mechanical fatigue. In *Proceedings of the XI international conference on computational plasticity*, 2011.

[118] G. Rousselier. Ductile fracture models and their potential in local approach of fracture. *Nuclear engineering and design*, 105(1):97–111, 1987.

[119] G. Rousselier, J.-C. Devaux, G. Mottet, and G. Devesa. A methodology for ductile fracture analysis based on damage mechanics: an illustration of a local approach of fracture. In *Nonlinear Fracture Mechanics: Volume II Elastic-Plastic Fracture*. ASTM International, 1988.

[120] RP2Z. Recommended practice for preproduction qualification for steel plates for offshore structures. *API, American Petroleum Institute, Washington, DC, USA*, 2005.

[121] C. Ruggieri and R. Dodds. Wstress release 1.0: numerical computation of probabilistic fracture parameters for 3-d cracked solids. Technical report, BT-PNV-30 (Technical Report), EPUSP, University of Sao Paulo, 1997.

[122] C. Ruggieri and R. H. Dodds. A transferability model for brittle fracture including constraint and ductile tearing effects: a probabilistic approach. *International Journal of Fracture*, 79(4):309–340, 1996.

[123] C. Ruggieri and R. Dodds Jr. Probabilistic modeling of brittle fracture including 3-d effects on constraint loss and ductile tearing. *Le Journal de Physique IV*, 6(C6):C6–353, 1996.

[124] C. Ruggieri and R. H. Dodds Jr. Numerical evaluation of probabilistic fracture parameters using wstress. *Engineering Computations*, 15(1):49–73, 1998.

[125] M. Samal, M. Seidenfuss, E. Roos, B. Dutta, and H. Kushwaha. Experimental and numerical investigation of ductile-to-brittle transition in a pressure vessel steel. *Materials Science and Engineering: A*, 496(1-2):25–35, 2008.

[126] H. Scheide. Modelling the ductile-to-brittle transition regions in arctic steels (project thesis). December 2017.

[127] J. Schuenemeyer and D. Gautier. Aggregation methodology for the circum-arctic resource appraisal. *Mathematical Geosciences*, 42(5):583–594, July 2010.

[128] V. Shlyannikov, N. Boychenko, and A. Tartygasheva. In-plane and out-of-plane crack-tip constraint effects under biaxial nonlinear deformation. *Engineering Fracture Mechanics*, 78(8):1771–1783, 2011.

[129] SINTEF. Arctic materials, www.sintef.no/en/projects/arctic-materials. March 2018.

[130] I. N. Sneddon. The distribution of stress in the neighbourhood of a crack in an elastic solid. 187(1009):229–260, October 1946.

[131] R. Song, D. Ponge, and D. Raabe. Improvement of the work hardening rate of ultrafine grained steels through second phase particles. *Scripta materialia*, 52(11):1075–1080, 2005.

[132] H. Tada. *The stress analysis of cracks handbook*. ASME Press Professional Engineering Publishing, New York, N.Y, 3rd edition, 2000.

[133] P. F. Thomason. A theory for ductile fracture by internal necking of cavities. *J.Inst.Met.*, 96:360–365, 1968.

[134] P. F. Thomason. *Ductile fracture of metals*. Pergamon Press, Oxford, 1990.

[135] G. E. Totten and M. A. Howes. *Steel heat treatment handbook*. Marcel Dekker, New York, 1997.

[136] V. Tvergaard. Influence of voids on shear band instabilities under plane strain conditions. *International Journal of Fracture*, 17(4):389–407, August 1981.

[137] V. Tvergaard. On localization in ductile materials containing spherical voids. *International Journal of Fracture*, 18(4):237–252, April 1982.

[138] V. Tvergaard and J. W. Hutchinson. The relation between crack growth resistance and fracture process parameters in elastic-plastic solids. *Journal of the Mechanics and Physics of Solids*, 40(6):1377–1397, 1992.

[139] V. Tvergaard and J. W. Hutchinson. Two mechanisms of ductile fracture: void by void growth versus multiple void interaction. *International Journal of Solids and Structures*, 39(13):3581–3597, 2002.

[140] V. Tvergaard and A. Needleman. Analysis of the cup-cone fracture in a round tensile bar. *Acta Metallurgica*, 32(1):157–169, 1984.

[141] K. Wallin. *Optimized estimation of the Weibull distribution parameters*. Valtion teknillinen tutkimuskeskus. Metallilaboratorio, 1989.

[142] K. Wallin. Statistical aspects of constraint with emphasis on testing and analysis of laboratory specimens in the transition region. In *Constraint Effects in Fracture*. ASTM International, 1993.

[143] K. Wallin. Quantifying tstress controlled constraint by the master curve transition temperature t0. *Engineering Fracture Mechanics*, 68(3):303–328, 2001.

[144] K. Wallin. Master curve analysis of the euro fracture toughness dataset. *Engineering Fracture Mechanics*, 69(4):451–481, 2002.

[145] Y. Wang, M. Chen, F. Zhou, and E. Ma. High tensile ductility in a nanostructured metal. *Nature*, 419(6910):912, 2002.

[146] A. Weck, D. Wilkinson, E. Maire, and H. Toda. Visualization by x-ray tomography of void growth and coalescence leading to fracture in model materials. *Acta Materialia*, 56(12):2919–2928, 2008.

[147] W. Weibull et al. A statistical distribution function of wide applicability. *Journal of applied mechanics*, 18(3):293–297, 1951.

[148] A. Wells. Unstable crack propagation in metals: cleavage and fast fracture. In *Proceedings of the crack propagation symposium*, volume 1, 1961.

[149] A. Wells. Application of fracture mechanics at and beyond general yielding. *British Welding Journal*, 10(11):563–70, 1963.

[150] A. Wormsen, A. Fjeldstad, and G. Härkegård. A post-processor for fatigue crack growth analysis based on a finite element stress field. *Computer Methods in Applied Mechanics and Engineering*, 197(6-8):834–845, 2008.

[151] L. Xia and L. Cheng. Transition from ductile tearing to cleavage fracture: a cell-model approach. *International Journal of Fracture*, 87(3):289, 1997.

[152] L. Xia and C. F. Shih. Ductile crack growth–iii. transition to cleavage fracture incorporating statistics. *Journal of the Mechanics and Physics of Solids*, 44(4):603–639, 1996.

[153] J. Xu, Z. Zhang, E. Østby, B. Nyhus, and D. Sun. Effects of crack depth and specimen size on ductile crack growth of sent and senb specimens for fracture mechanics evaluation of pipeline steels. *International Journal of Pressure Vessels and Piping*, 86(12):787–797, 2009.

[154] J. Xu, Z. Zhang, E. Østby, B. Nyhus, and D. Sun. Constraint effect on the ductile crack growth resistance of circumferentially cracked pipes. *Engineering Fracture Mechanics*, 77(4):671–684, 2010.

[155] X. P. Xu. Void nucleation by inclusion debonding in a crystal matrix. *Modelling and Simulation in Materials Science and Engineering*, 1(2):111–132, January 1993.

[156] L. Xue. Damage accumulation and fracture initiation in uncracked ductile solids subject to triaxial loading. *International Journal of Solids and Structures*, 44(16):5163–5181, 2007.

[157] L. Xue and T. Wierzbicki. Ductile fracture initiation and propagation modeling using damage plasticity theory. *Engineering Fracture Mechanics*, 75(11):3276–3293, 2008.

[158] A. T. Zehnder. *Fracture Mechanics*. Lecture Notes in Applied and Computational Mechanics, 62. 2012.

[159] X. Zhang and J. Knott. Cleavage fracture in bainitic and martensitic microstructures. *Acta materialia*, 47(12):3483–3495, 1999.

[160] Z. Zhang, C. Thaulow, and J. Ødegård. A complete gurson model approach for ductile fracture. *Engineering Fracture Mechanics*, 67(2):155–168, 2000.

[161] M.-C. Zhao, T. Hanamura, H. Qiu, K. Nagai, and K. Yang. Grain growth and hall–petch relation in dual-sized ferrite/cementite steel with nano-sized cementite particles in a heterogeneous and dense distribution. *Scripta materialia*, 54(6):1193–1197, 2006.

[162] M.-C. Zhao, T. Hanamura, F. Yin, H. Qiu, and K. Nagai. Formation of bimodal-sized structure and its tensile properties in a warm-rolled and annealed ultrafine-grained ferrite/cementite steel. *Metallurgical and Materials Transactions A*, 39(7):1691–1701, 2008.

[163] M.-C. Zhao, F. Yin, T. Hanamura, K. Nagai, and A. Atrens. Relationship between yield strength and grain size for a bimodal structural ultrafine-grained ferrite/cementite steel. *Scripta materialia*, 57(9):857–860, 2007.

[164] M.-C. Zhao, T.-Y. Zeng, J.-L. Li, H. Xiaofang, Y.-C. Zhao, and A. Atrens. Identification of the effective grain size responsible for the ductile to brittle transition temperature for steel with an ultrafine grain size ferrite/cementite microstructure with a bimodal ferrite grain size distribution. *Materials Science and Engineering: A*, 528(12):4217–4221, 2011.

[165] F. W. Zok. On weakest link theory and weibull statistics. *Journal of the American Ceramic Society*, 100(4):1265–1268, April 2017.

Appendix A

Equations

A.1 Effective and Mean Stress

The following stress parameters are utilised in Equation 2.11

Effective stress (von Mises)

$$\sigma_e = \frac{1}{\sqrt{2}}\sqrt{(\sigma_1 - \sigma_2)^2 + (\sigma_1 - \sigma_3)^2 + (\sigma_3 - \sigma_2)^2} \tag{A.1}$$

Mean (hydrostatic) stress

$$\sigma_m = \frac{\sigma_1 + \sigma_2 + \sigma_3}{3} \tag{A.2}$$

A.2 Void Radius and Intervoid Distance

Equation A.3 and A.4 deduce the void radius and the intervoid distance, respectively. ϵ_{xx} and ϵzz are components of the strain tensor, R_0 is the initial intervoid radius and f is the void volume fraction. These parameters are used in Equation 3.16 and is referred to in Section 3.2.1.

$$r = \sqrt{\frac{f}{\pi} e^{\epsilon_{xx} + \epsilon zz}} \tag{A.3}$$

$$R = R_0 e^{\epsilon_{xx}} \tag{A.4}$$

Appendix B

Weibull Analysis

B.1 Constitutive Matlab Functions

This appendix section presents the most relevant Matlab functions used to calibrate and analyse the Weibull distributed fracture mechanics data. All the constitutive Matlab functions are from the MathWorks library and the Statistics and Machine Learning Toolbox. [85] The Matlab functions are utilised to estimate the constitutive Weibull parameters and the corresponding cumulative distribution functions as described in Section 5.3.

Maximum Likelihood Estimation (MLE) of Weibull Parameters

$phat$ is a two-element vector where $phat(1)$ is the Weibull scale parameter estimate, σ_u and $phat(2)$ is the Weibull shape parameter estimate, m (Weibull modulus). pci is a 2x2 matrix and returns the confidence intervals of the Weibull parameter estimates. Equation 1 and 2 yields the same maximum likelihood Weibull parameter estimates with 95% Weibull parameter confidence intervals. Equation 3 can be utilised to return defined 100(1-alpha)% Weibull parameter confidence intervals. The $data$ input values can either be experimental fracture toughness values or simulated Weibull stresses at fracture.

```
1: [phat,pci] = mle(data,'distribution','Weibull');

2: [phat,pci] = wblfit(data);

3: [phat,pci] = wblfit(data,alpha);
```

Calculate the Cumulative Distribution Function points with MLE

In order to calculate the data points for the Weibull cumulative distribution function, the Weibull parameters must first be estimated with the integrated maximum likelihood Weibull parameter estimation function $wblfit(data)$ returning the 1x2 parameter vector $phat$. After the Weibull modulus and the scale parameter are estimated, the resulting cumulative distribution function data points, $cdfpoints$ can be calculated with the integrated $wblcdf$ function.

```
cdfpoints = wblcdf(data,phat(1), phat(2))
```

Estimate Weibull Cumulative Distribution Functions

This Matlab script is used to estimate Weibull cumulative distribution functions. $data$ is either critical Weibull stresses or fracture toughness values from the respective fracture mechanics test series. The fracture dataset is arranged in ascending order.

```
phat = wblfit(data);
%Calculates Weibull parameters
%Scale parameter = phat(1), shape parameter = phat(2)

min_data_value = data(1) - 200;
%Smallest critical Weibull stress - arbitrary confidence value

max_data_value = data(length(data)) + 200;
%Largest critical Weibull stress + arbitrary confidence value

x = [min_data_value:10:max_data_value]; %Generates data points
y = x.'; %Converts vector to column

cdf = wblcdf(y, phat(1), phat(2))
%Estimates the Weibull cumulative distribution function
```

B.2 LINKpfat

This section briefly introduces LINKpfat and its constitutive modules used to calculate Weibull stresses, and it is exclusively referred to in Section 5.3 as one of the segments in the comprehensive Beremin model implementation scheme.

LINKpfat is an in-house finite element post-processor tool which uses information from finite element analyses to calculate deterministic and probabilistic material features. The model geometries and stresses are extracted directly from the finite element analysis result file (.odb in ABAQUS), and LINKpfat is compatible with programs such as ABAQUS, ANSYS, and NX. Nodal coordinates, element topology and principal stresses are some of the extracted features used in the computations. The two deterministic modules in LINKpfat are defined as the Local Stress Approach (LSA) and the Single Defect Approach (SDA) which in turn can be used to predict the component fatigue lifetime by considering simulated stresses and crack-like defects. The Random Defect Approach (RDA) is one of the probabilistic modules and is based on finite element stresses and Poisson distributed material defects and can be used to calculate the fatigue life distribution by determining the required cycles needed for each defect to become critical.

The second probabilistic module is the Weakest-link Approach (WEAK). This module is based on the weakest-link principles in Section 2.8.1 and assumes the component reliability to be equivalent to the product of the reliability of each element in the finite element analysis. Thus, the entire component fails if one of the finite elements fails, and the probability of failure of all the small element volumes is obtained from the two-parameter Weibull cumulative distribution function

$$P_F = 1 - exp\Bigg[- \Big(\frac{\sigma_a}{\sigma^*_{A0}(R,n)} \Big)^{b_\sigma} \Bigg] \tag{B.1}$$

b_σ is the Weibull modulus (shape parameter), σ^*_{A0} is the scale parameter, and σ_a is the Weibull stress. σ^*_{A0} is equivalent to the Weibull stress at 63.2% probability of failure and represents the resistance to brittle failure. However, the scale parameter is dependent on the number of cycles, n and the stress ratio, $R = \sigma_{min}/\sigma_{max}$ which in turn makes the parameter biased in fracture mechanics analyses. b_σ determines the amount of scattering in the Weibull distribution where low b_σ-values are equivalent with large scatter bands, and high b_σ-values are equivalent with narrow scatter bands. The Weibull stress, σ_a is defined as the stress amplitude

$$\sigma_a = \Bigg[\frac{1}{V_0} \int_V \sigma_1^{b_\sigma} dV \Bigg]^{1/b_\sigma} \tag{B.2}$$

where V_0 is the reference volume, and σ_1 is the maximum principal stress extracted from the element nodes. Thus, the resulting Weibull stress in Equation B.2 is calculated by performing a summation of all the principal stresses in all the element nodes in the finite element model and is the only parameter which is extracted from LINKpfat.

Appendix C

Gurson Analysis

C.1 Run Input File

This commando script calls for the input file sequentially and creates a new job with corresponding output file, and is used in the Gurson implementation scheme in Section 5.4. The commando script also defines how many CPU cores to initiate when running the commando which in this case is four CPU cores.

```
@echo off
REM CPUS can be between 1 and 4. Default is 1
call abaqus cpus=4 job=Gurson_T_RT input=Gurson_T_RT.inp -seq
pause
```

C.2 Run UMAT

This code is compiled with the commando in Appendix C.1 in order to run the Gurson user-defined material (UMAT) automatically in the simulation as described in Section 5.4. The code must be in the same folder as the commando script and the input file. It locates the Gurson UMAT .dll file and prints a message to indicate the UMAT initiation. The UMAT code is a detailed and long document and is not presented due to redundant space requirements. Abaqus_v6.env prints the identification message while StandardU.dll and usub_lib_dir represent the complete Gurson user subroutine code.

```
#
# set usub_lib_dir to the directory where StandardU.dll
is located.
#
usub_lib_dir=r'C:\ABAQUS614'

print 'Hello from abaqus_v6.env: usub_lib_dir=%s'
% ( usub_lib_dir )
```

C.3 State-Dependent Variables

The following list describes the state-dependent output variables from the user subroutine called upon in Appendix C.2. SDV = State-Dependent Variable

- SDV1 - The equivalent plastic strain of the matrix material
- SDV2 - The void volume fraction at the end of the increment
- SDV3 - Stress triaxiality
- SDV4 - Controlling parameter for failure.

```
IF F >  FMAX, STATVE(4) = -FC < 0.0,
        TOTAL FAILURE
IF F >= FC,   STATEV(4) = FC,
        BEFORE COALESCENCE.
IF F <  FC,   STATEV(4) = 0.0,
        NOT FAILED AT ALL.
```

- SDV5 - The plastic strain rate at loading initiation
- SDV6 - Temporary print controlling variable

C.4 Data Extraction: Output File

This commando calls upon the python script GetData.py and must define the local storage location of the python script, the output file it is going to extract the data from, the yield strength, the strain hardening exponent, and the node numbers for the CTOD, the crack tip, and the adjacent crack tip node. The GetData.py script extracts the CTOD, J-integral and crack growth from the output file (.dat), but is not presented in full due to excessive space requirements. The data extraction is exclusively used in the Gurson implementation scheme in Section 5.4.

```
@echo off
(
abaqus python C:\ABAQUS614\Henrik_ABAQUS\Scripts\GetData.py
-f Gurson_T_RT.dat  -y 667 -n 0.1  --node-ctod 7
--node-tip 3000 --node-crack0 21
pause
)
```

Appendix D

Fracture Mechanics

D.1 Preliminary Experimental Force-CMOD Curves

The following figures illustrate the experimental Force-CMOD curves from the recent SENB05 fracture mechanics test series as referred to in Section 4.1.

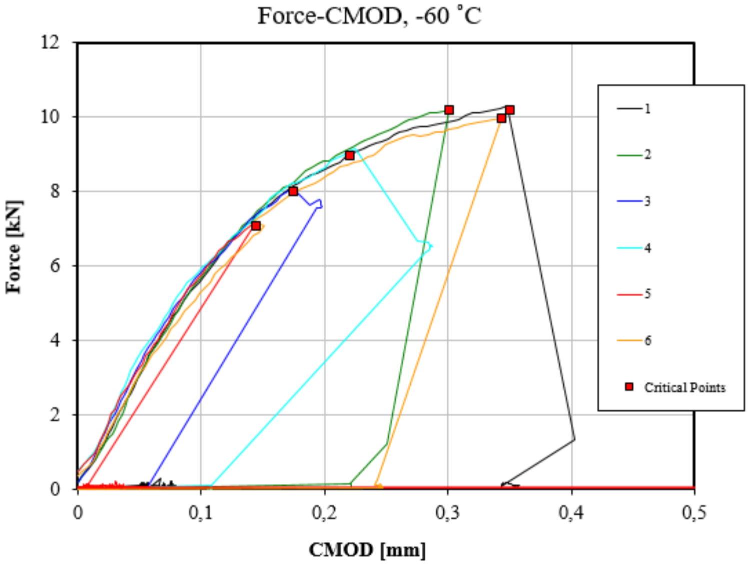

Figure D.1: Experimental Force-CMOD curves for specimen 1 to 6 at -60°C.

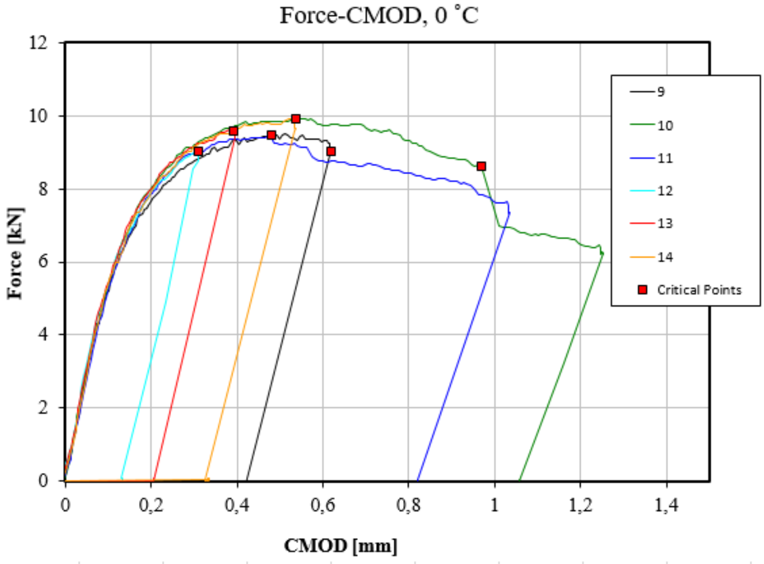

Figure D.2: Experimental Force-CMOD curves for specimen 9 to 14 at 0°C.

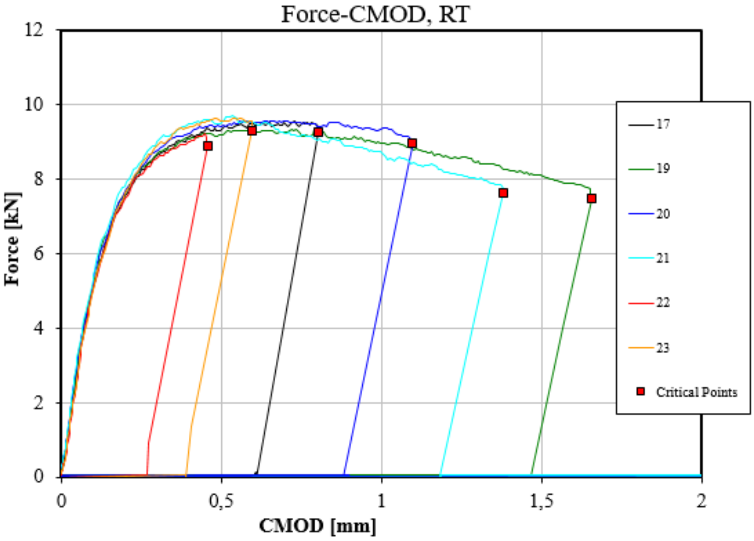

Figure D.3: Experimental Force-CMOD curves for specimen 17 to 23 at 21°C.

D.2 DBT: Fractured and Unloaded Specimens

This section illustrates the experimental fracture toughness values from the fracture mechanics test series used to find the constitutive results in Chapter 6 and is exclusively referred to in Section 6.1.

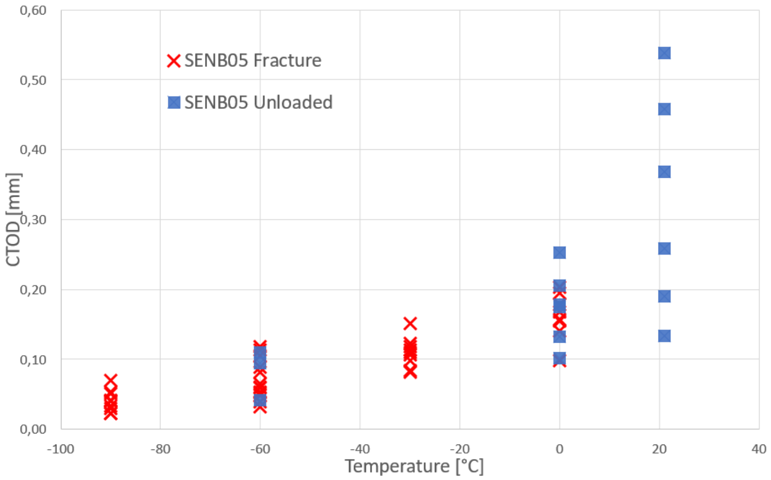

Figure D.4: The ductile-to-brittle transition of **valid** SENB05 unloaded and fractured specimens. Some fracture specimens are unloaded at desired CMODs, and some have invalid CTOD values.

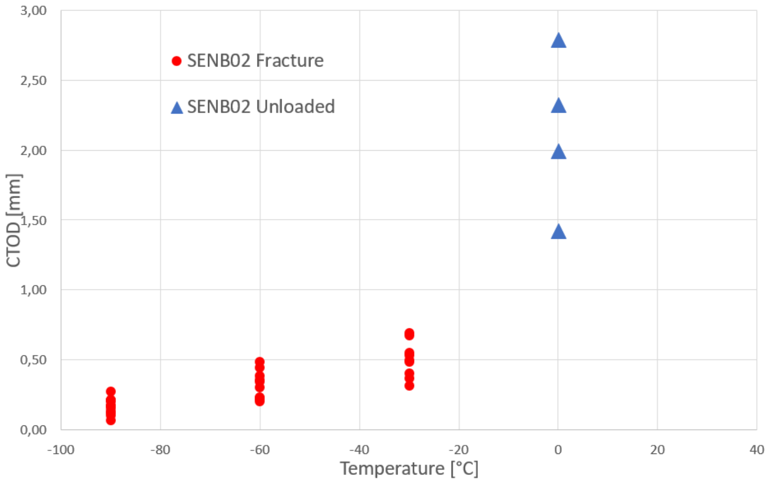

Figure D.5: The ductile-to-brittle transition of **valid** SENB02 unloaded and fractured specimens. Some specimens fractured at $0^{\circ}C$ but have invalid CTOD values

D.3 Simulated and Experimental Force-CMOD Curves

This section is referred to in Section 6.1.1 and comprises all the simulated and experimental Force-CMOD curves for SENB05 and SENB02. A few Force-CMOD curves are additionally presented in **Figure 6.5**. As discussed in Section 6.1, some of the CMOD values might be incorrect as the red squares indicate initially measured fracture and unloading points. See Appendix D.4 for all the valid fracture mechanics data.

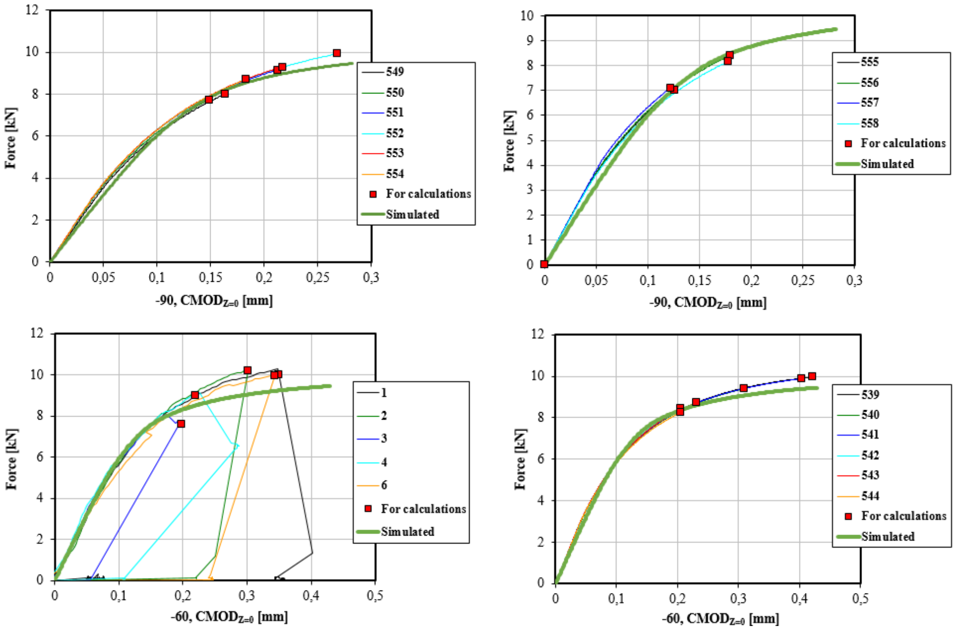

Figure D.6: SENB05: Force-CMOD curves at -90°C and -60°C

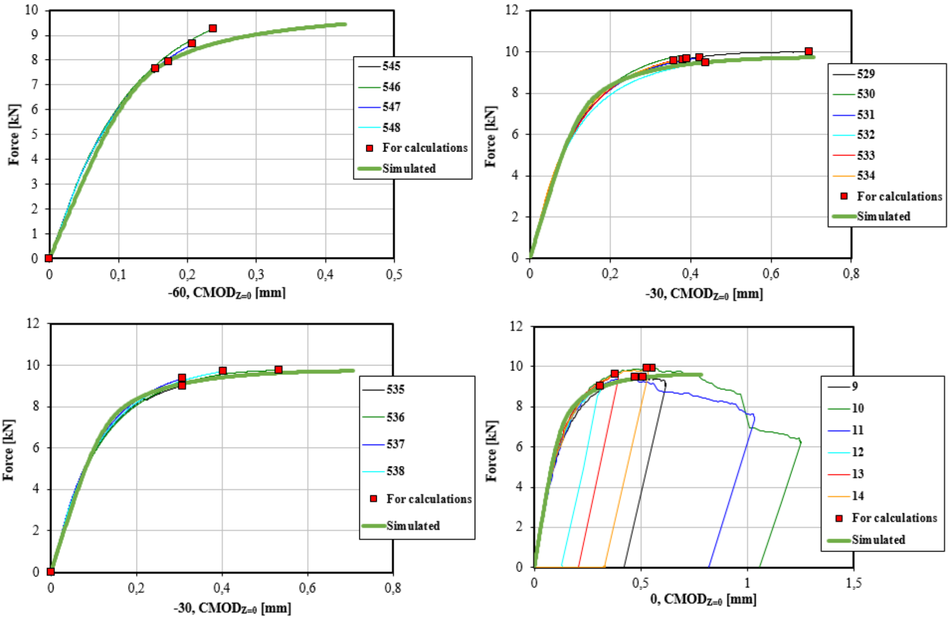

Figure D.7: SENB05: Force-CMOD curves at -60°C, -30°C and 0°C

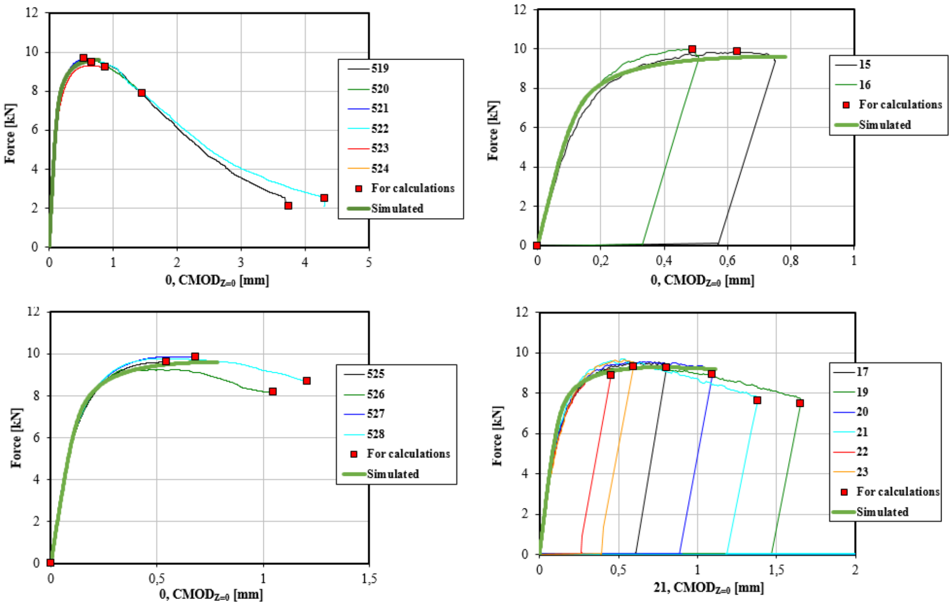

Figure D.8: SENB05: Force-CMOD curves at 0°C and 21°C

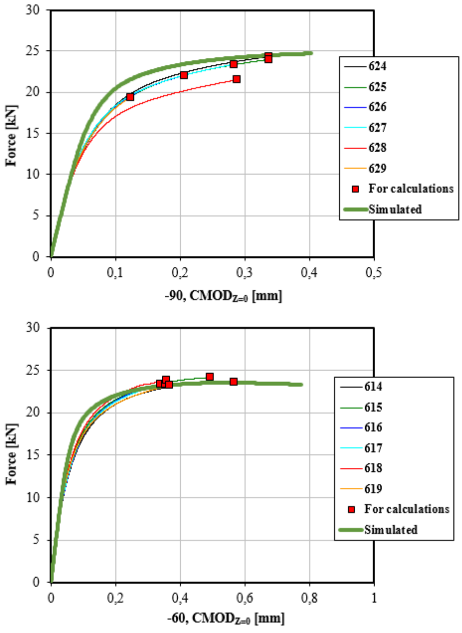

Figure D.9: SENB02: Force-CMOD curves at -90°C and -60°C

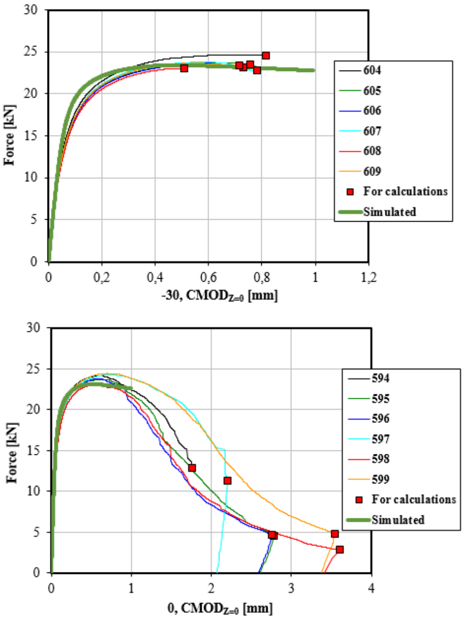

Figure D.10: SENB02: Force-CMOD curves at -30°C and 0°C

D.4 Fracture Mechanics Data

This section describes all the fracture mechanics test data from a recent SENB05 test series and an Arctic Materials I project series. The recent SENB05 test series includes the specimens from #1 to #23, and the Arctic Materials I test series comprises the specimens from #520 to #673. The section is referred to in Section 6.1, and the following fracture mechanics data are illustrated in **Figure 6.2 and 6.4**. The MOTE values are based on fracture point characterisation according to BS 7910 [30] and **Table D.1**.

Table D.1: MOTE according to BS 7910

Ranked value of data set	Data set size BS 7910
Minimum Value	3-5
2^{nd} lowest value	6-10
3^{rd} lowest value	11-15
4^{th} lowest value	N-A

Table D.2: SENB05 fracture mechanics data. F = Fracture, U = Unloaded
NV = Not valid, max force in *italic* and MOTE in **bold**

Specimen #	Temperature $^{\circ}C$	CTOD [mm]	Δa [mm]	Force [kN]	Mode F/U	Exceeded Max Force Yes/No
549	-90	0.033	0.00	8.00	F	No
550	-90	0.030	0.00	7.74	F	No
551	-90	0.051	0.02	9.15	F	No
552	-90	0.070	0.03	*9.91*	F	No
553	-90	0.053	0.02	9.30	F	No
554	-90	0.042	0.02	8.69	F	No
555	-90	**0.023**	0.00	7.03	F	No
556	-90	0.040	0.02	8.41	F	No
557	-90	0.022	0.00	7.11	F	No
558	-90	0.040	0.00	8.16	F	No
1	-60	0.105	0.07	10.00	F	No
2	-60	0.094	0.08	*10.22*	U	No
3	-60	0.059	0.05	7.59	F	No
4	-60	0.089	0.07	8.99	F	No
5	-60	0.042	0.03	7.12	U	No
6	-60	0.110	0.06	9.97	U	No
539	-60	0.119	0.06	9.96	F	No
540	-60	0.082	0.07	9.40	F	No
541	-60	0.113	0.06	9.89	F	No
542	-60	**0.049**	0.05	8.44	F	No
543	-60	0.061	0.06	8.73	F	No
544	-60	0.052	0.05	8.26	F	No
545	-60	0.039	0.00	7.96	F	No
546	-60	0.065	0.06	9.26	F	No
547	-60	0.053	0.03	8.64	F	No
548	-60	0.032	0.02	7.64	F	No

Table D.3: SENB05 fracture mechanics data. F = Fracture, U = Unloaded
NV = Not valid, max force in *italic* and MOTE in **bold**

Specimen #	Temperature $^{\circ}C$	CTOD [mm]	Δa [mm]	Force [kN]	Mode F/U	Exceeded Max Force Yes/No
529	-30	NV	NV	*9.99*	U	No
530	-30	0.106	0.09	9.62	F	No
531	-30	0.118	0.13	9.70	F	No
532	-30	0.123	0.12	9.46	F	No
533	-30	0.098	0.08	9.59	F	No
534	-30	0.110	0.06	9.65	F	No
535	-30	0.082	0.07	9.01	F	No
536	-30	0.152	0.10	9.77	F	No
537	-30	**0.083**	0.07	9.36	F	No
538	-30	0.113	0.09	9.69	F	No
9	0	0.205	0.23	9.33	U	Yes
10	0	0.168	NV	8.62	F	No
11	0	**0.141**	NV	9.48	F	No
12	0	0.101	0.08	9.02	U	No
13	0	0.133	0.11	9.42	U	No
14	0	0.175	0.17	9.66	U	No
15	0	0.253	0.38	9.52	U	Yes
16	0	0.178	0.31	9.69	U	No
519	0	NV	NV	NV	U	Yes
520	0	NV	NV	7.87	U	Yes
521	0	0.155	NV	9.68	F	No
522	0	NV	NV	9.11	F	Yes
523	0	NV	NV	9.24	F	No
524	0	0.195	NV	9.50	F	Yes
525	0	0.157	0.13	9.60	F	No
526	0	0.098	NV	9.27	F	No
527	0	0.203	0.15	*9.85*	F	No
528	0	0.178	NV	9.77	F	No
17	21	0.259	0.22	9.27	U	Yes
19	21	0.538	0.89	7.48	U	Yes
20	21	0.368	0.51	8.95	U	Yes
21	21	0.458	0.77	7.62	U	Yes
22	21	0.134	0.09	8.89	U	Yes
23	21	0.190	0.19	*9.31*	U	Yes

Table D.4: SENB02 fracture mechanics data. F = Fracture, U = Unloaded
NV = Not valid, max force in *italic* and MOTE in **bold**

Specimen #	Temperature $^{\circ}C$	CTOD [mm]	Δa [mm]	Force [kN]	Mode F/U	Exceeded Max Force Yes/No
624	-90	0.208	0.14	*24.30*	F	No
625	-90	0.205	0.14	23.96	F	No
626	-90	**0.120**	0.09	22.04	F	No
627	-90	0.174	0.09	23.39	F	No
628	-90	0.172	0.10	21.49	F	No
629	-90	0.066	0.07	19.38	F	No
630	-90	0.154	0.10	23.49	F	No
631	-90	0.205	0.14	24.00	F	No
632	-90	0.103	0.08	21.17	F	No
633	-90	0.272	NV	25.85	F	No
634	-90	0.213	0.14	23.38	F	No
635	-90	0.130	0.09	22.73	F	No
614	-60	0.343	0.43	23.66	F	No
615	-60	0.304	0.36	*24.20*	F	No
616	-60	0.202	0.18	23.36	F	No
617	-60	**0.212**	0.18	23.37	F	No
618	-60	0.227	0.23	23.85	F	No
619	-60	0.232	0.15	23.22	F	No
620	-60	0.353	0.31	23.76	F	No
621	-60	0.384	0.39	24.23	F	No
622	-60	0.445	0.45	24.24	F	No
623	-60	0.483	0.40	24.69	F	No
604	-30	0.530	0.46	*24.53*	F	Yes
605	-30	0.484	0.64	23.47	F	Yes
606	-30	0.400	NV	23.65	F	No
607	-30	0.496	NV	22.72	F	Yes
608	-30	0.313	0.35	23.01	F	No
609	-30	NV	NV	23.66	F	No
610	-30	**0.366**	NV	22.93	F	No
611	-30	0.674	NV	22.94	F	Yes
612	-30	0.693	NV	22.99	F	Yes
613	-30	0.551	NV	23.57	F	Yes
594	0	NV	NV	15.20	F	Yes
595	0	NV	NV	*17.14*	F	Yes
596	0	NV	NV	16.53	F	Yes
597	0	1.420	NV	15.10	U	Yes
598	0	NV	NV	15.70	F	Yes
599	0	2.320	NV	4.77	U	Yes
600	0	2.786	NV	8.08	U	Yes
601	0	NV	NV	15.55	F	Yes
602	0	1.994	NV	4.38	U	Yes
603	0	NV	NV	15.11	F	Yes